Studies of the Electromagnetic Calorimeter and Direct Photon Production at the CMS Detector.

Elspeth Catriona Reid

A thesis submitted to the University of Bristol for the degree of Doctor of Philosophy

1999

Table of Contents

List of Figures

1 List of Tables

1 Introduction

This thesis describes the work I have undertaken as a member of the CMS collaboration. I have been working on the test beam programme for the Electromagnetic calorimeter and also studying direct photon production. The CMS collaboration is composed of 145 institutions from 30 countries, with a total membership of more than 1700 scientists who are all working towards the construction of a general purpose detector for the Large Hadron Collider (LHC).

The LHC 7 TeV proton-proton collider is to be built at CERN, the European Centre for Particle Physics where it will replace the existing LEP collider. The project is currently (Spring 1999) in the final design and testing stages and it is expected that construction will be complete and data taking will begin in the year 2005

1.1 The Standard Model

Particle	**Symbol**	**Charge**	**Mass (MeV/c^2)**
electron	e	-1	0.511
electron neutrino	ν_e	0	$< 5.10^{-6}$
muon	μ	-1	105.7
muon neutrino	ν_μ	0	< 0.17
tau	τ	-1	1777
tau neutrino	ν_τ	0	< 18.2

Table 1.1: The three generations of leptons.

In order to set the framework to which the study of photons at CMS will contribute it is necessary to briefly consider the known elementary particles and the forces which govern their interactions. The mathematical description of this set of particles, their antiparticle counterparts and the physical laws they obey is known as the Standard Model.

In the Standard Model all matter is composed of point-like particles which have values of spin equal to one half. These *fermions*, can be further divided into *leptons* (Table 1.1) and *quarks* (Table 1.2). Both leptons and quarks can be grouped into three 'generations', the corresponding members of each generation having identical properties except for mass. The reason for these generations is still unknown - most matter in the universe is composed of particles from the first generation: 'up' and 'down' quarks combine to form the protons (*uud)* and neutrons (*udd*) that make up the nuclei of atoms: and electrons orbit the nuclei, giving atoms their chemical and material properties. The heavier versions of the quarks and leptons can be found in cosmic rays and can be created in particle accelerators. There is also the possibility that the 'dark matter' which is thought to make up some of the universe may be composed of some exotic, unknown particles.

Particle	**Symbol**	**Charge**	**Mass (MeV/c^2)**
up	*u*	+2/3	1.5-5
down	*d*	-1/3	3-9
charm	*c*	+2/3	1100-1400
strange	*s*	-1/3	505
top	*t*	+2/3	173800
bottom	*b*	-1/3	4100-4400

Table 1.2: The three generations of quarks.

Governing how these particles interact are the four known forces: Electromagnetic, Weak, Strong and Gravitational. Each of these forces is mediated by particles with integer values of spin, known as *bosons* (Table 1.3). For example particles with electric charge interact through the electromagnetic force mediated by the photon. Weak interactions proceed through the exchange of a W or Z boson. The electromagnetic and the weak force are treated theoretically as two aspects of one Electroweak force.

The Gravitational force has been known about for longer than the other three forces and the general theory of relativity correctly describes large scale gravitational effects. However, there is as yet no well developed quantum theory of gravitation. Gravitational radiation is expected to exist although it has not yet been observed directly. The quantum of the radiation has been called the graviton before observation. The nature of the gravitational field implies that it will be a spin-2 particle.

Boson	**Symbol**	**Force**	**Electric Charge**	**Mass (MeV/c^2)**
photon	γ	Electromagnetic	0	0
W	W	Weak	±1	80410
Z	Z	Weak	0	91187
gluon	g	Strong	0	0
graviton	?	Gravitational	0	0

Table 1.3: Bosons and the forces they mediate.

Quarks are never found in isolation but are confined within composite particles such as the proton. These composite particles also contain many gluons, which interact with the quarks and with each other. The gluons are the mediators of the Strong force, which is responsible for binding the proton together and also binding protons and neutrons together in the atomic nucleus.

The Strong force introduces a new type of quantum number called colour. Colour is analogous to the electromagnetic charge but has three facets. Quarks can be red, green, or blue and antiquarks are antired, antigreen, or antiblue. The gluons can be thought of as carrying these characteristics by being a mixture of colour and anticolour, which enables them to exchange colour between two quarks. This is noticeably different to electromagnetism where the photons do not themselves carry charge. Only colourless particles are allowed to exist freely in nature. Therefore quarks only exist in quark-antiquark states called *mesons*, in which the colour charges cancel, or in three quark states called *baryons*, in which red, green and blue form a colourless combination. More generally the term *hadron* is used to refer to any particle that is composed of quarks, whether baryon or meson.

The Standard Model is a stable and consistent structure which explains most of the fundamental behaviour of particles and forces extremely well. However there are still some important questions to be addressed. Are quarks and leptons really fundamental? Why does there seem to be more matter than antimatter in the Universe? Why are there three generations of matter particles? Why are there huge mass differences between the three generations? Even more importantly, what is the origin of mass?

The Standard Model incorporates the idea that massive fundamental particles acquire their mass via an interaction with a field which is postulated to fill all of space. This is known as the Higgs field. The principal reason for building the LHC is to find direct evidence for the existence of the Higgs field by producing and detecting its associated particle, the Higgs boson. There may be one Higgs boson or there may be more. Supersymmetric theories require charged as well as neutral Higgs bosons. It is also possible that the Higgs boson does not exist. If it does not exist then something else must be the origin of mass and hopefully the LHC would discover that.

The Higgs boson is expected to decay with a very short lifetime, and so will be detected by measuring its decay products. The modes of decay are dependent on the mass of the Higgs, which is poorly constrained by presently available data. The CMS experiment is designed to be able to detect the Higgs via different decay modes. An important one is $H \rightarrow \gamma\gamma$, since this is likely to be the easiest to detect if the Higgs is light which is favoured by current experiments. High quality photon detection capability is vital for CMS, contributing to the Higgs boson search and many of the other aims of the experiment.

1.2 Variables for Hadron Collider Physics

It is important to define a set of variables which are used in the study of high energy hadron-hadron interactions. The standard phase space variables of energy (E), momentum (p), polar angle (θ) and azimuthal angle (ϕ) can be used, however, the nature of hadron colliders makes the introduction of some additional quantities advisable.

A significant feature of hadron colliders is that while the hadrons can be given equal and opposite momenta, there is an inherent uncertainty in the momenta of the partons which interact. Unlike electron-positron (e^-e^+) colliders, where the two colliding particles and their momenta can be well defined, the quark and gluon substructure of the proton implies that we cannot predetermine which partons will interact and what momentum they will have. This means that in the lab, or detector, frame the momenta along the beam axis, which is defined to be in the *z* direction, will usually not sum to zero and the system will be Lorentz boosted.

In the transverse (x - y) plane however, we expect that the final state momenta will cancel, as the initial state transverse momenta are negligible. Therefore we define the transverse momentum and energy:

$$p_{\mathrm{T}} \equiv \sqrt{p_x^2 + p_y^2} \qquad (1.1)$$

$$E_{\mathrm{T}} = \sqrt{E^2 - p_z^2} \qquad (1.2)$$

which become important variables for collider physics. Note that if the particle mass $m << E$, or for massless particles such as the photon,

$$E_{\mathrm{T}} = p_{\mathrm{T}} = E \sin\theta \qquad (1.3)$$

The Lorentz boost also motivates an alternative to the polar angle θ because θ is not Lorentz invariant. For a relativistic particle with four-momentum (E, p_x, p_y, p_z) we define the rapidity, *y*:

$$y \equiv \frac{1}{2}\ln\left(\frac{E + p_z}{E - p_z}\right) \qquad (1.4)$$

which transforms under a Lorentz boost as $y \rightarrow y+$ [constant], thereby preserving the shape of the rapidity distribution under the boost. Again, if the mass of a particle is much

less than its energy we can simplify y to give the pseudorapidity, η:

$$\eta = -\ln \tan\left(\frac{\theta}{2}\right) \qquad (1.5)$$

Thus a pseudorapidity of $\eta = 0$ corresponds to $\theta = 90$ degrees from the beam (z) direction increasing to ∞ ($-\infty$) as the angle grows nearer to the $+z$ ($-z$) direction. Because the condition $m << E$ is a good approximation for high energy photons and jets, the pseudorapidity is used almost exclusively and is often referred to simply as the rapidity.

2 The LHC and the CMS Detector

2.1 The Large Hadron Collider

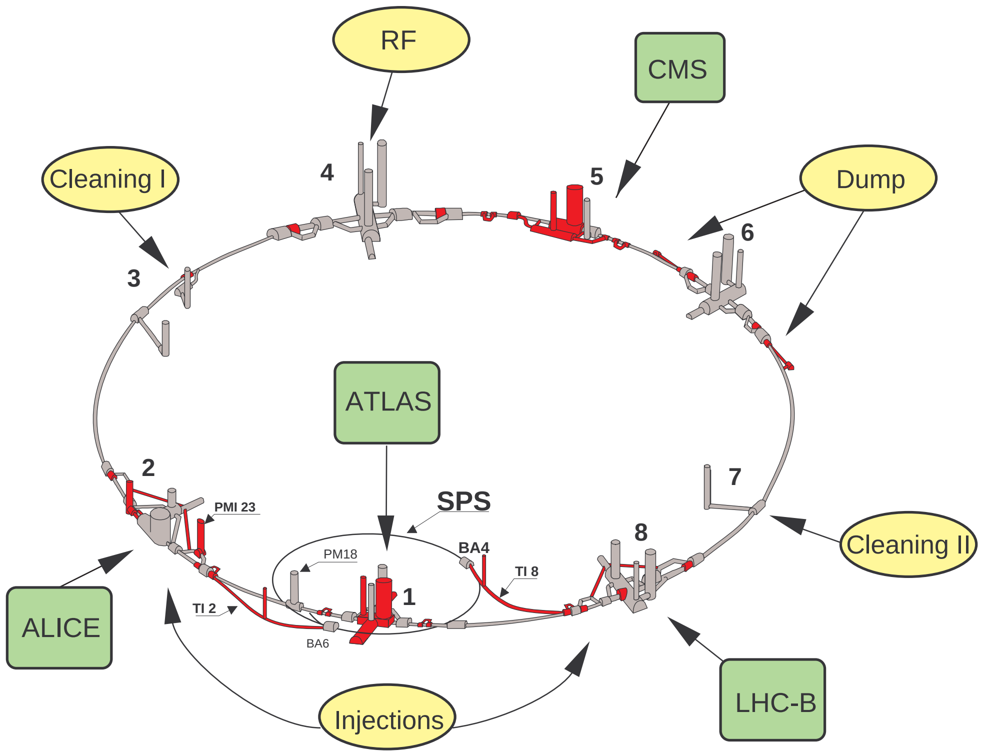

Figure 2.1: Schematic showing the LHC ring together with experimental caverns and machine utilities. Underground access to the ring is available at the points marked 1 to 8. The proposed experiment positions are also marked.

The LHC will be constructed in the 27km LEP tunnel when LEP finishes its final run in 2000. It is a ring of superconducting magnets which deflect and focus two beams of protons circulating in opposite directions. The LHC is composed of eight arcs that are separated by 528m long straight sections. In these sections will be the housings for the machine equipment and detectors, they will also include the four main points where the beams cross and the experiments are situated. Two of the experiments that will be built are general purpose detectors and two will be specialised detectors. A schematic of the LHC is shown in Figure 2.1.

The Atlas[1] and CMS[2] experiments are general purpose detectors and they will be built at points 1 and 5 respectively. At access points 2 and 8 will be Alice[3], a dedicated heavy ion experiment and LHC-B[4], a specialised B-physics detector.

2.1.1 The LHC Performance and Parameters

The main parameters of the LHC are listed in table 2.1 for standard proton-proton beams.

Centre of mass energy (TeV)	14
Magnetic field in bending magnets (T)	8.4
Design luminosity (cm^{-2} s^{-1})	10^{34}
Number of bunches per beam	2835
Bunch Spacing (m/ns)	7.5 / 25
Number of particles per bunch	10^{11}
Stored beam energy (MJ)	334

Table 2.1: Main LHC parameters for proton-proton running.

During standard running at the LHC two beams of protons will collide every 25ns at points 1 and 5. They will collide in bunches of ≈ 10^{11} particles with a combined centre of mass energy of 14 TeV. The LHC has a design luminosity of 10^{34} cm^{-2} s^{-1} but before this is reached there will be 2-3 years of low luminosity running at 10^{33} cm^{-2} s^{-1}.

Each superconducting magnet in the ring will require a magnetic field of 8.4 Tesla to provide sufficient control and bending for the 7 TeV proton beams. Each of the eight arcs of the LHC has 23 magnetic sections or ‘lattice periods’. Each lattice period consists of two symmetric halves of three 14.2m dipole bending magnets and a single quadrupole magnet.

A cycle of the LHC commences with bunches of protons injected singly into each of the four CERN PS booster rings. Within the PS the bunches are combined and accelerated up to a single bunch at an energy of 26 GeV. A 40MHz RF system then ‘captures’ each bunch and injects it into the CERN SPS. This is repeated three times which results in three bunches within the SPS separated by the LHC 25ns timing. A full SPS could hold eleven bunches. The proton beam is then injected from the SPS into the LHC with an initial energy of 450 Gev. The acceleration to 7 TeV then takes approximately 20 minutes [5]. The predicted time between LHC refills is about 7 hours. During this time the beam luminosity will fall to about 60% of its initial value.

2.1.2 Engineering Layout

The four straight sections of the LHC, not used for siting experiments, will be used for machine utilities. Points 3 and 7 will be used for beam cleaning. The cleaning systems are composed of collimators which will remove any particles that fall outside the defined aperture and dump them safely into appropriate shielding. The ‘halo’ of particles outside the aperture is fed by 10^9 protons per second. Only 10^6 of these protons would be needed to heat up the superconducting magnets to the point where a quench would occur. Therefore it is important that the cleaning is effective to better than 0.1%.

At position 4 is the LHC RF acceleration system. It will be composed of eight superconducting cavities and will operate at 400.8MHz [6]. There are two parallel systems so that protons and lead ions may be accelerated separately. This acceleration system is housed at the end of a straight section to allow another experiment to be inserted if necessary at a later date.

Position 6 will contain the beam dump apparatus which will be used to deal with the beams when they are exhausted. Each bunch train has a small gap of 3 μs left in it which allows the beam to be ejected from the ring at the appropriate time. The beam is then directed to a separate cavern 750m downstream where it will be swept backward and forward across the face of carbon dump blocks.

2.1.3 The Magnet and Cryogenic Systems

About two thirds of the length of the LHC contains superconducting dipole magnets, one of which can be seen in Figure 2.2. Twin apertures for the particle beams are found at the centre of each dipole. These apertures are surrounded by an iron return yoke and a

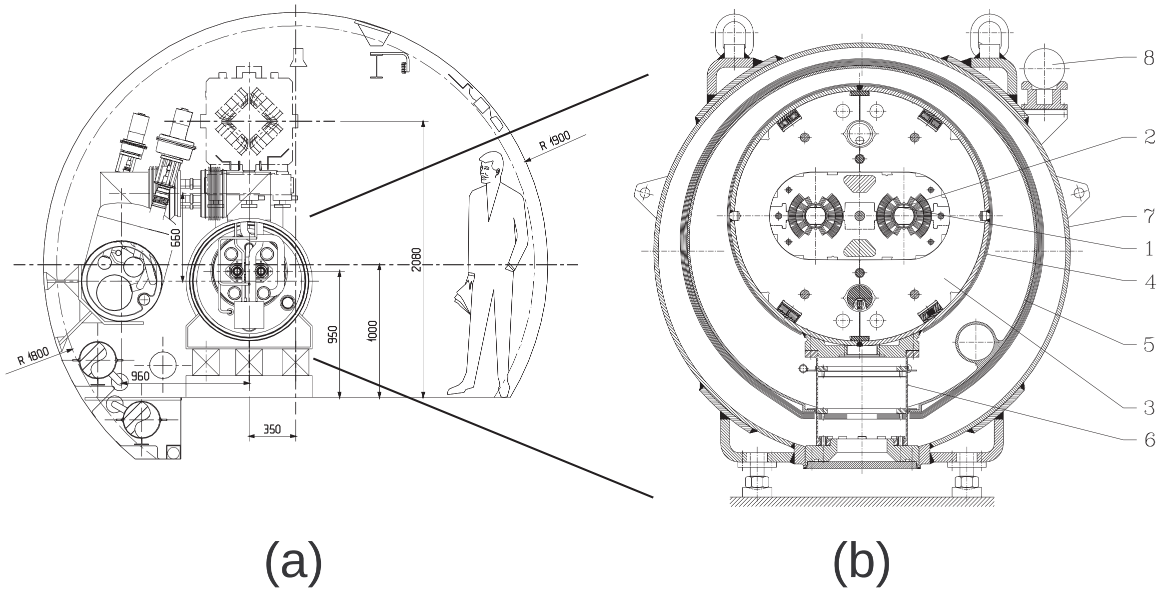

Figure 2.2: (a) A cross section of the machine tunnel showing the twin aperture dipole magnet. To the left is the cryogenic cooling feed system and on top a repositioned LEP quadrupole. (b) Close up of a dipole magnet and cryostat. (1) Beam Screen,(2) Cold Bore, (3) Cold mass at 1.9K, (4) Radiative insulation, (5) Thermal shield (55 to 75K), (6) Support Post, (7) Vacuum Vessel, (8) Alignment target.

cryostat. The cryostat maintains a temperature of 1.9K, which will allow the superconducting NbTi cable to pass the current necessary to achieve the required 8.4T field. The cryostat consists of a bath of superfluid ^{4}He pressurised to 1 bar. The inner cryostat is surrounded by further heat shields at 55K and 75K. All the cryogenic systems will be fed from the even numbered utility chambers using existing LEP [7] equipment.

2.2 The CMS Detector and its Physics Goals

The Compact Muon Solenoid (CMS) is one of two general purpose experiments for the LHC which have been optimised for the discovery and investigation of the Standard Model Higgs Boson over a very large mass range. It will also be possible to detect the signatures of other possible electroweak symmetry breaking mechanisms such as the light supersymmetric Higgs bosons. The CMS detector has very different physics goals for the periods of low and high luminosity.

2.2.1 High Luminosity

The search for the Higgs boson will dominate the high luminosity running. Standard Model predictions of electroweak observables depend on the mass of heavy objects such as the top quark and the Higgs boson via their contributions to higher order diagrams, or loop corrections. The LEP Electroweak Working Group have performed fits of a large

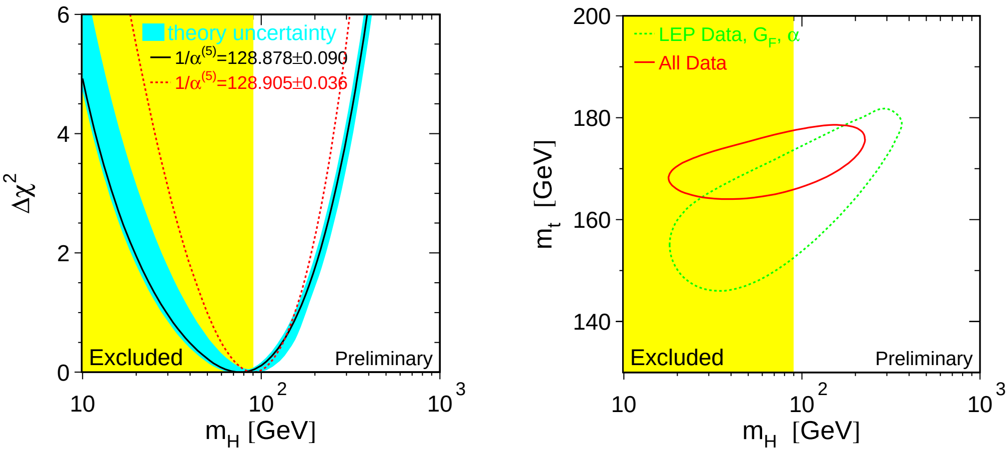

Figure 2.3 Predictions of the Higgs mass from fits to current experimental data (a) χ^2 as a function of m_H for the latest electroweak data [8]. The band represents an estimate of theoretical error from higher order corrections. (b) 68% confidence level contours in m_t m_H for fits to LEP data (dashed line) and all data including CDF/D0 (solid line).

number of observations to the Standard Model, including higher order corrections. These fits can be used to constrain the Higgs mass in the Standard Model. The Higgs boson mass has current 95% C.L. bounds of 89.2GeV < m_H < 262 GeV[8]. Figure 2.3 shows these bounds using data from the LEP experiments. In the intermediate mass range $m_H \approx 80$ to 150 GeV the $H \rightarrow \gamma\gamma$ decay mode, despite its small branching ratio, provides a distinctive signature for its discovery at the LHC. This has resulted in the

design of a very high resolution crystal calorimeter with excellent photon angular separation. Contours giving the cross-section times branching ratio required to give specified signal significances ($N_S/\sqrt{N_B}$) for this channel at low and high luminosities are shown in Figure 2.4. One year of high luminosity running could see a discovery over the whole intermediate mass range while three years running at low luminosity could see a discovery over a constrained mass range of 95 < m_H < 150 GeV.

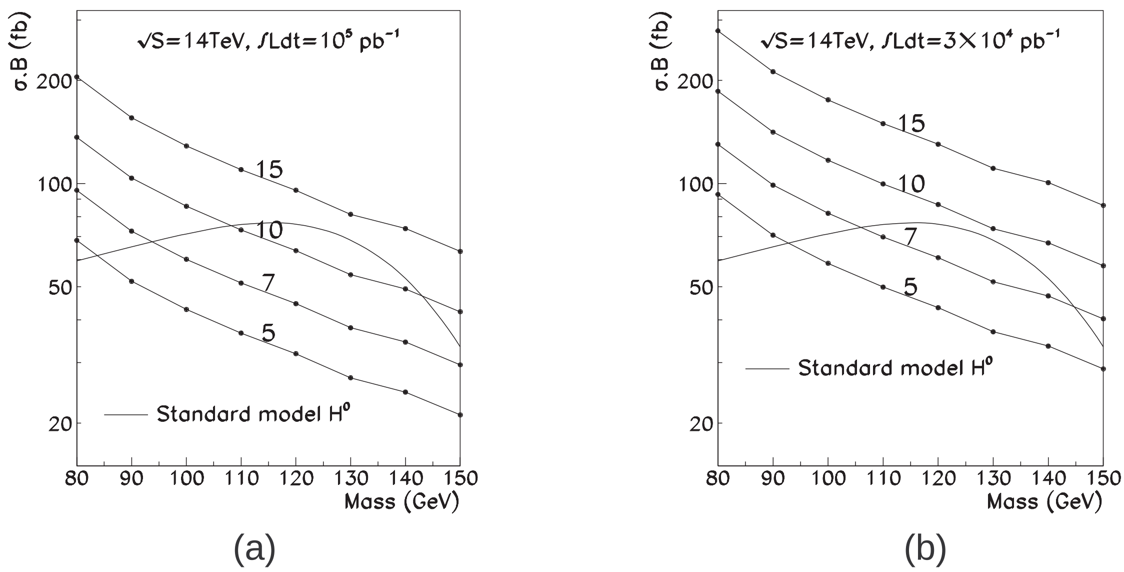

Figure 2.4: Higgs boson signal significances as a function of m_H against isa-significance contours for the decay $H\rightarrow\gamma\gamma$ for (a) high ($10^5 pb^{-1}$) and (b) low ($3\times10^4 pb^{-1}$) luminosity running.

2.2.2 Low Luminosity

The first two or three years of running will be at a reduced luminosity of $\approx 10^{33}$ cm^{-2} s^{-1}. During this period extensive studies of beauty and top physics will be undertaken as well as searches for the Higgs boson. B physics at CMS essentially means CP-violation studies defined by

$$\Gamma\left(B^0 \to f\right) \neq \Gamma\left(\bar{B}^0 \to \bar{f}\right) \qquad (2.1)$$

It has been shown at the Tevatron that hadron colliders can extract the channels

$$B \to J/\Psi K_S^0,\ J/\Psi K^{\pm},\ \text{and}\ J/\Psi K^{*} \qquad (2.2)$$

with good signal to noise ratios[2]. The LHC will produce between 10^{12} and 10^{13} $b\bar{b}$ pairs and this will allow CP-violation to be studied in these modes which have relatively small branching ratios $O(10^{-4}$–$10^{-7})$. Other topics will be studied in addition to CP-violation. These will include prompt photon production, anomalous gauge couplings and searches for very heavy Higgs bosons.

2.3 The CMS Detector

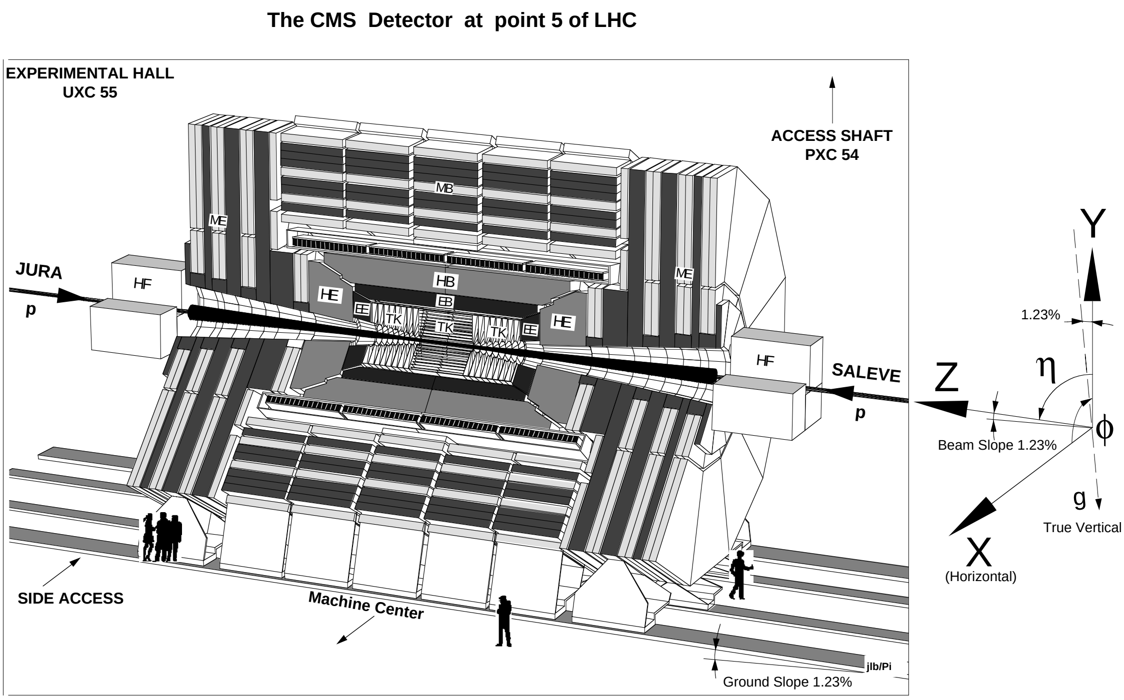

Figure 2.5: Overall view of the CMS detector.

The concept of a compact detector for LHC was presented in October 1990 at the LHC workshop in Aachen [9]. The requirement for a compact design led to the choice of a strong magnetic field generated by a solenoid. In March 1992, at the Evian meeting [10], a conceptual design of the complete detector was presented as an Expression of Interest by the proto-collaboration comprising 49 institutions. The design goals were defined as follows:

- a long superconducting solenoid, with a large radius such that both the central tracking and calorimetry can be contained in its bore and providing a high magnetic field (4T),
- a very good and redundant muon system,
- the best possible electromagnetic calorimeter (ECAL) consistent with the above,
- a central tracking detector that allows the reconstruction of charged particle tracks and a precise measurement of momenta,
- a robust and cost effective detector.

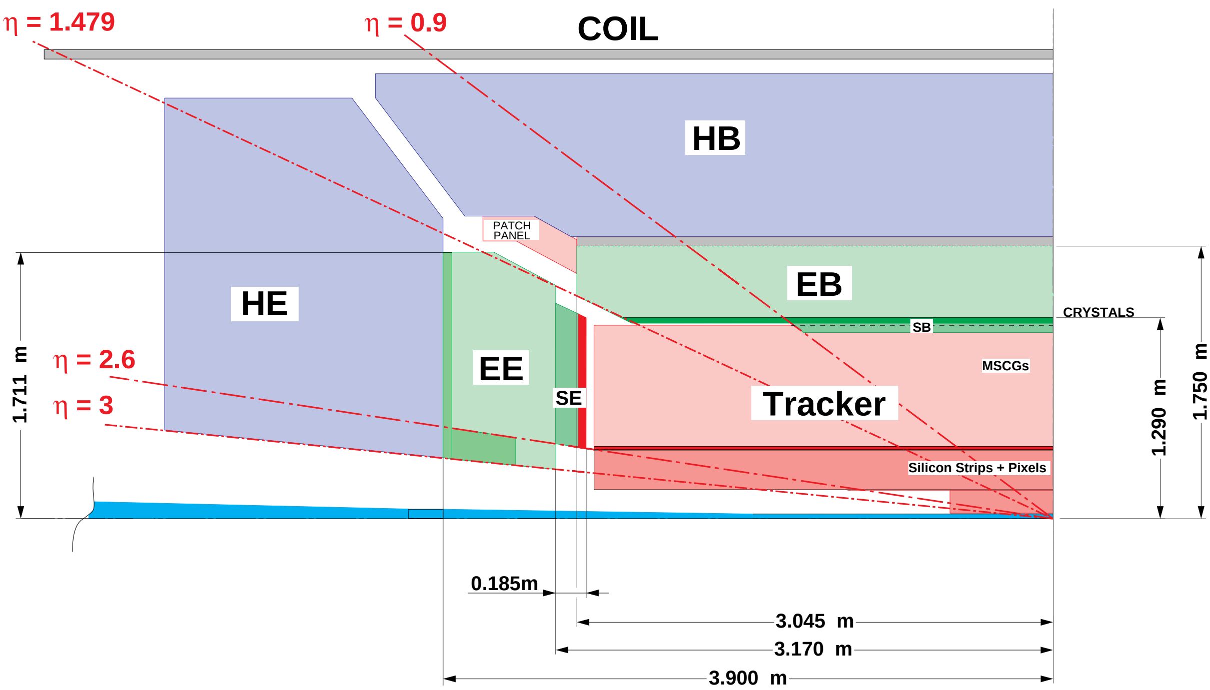

Figure 2.6: Schematic view of one quadrant of the calorimetry and tracking system.

In October 1992 a Letter of Intent signed by 443 members from 62 institutes was submitted to the LHC Committee (LHCC). On January 19th 1995 the open presentation of the CMS Technical Proposal [2] took place. The detector is now at an advanced stage of design and subdetector prototype testing.

A three-dimensional view of the CMS detector is shown in Figure 2.5. Figure 2.6 shows a longitudinal cut through the CMS detector but excluding the very forward calorimeters and the muon system. Here the geometry of the detector is described in terms of the z co-ordinate, which is parallel to the beam axis with the origin located at the nominal interaction point, and pseudorapdity η.

The CMS detector can generally be divided into a barrel region and two identical endcap regions. The central element of the CMS detector is a 13m long, superconducting solenoid generating a uniform magnetic field of 4 T. The magnetic flux is returned through a 1.5m thick saturated iron yoke instrumented with muon chambers. Located within the solenoid bore are the central tracker and both the electromagnetic (ECAL) and hadron (HCAL) calorimeters. The high magnetic field strength allows precision inner and muon tracking, and results in a large fraction of the relatively soft charged tracks from minimum bias events being contained in the innermost region of the tracker. This aids track reconstruction and reduces pile-up in the ECAL. The overall length, excluding the very forward calorimeters, will be 21.6m and the radius will be 7.5m. The detector will weigh approximately 12500 tonnes.

Magnet

The focal point of the design of the CMS detector is a superconducting magnet which can generate a uniform 4 Tesla field. This field strength is necessary to provide the bending power for the inner tracker and the muon chambers. The magnet is 13m long with an inner radius of 2.95m. Figure 2.7 shows the superconducting coil and also the return yoke. The return yoke is made of 1.8m thick iron and as well as returning the magnetic flux it is instrumented with muon chambers[12]. The total weight, including the coil, is ~12000 tonnes. The magnet is used as the principal support structure for all the other detectors.

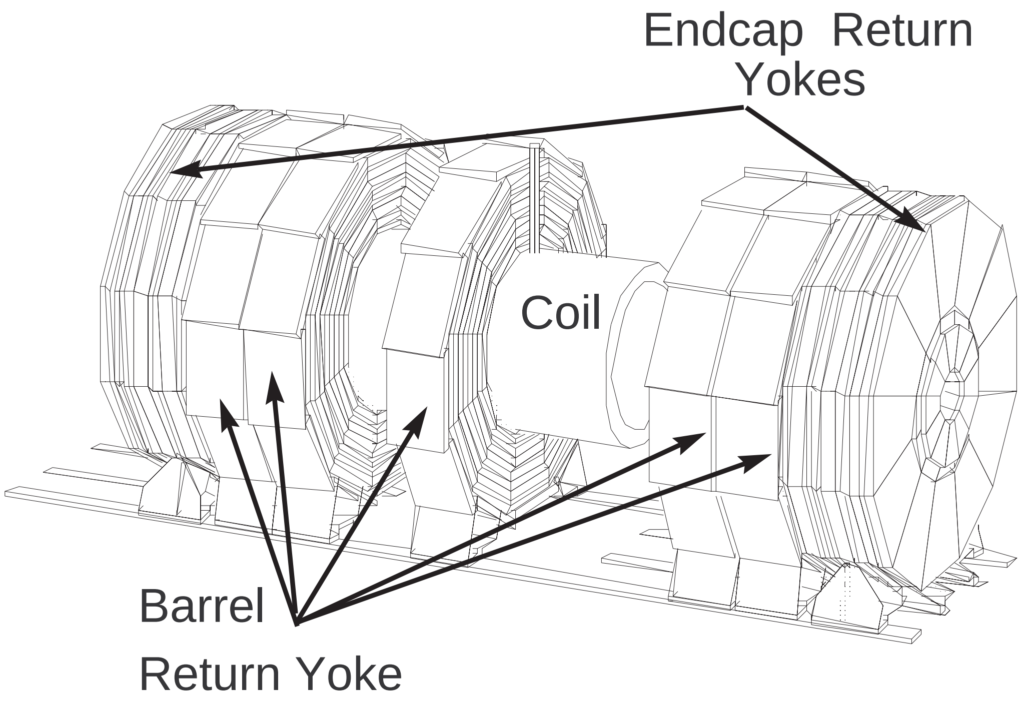

Figure 2.7: Three dimensional view of the CMS magnet. The yoke is shown open revealing the superconducting coil.

The cut away view of the coil and a ring from the barrel yoke is shown in Fig 2.8. The complete yoke will be composed a barrel of five such rings and also two endcap sections. The barrel yoke is a twelve-sided cylindrical structure 11m in length, subdivided into 5 rings of ~2.2m in length. The central ring, centred on the interaction point, supports the superconducting coil. Each barrel ring is made of 3 iron layers; connecting brackets hold them together and provide structural rigidity. Each endcap yoke is built from 3 independent discs which can be separated to provide access to the forward muon chambers. Due to the axial magnetic field the inner two discs must withstand a large attracting force and resist the large bending moments induced and are therefore much thicker than the outer disc. The vacuum tank is made of stainless steel and houses the superconducting coil. The superconducting coil is of a unique self supporting design[12] resisting the magnetic forces where they are produced, which reduces the stresses in the insulation. The diagram also shows the cryogenic system, which is used to keep the magnet below the critical quench temperature of 4.2K. The magnet will be assembled in a hall at ground level and after thorough testing it will be lowered into the access shaft ready for installation.

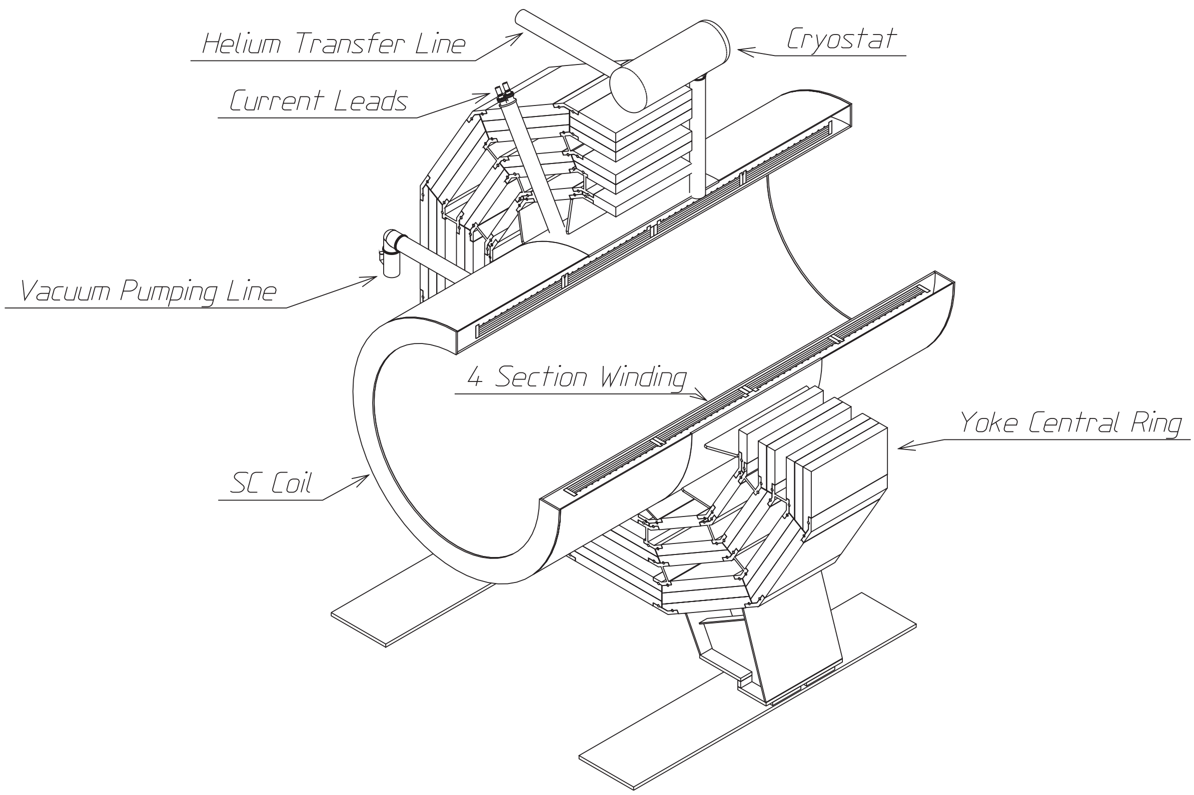

Figure 2.8: Cut-away view showing the exposed coil, yolk and support services.

2.3.1 Central Tracking

The central tracking system is designed to reconstruct isolated high p_T muons, electrons and hadrons with an efficiency that is better than 95%, and high p_T tracks within jets with an efficiency of better than 90% over a pseudorapidity range $0< |\eta| <2.6$. It will also enable a measurement of the z-coordinate of the primary vertex to be made. This is essential for efficient b-tagging.

The main problem for the tracker will be pattern recognition: it needs to be able to recognise the few tracks with a $p_T > 2$GeV from an average of 500 soft tracks superimposed upon them. In addition to the problem of pattern recognition the levels of radiation will be very high due to primary interactions around the collision region. A high flux of neutrons that originate from nuclear interactions in the electromagnetic calorimeter will also fill the tracker volume.

These considerations lead to an inner tracking system incorporating three complementary technologies, a combination of silicon pixel detectors (SPDs), silicon microstrip detectors (SMSDs), and microstrip gas chambers (MSGCs). The layout of the CMS tracker is shown in Figure 2.9. [13]. Each technology has high granularity and precision. The excellent granularity ensures efficient pattern recognition at high luminosity. The precision provides the best momentum resolution. Both the detectors and read-out systems are radiation resistant to enable them to withstand the high fluence of neutrons, photons, and charged particles in the tracking cavity.

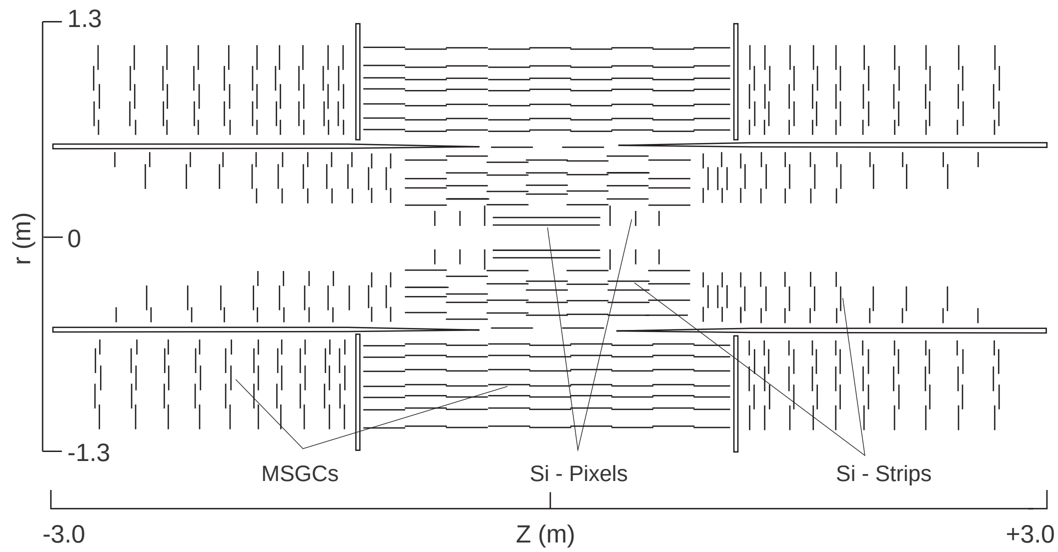

Figure 2.9: Schematic of the inner tracker showing the three technologies used. Silicon pixel detectors are followed by silicon microstrips and finally by microstrip gas chambers.

The entire tracker is contained in a cylindrical volume of 1.3m radius with a length of approximately 6m. The tracker is subdivided into barrel and endcaps. A momentum resolution of $\Delta p_T / p_T = 0.1 p_T$ (p_T in TeV) [2] is required for isolated charged leptons in the central rapidity region. This will allow the measurement of the charge of the lepton up to $p_T \approx 2$ TeV. It will also allow frequent in situ calibration of every cell in the electromagnetic calorimeter, needed to maintain the high energy resolution of the calorimeter, using the high rate of precisely measured electrons from W and Z decays.

A silicon pixel detector is situated closest to the interaction point. It consists of two layers in the barrel and three layers in the endcaps. It provides assistance in pattern recognition, leading to a much improved z-resolution in the barrel. The silicon pixel detector is placed in a very harsh radiation environment where it must withstand particle fluences in excess of 10^{14} n / cm^2. After about five years in this environment it may be necessary to replace the detector.

Surrounded the SPD are three layers of silicon microstrip detectors instrumenting the intermediate radial region between 20.5cm < r < 40cm. They provide at least three measurements in r-ϕ with a position resolution of ~15μm and two position measurements in the r-z plane with a resolution of better than 1mm [11].

The silicon microstrip detectors are in turn surrounded by planes of MSGCs. These consist of anode and cathode strips mounted on a glass substrate in an atmosphere of pure DME gas. They provide at least seven position measurements for high p_T tracks as well as three hits in r-z.

2.3.2 Electromagnetic Calorimeter

The primary function of the ECAL is the precise measurement of the energy of both electrons and photons, and in conjunction with the HCAL, the measurement of jets. The large solenoid bore enables both the ECAL and HCAL to be positioned inside the coil where their performance is not degraded by particle showers starting in the coil material. The choice of detection technique and design of the ECAL are largely determined by the desire to cleanly detect the intermediate mass Higgs decaying into two photons [15]. The natural width for the intermediate mass Higgs boson (80 – 140GeV) is rather small (< 10 GeV), and hence the observability of the two photon decay is strongly dependent on the electromagnetic energy resolution. Thus the benchmark against which the performance of the ECAL is measured is the di-photon mass resolution. The dependence of the di-photon mass resolution on the energy and angular resolution is given in equation 2.3

$$\frac{\sigma_M}{M} = \left[\frac{\sigma_{E_1}}{E_1} \oplus \frac{\sigma_{E_2}}{E_2} \oplus \frac{\sigma_\theta}{\tan(\theta/2)} \right] \qquad (2.3)$$

where E_1 and E_2 are the energies of the two photons in GeV and θ is in radians. The electromagnetic energy resolution is usually parameterised as:

$$\frac{\sigma_E}{E} = \left[\frac{a}{\sqrt{E}} \oplus b \oplus \frac{\sigma_N}{E} \right] \qquad (2.4)$$

where a is the stochastic term, b the constant term and σ_N the energy equivalent of noise. The energy resolution in the ECAL is dependent on intrinsic fluctuations in the shower process. A homogeneous calorimeter will have better resolution than a sampling calorimeter. A sampling calorimeter does not register everything that takes place so therefore these fluctuations are more pronounced. Two main processes contribute to the stochastic term, the first is shower containment and the second photostatistics. The most significant of the several processes that affect the constant term is the longitudinal uniformity of the light yield. The processes that contribute to these terms are discussed in more detail in chapter 3.

The LHC bunch crossing interval of 25ns dictates that the material must have a fast response time. The material must also be resistant to both neutrons and charged particles because of the radiation environment at the LHC. In addition a large geometrical acceptance, fine granularity and a large dynamic range are required.

Both fully active and sampling ECALs were initially considered. It is difficult to achieve a stochastic term of below $10\%/\sqrt{E}$ with a sampling ECAL. However, with many active media it is possible to achieve stochastic terms as low as $2\%/\sqrt{E}$. Following excellent results obtained during August 1994 with a matrix of 6×6 lead tungstate ($PbWO_4$) crystals the decision on the material for the electromagnetic calorimeter was taken. The small Moliere radius (2.2cm) and short radiation length (0.89cm) of $PbWO_4$, mean that the volume of material required to incorporate 25 X_0 is much less than with other commonly used scintillators. This leads to a compact design for the ECAL. In addition the fast emission time for the scintillation light (5 –15ns) means that most of the light can be collected within the bunch crossing time of 25ns, thus reducing the problem of signal pile–up. A more detailed description of the electromagnetic calorimeter is available in Chapter 3.

2.3.3 Hadron Calorimeter

The Hadron Calorimeter (HCAL) is situated between the ECAL and the superconducting solenoid coil. Together with the ECAL its primary functions are to measure the energies and directions of particle jets, and to provide hermetic coverage for accurate measurement of missing transverse energy. This leads to the following design requirements for the CMS hadron calorimeter system: good hermeticity, good transverse granularity, moderate energy resolution and sufficient depth for hadronic shower containment.

The HCAL consists of a barrel 9m in length with inner/outer radii of ~2 –3m which covers the pseudorapidity range to η = 1.3 – 1.5. Two endcaps increase the HCAL coverage to $|\eta|$ = 3.0 where the VFCAL takes over.

The HCAL is situated inside the magnetic field and it therefore must be built from non-magnetic components. A sampling calorimeter has been chosen which has copper plates as the absorber and plastic scintillator, read out with embedded wavelength shifting fibres, as the active medium. The copper plates are 4cm thick in the barrel and 8cm thick in the endcaps. The scintillator tiles are 4mm thick in both regions. The readout of the optical signal from the fibres is done with hybrid photodetectors [16] which can operate successfully in the radiation environment.

The barrel of the HCAL will be made of two identical sections, which will be bolted together in the centre of the detector. Each half-barrel consists of 18 identical wedges that are constructed out of flat absorber plates, orientated parallel to the beam axis.

The absorber plates are 50mm thick. The scintillator tiles in each layer are divided into towers with a lateral granularity of $\Delta\eta \times \Delta\phi = 0.087 \times 0.087$ for $|\eta| < 2$.

The body of the calorimeter is copper but the inner and outer plates are of stainless steel. The copper plates are bolted together in a staggered gap/absorber structure that ensures there is no projective dead material for the full radial extent of a wedge.

The endcap has the same 18 fold segmentation in ϕ. As in the barrel the inner and outermost plates are made of stainless steel for strength. The endcaps are composed of staggered copper plates bolted together in 10 degree sectors.

To ensure sufficient depth for hadronic shower containment in the barrel region a 'tailcatcher' [17] of two additional layers of scintillator is positioned either side of the first iron flux return layer. The tailcatcher increases the total calorimetry depth to a

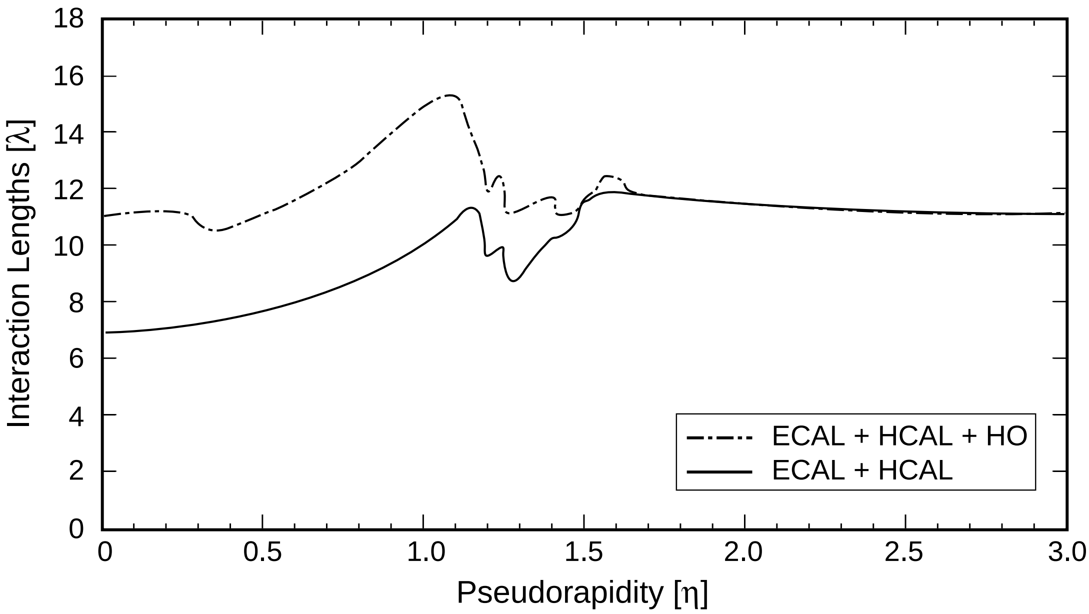

Figure 2.10: Total thickness in absorption lengths of the calorimeter system.

minimum of 10λ over the pseudorapidity range $0< |\eta| <3.0$. It improves the energy measurement for late developing hadron showers and hence the capability of the CMS detector to accurately define any missing energy in the event.

Owing to the extreme radiation conditions the endcap scintillator is not expected to last the LHC 'lifetime' of ten years. It will have to be replaced after about five years, the time being dependent on the integrated luminosity. No problems of this nature are foreseen for the barrel region.

2.3.4 Very Forward Calorimeter

The Very Forward Calorimeter, VFCAL, provides an improved measurement of the missing transverse energy. This is especially important for the study of top quark production and Standard Model and SUSY Higgs searches. The VFCAL also enables the identification of very forward jets. This is very important in searches for a heavy Higgs (M_H ~ 1TeV) boson. The production of the Higgs in this range, through the WW or ZZ, fusion mechanism, is characterised by two forward jets. Tagging these jets helps to suppress the large QCD, W, Z, and jets backgrounds [18].

Because of the exceptionally harsh radiation environment forward of $|\eta| = 3$ it is essential that the detector and its read-out be immune to induced radioactivity and insensitive to high neutron fluences.

The VFCAL is located at $z = \pm 11.10$m from the interaction point in both forward and backward directions [19] and it is designed to cover the pseudorapidity range $3.0 < |\eta| < 5.0$. The VFCAL is constructed of blocks of copper embedded with quartz fibres [20] that run parallel to the beam. High purity quartz is ideal for these working conditions as it is very radiation hard [21]. Charged particles hitting the copper absorber initiate electromagnetic showers which in turn produce Cherenkov light in the fibres. The light continues down the outside edge of the copper block where it is read out by a photodetector. To reduce the effects of radiation the photomultipliers and electronics are located to the sides of the calorimeter.

2.3.5 Muon Chambers

The detection of muons is of great importance because they provide some of the cleanest signals of a wide variety of new physics processes at the LHC. Therefore, the ability to trigger on and reconstruct muons at the highest luminosities and with a large angular coverage is central to the design of the CMS detector. The CMS muon system consists of a barrel region (0 < | η| < 1.3) which overlaps with two endcap regions (0.9 < | η| < 2.4). This enables identification of muons from p_T = 5GeV to several TeV in a large rapidity interval.

The purpose of the muon chambers is to provide muon identification, a trigger, and momentum measurements. It is important that the detector has excellent timing capability, a good position resolution and efficient track recognition. The CMS muon system uses three different technologies to detect and measure the muons[22].

In the barrel region the muon detector is based on a system of drift tube detectors (DTs) and resistive plate chambers (RPCs) that are arranged in four concentric ‘stations’. These stations are inserted in the iron flux return yoke, which also serves as the absorber for muon identification.

Figure 2.11 shows a transverse view of the four separate stations of the barrel muon system inserted into the magnetic return yoke. The barrel muon stations contain a total of 12 drift chambers. Eight of these chambers measure the r-ϕ coordinate and define the bunch crossing while the other four chambers measure the z coordinate. The RPC

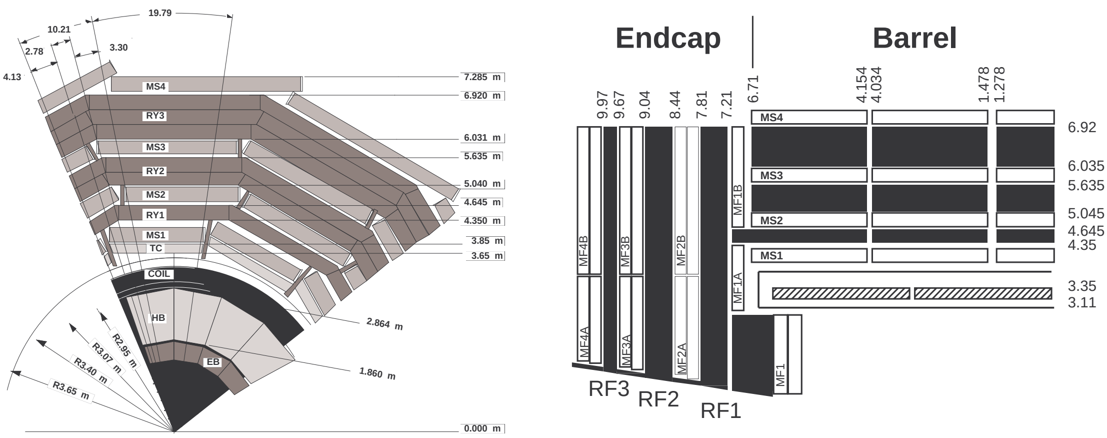

MF1B

Figure 2.11: Cross sections of the CMS muon system. On the left are the barrel muon stations MS1-MS4 and on the right those of the endcaps, MF1-MF4.

trigger modules have excellent timing and momentum resolution. They are used to provide a first level trigger for a range of muon p_Ts.

The muon stations in the endcaps are made of six layers of cathode strip chambers (CSCs). These are able to provide excellent spatial precision and timing information in the presence of a high magnetic field and at high particle rates. Each station provides a minimum of three sets of measurements on the muon track outside the central solenoid volume.

The muon system has to be flexible so as to handle a wide range of conditions including variations in luminosity, the magnetic field and chamber alignment. It must also have sufficient redundancy in order to deal with pile-up, punch-through, muon secondaries, backgrounds and noise.

2.4 Trigger and DAQ

The CMS Trigger and Data Acquisition System (TRIDAS) [2], must select and store events that may contain signals of new physics. The events of interest must be picked out from the vast background of Standard Model processes that will occur at the LHC. With the LHC running at its design luminosity of 10^{34} cm^{-2} s^{-1} there will be an average of 20 inelastic events occurring every 25ns, the beam crossing interval. This input rate of ~ 1GHz at high luminosity has to be reduced to less than 100Hz, the upper limit that could be archived for off-line analysis. Therefore a highly tuned TRIDAS is required to trigger on the characteristics of events that appear interesting. This triggering occurs in three stages.

The Level-1 trigger system bases its decisions on the local information concerning the presence of ‘trigger-objects’ such as photons, electrons, muons and jets in addition to the sums of visible and missing transverse energy. It operates on a subset of the data collected at each bunch crossing. It reduces the event rate to less than 100kHz which is the maximum rate that the Level-2 trigger can accept.

The events that pass the first level trigger are then passed on to a second level trigger. Here the first level thresholds are applied again but using the complete detector granularity. This will reduce the event rate by a factor of ten.

After a Level-2 positive decision which is again based on a subset of the data collected, the third level trigger will reconstruct the whole event and implement a final set of cuts to provide a reduction to an event rate of between 10Hz and 100Hz. The data can then be written to permanent storage for off-line analysis.

The CMS muon trigger is required to identify muons, measure their transverse momentum, p_T, and determine the bunch crossing from which they originated. Other ‘trigger objects’ are measured by the calorimeter trigger. The muon and calorimeter triggers work independently of each other for Level-1 and then together for levels 2 and 3 to reduce the event rate to an amount that is small enough to be stored.

3 ECAL Test Beam Studies

3.1 The Electromagnetic Calorimeter

3.1.1 Mechanical Design

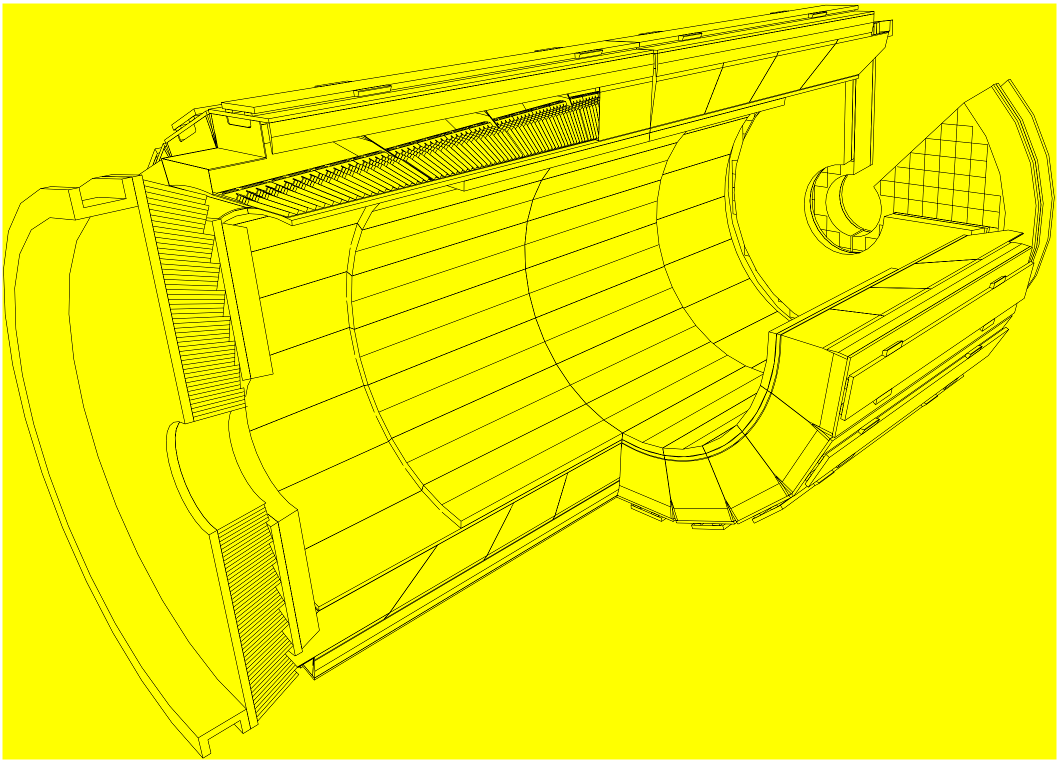

Figure 3.1: A 3-D view of the electromagnetic calorimeter.

The CMS electromagnetic calorimeter design described in this thesis is for that contained in the Technical Design Report [13]. The ECAL contains ~ 80,000 lead tungstate crystals arranged into a barrel region covering the rapidity region $|\eta| \leq 1.48$ and two endcaps covering $1.48 \leq |\eta| \leq 3.0$. The gaps between the barrel and the endcaps, which can be seen in Figure 2.6, contain the support manifolds and are used to route the central tracker and preshower cabling. Table 3.1 summarises the various design parameters for the CMS ECAL [13].

Parameter	**Barrel**	**Endcap**
Coverage	$\eta < 1.48$	$1.48 < \|\eta\| < 3.0$
r_{inner}, r_{outer} (mm)	1290, 1750	375, 1711
z_{inner}, z_{outer} (mm)	0, ±3045	3170, 3900
Granularity: $\Delta\eta \times \Delta\phi$	0.0174×0.0174	variable
Crystal dimension (mm^3)	$21.8 \times 21.8 \times 230$	$24.7 \times 24.7 \times 220$
Depth in X_0	25.8	24.7
Number of crystals	61200	2×10764
Total crystal volume (m^3)	8.14	3.2
Total crystal mass (tonnes)	67.4	25
Modularity	36 supermodules comprising of 1700 crystals (20 in ϕ, 85 in η)	~600 supercrystals containing 36 crystals

Table 3.1: ECAL design parameters.

3.1.1.1 The Barrel

The $PbWO_4$ crystals used in the barrel region have a projective geometry with the front face of each crystal having a square section of 21.8×21.8 mm^2. The length of crystals is 23 cm, which corresponds to 25.8 X_0. The crystals are mounted in a geometry off-pointing to the mean position of the primary interaction vertex with a 3° tilt in ϕ and η. This limits the effects of inter-crystal gaps, which if pointed at the vertex, would lead to tails in the measured energy distributions. The barrel will be constructed in two halves. Each half barrel will be constructed from 18 supermodules each subtending 20^{o} in ϕ. Each supermodule is comprised of four 'baskets' with an almost equal number of crystals. Baskets contain 400 or 500 crystals divided into alveolar submodules of 10 crystals. Figure 3.2 [13] shows a schematic of an alveolar submodule. A ferrule (not shown) positions the monitoring optical fibre inside each cell before crystal insertion. Once the 10 crystal subunits are inserted the alveoli are closed with an aluminium tablet. Foam on the bottom of the unit takes the pressure exerted by the tablet.

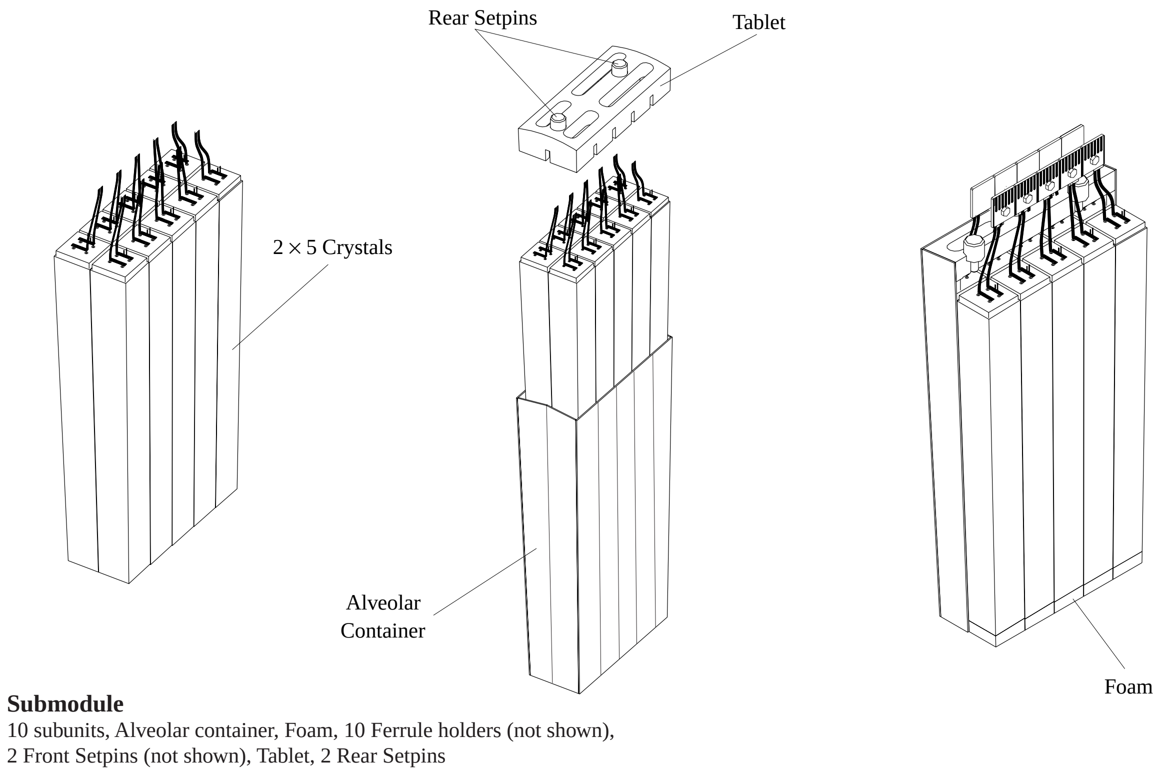

Figure 3.2: ECAL submodule assembly.

3.1.1.2 The Endcaps

The endcaps cover the pseudorapidity region from 1.48 to 3.0. The design of the endcaps foresees precision electromagnetic calorimetry measurements up to $|\eta| = 2.5$, matching the inner tracker system. However, crystals will be installed up to $|\eta| = 3.0$ in order to augment the energy-flow measurement in the forward direction.

The $PbWO_4$ crystals used in the two endcaps have a square front face of 24.7×24.7 mm^2, a square back face of 25.9×25.9 mm^2 and a length of 220 mm (24.7 X_0) with tapered sides providing an endcap with projective geometry. The basic detector unit is a glass fibre alveolar container, which houses a 6×6 array of crystals. 320 of these identical units, called supercrystals, will be used to cover approximately 90% of the endcap area. The remaining regions situated around the barrel/endcap transition and the perimeter, at $|\eta| = 3.0$, will be covered by subsections extracted from the basic 6×6 unit.

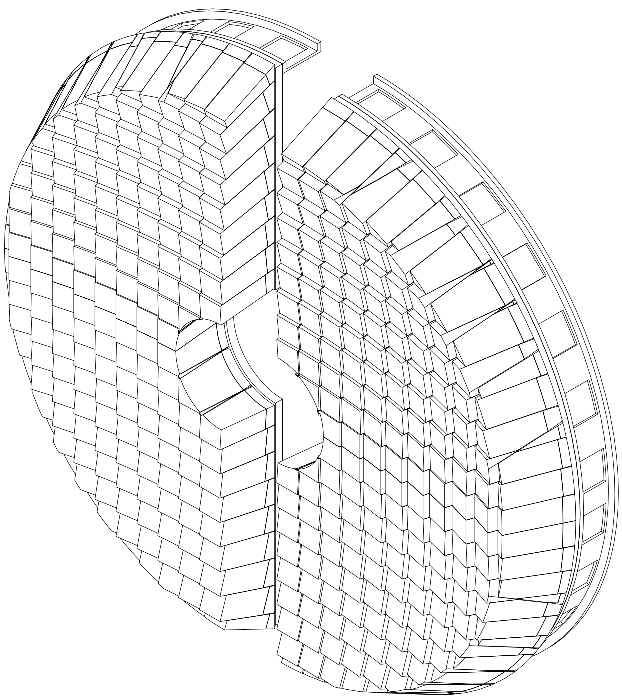

Figure 3.3: A single endcap with Dees apart.

3.1.2 The Radiation Environment

At a luminosity of $10^{34}cm^{-2}s^{-1}$ about 10^9 inelastic proton-proton interactions per second will generate a hostile radiation environment. Fig. 3.4 shows the integrated dose at shower maximum in the crystals and around the crystals at various values of pseudorapidity. These estimates are for an integrated luminosity of 5×10^5 pb^{-1} assumed to be appropriate for the first ten years of LHC operation. The integrated dose at shower maximum in the ECAL barrel crystals is about 4 kGy rising to 90 kGy and 200 kGy at $|\eta| = 2.6$ and $|\eta| = 3.0$ respectively. The numbers in bold italics are doses, in kGy, at shower maximum and at the rear of the crystals. The other numbers are neutron fluences immediately behind the crystals, in the space for the endcap electronics.

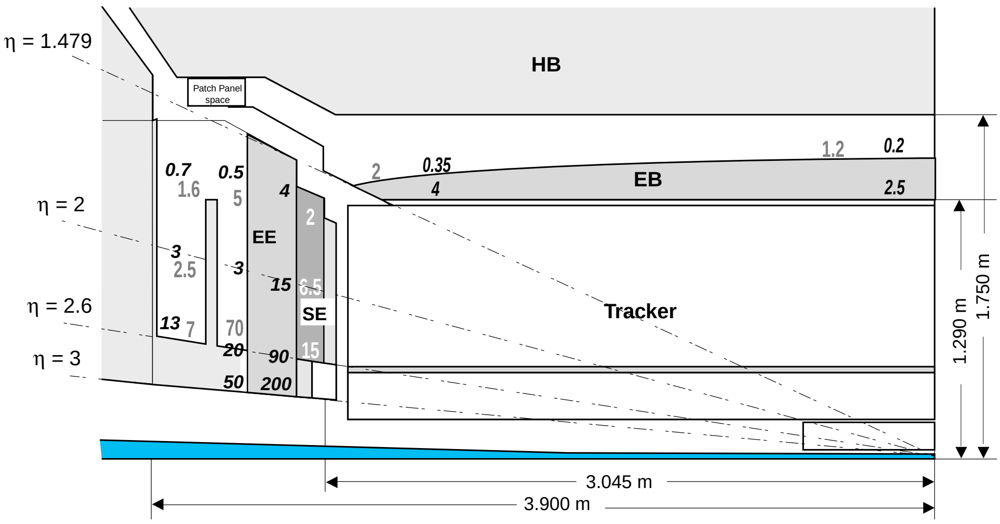

Figure 3.4: The dose and neutron fluence in and around the ECAL crystals as a function of pseudorapidity.

3.1.3 The Photodetectors

The properties of the photodetectors required for the CMS ECAL are as follows:

- A high quantum efficiency over the $PbWO_4$ scintillation spectrum (~ 440-520 nm) and some internal amplification to compensate for the rather low light yield of the crystals.
- Ability to operate in the 4 Tesla magnetic field of the CMS detector. This requirement rules out the use of photomultiplier tubes.
- Good radiation tolerance. The integrated neutron flux over 10 years of running would be $\leq 2 \times 10^{13}$ n / cm^2 in the barrel and 4×10^{14} n / cm^2 at $\eta = 2.6$[2]. In addition the photodetectors will be exposed to a large γ dose.
- The gain of the photodetectors must be stable if the constant term in the energy resolution is not to be degraded.
- The direct response to charged particles should be small. A large response to charged particles leads to degradation of the electromagnetic energy resolution due to longitudinal shower leakage into the photodetectors. The hadron energy resolution is also degraded if this requirement is not met.
- Small effective input capacitance in order to avoid excessive noise.

Conventional photomultiplier tubes are not suitable for use in a magnetic field because the magnetic field would cause the trajectories of the electrons to be bent and hence less charge would be collected. Silicon avalanche photodiodes (APDs) [23], which have been chosen for use in the barrel region, provide the required internal amplification and are sufficiently insensitive to charged particles. APDs are reversed biased diodes with an internal field of sufficient strength such that photoelectrons are accelerated and multiplied in an ‘avalanche’ process. The exact doping levels and thickness of the silicon layers may vary but figure 3.5 shows the general structure of an APD. It also shows how the electric field will vary throughout the device. Photons passing through the SiO_2 window convert in the p^{++} layer

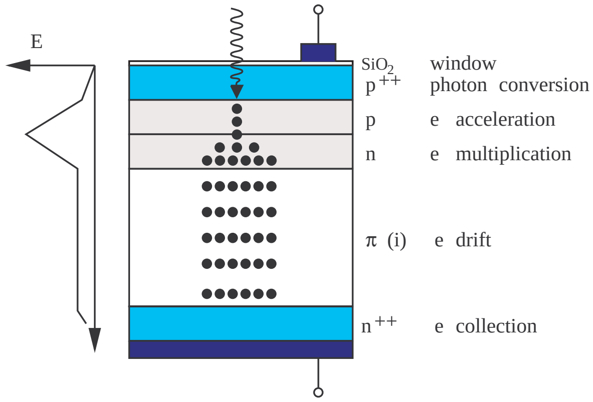

Figure 3.5: Generalised APD showing the electric field and the various silicon layers. The exact thickness' and doping will vary according to the manufacturer.

to photoelectrons, which are then accelerated and multiplied in the following p and n layers. This results in a gain, M, of between 50 and 200 depending on the bias voltage applied. Then there follows a drift region to reduce the overall capacitance of the device. Finally a highly doped n^{++} layer collects the electrons which then pass to the ohmic contact. Irradiation studies of APDs [24] show additional dark current being induced, leading to an increase in noise. Further details of the APDs used in beam tests of $PbWO_4$ crystal matrices are given in section 3.2.4.

The performance criteria for the photodetectors are the same for both the endcap and barrel regions with the exception of the magnetic field and the radiation environment. In the endcaps the photodetectors must operate in a harsher radiation environment and also have to operate in magnetic fields where the field vector is oriented at a small angle to the device axis. Vacuum Phototriodes (VPTs) [25] have been chosen instead of APDs for use in the endcaps. These devices have excellent radiation hardness, provide internal amplification, have a small response to charged particles and also have low noise.

3.1.4 Monitoring and Calibration

To maintain the CMS goal of 0.6% resolution at 100 GeV an inter-calibration of better than 0.25% is required. To achieve this, the crystals are calibrated both before installation and in-situ.

The initial calibration of the crystals will be carried out in beam tests before installation. The process will be carried out for single crystals and then repeated as the modules and supermodules are constructed. In order that the performance of the calorimeter is not to be degraded with time each crystal and the associated electronics chain will be monitored and the calibration updated. In-situ calibration is achieved by taking advantage of the high rate of isolated electrons from the decay of W and Z bosons at the LHC and matching the momentum measured in the tracker with the corresponding energy in the ECAL. This process will initially take a few weeks running at low luminosity. It will then be repeated at the beginning of each run. In addition a light injection system will be used to monitor changes in response with time.

3.1.5 The Preshower Detector

For the benchmark $H \rightarrow \gamma\gamma$ process, at high luminosity, uncertainty in the decay vertex position makes a large contribution to the reconstructed width. For this reason it is not satisfactory to use the mean interaction point to reconstruct this narrow two photon state. The preshower detector in the barrel region, which covers the pseudorapidity range $|\eta| \leq 0.9$, enables the direct measurement of the photon angle in the η direction. A measurement of the electromagnetic shower position is made at two depths; the first in the preshower detector, the second in the crystals themselves. This enables the photon trajectory to be reconstructed and, hence, the production vertex is located.

Two modes of operation are envisaged at the LHC: low luminosity (10^{33} cm^{-2} s^{-1}) and high luminosity (10^{34} cm^{-2} s^{-1}). At low luminosity when the number of superimposed 'minimum bias' events is small, it is possible to use charged tracks associated with the

Higgs to locate the longitudinal position of the primary vertex. Hence the barrel preshower is inserted only for the high luminosity phase

The barrel preshower consists of a single, two X_0, layer of lead converter followed by a single plane of microstrip detectors oriented to measure the z (or η) direction with a strip pitch of 1.8mm. The spatial resolution obtained with a prototype barrel preshower detector in beam tests is better than 300 μm above 50GeV [26]. Combined with the measured position resolution in a $PbWO_4$ crystal array [27] the angular resolution meets the design criteria of 50mrad/$\sqrt{E}$.

The function of the end-cap preshower detectors, which cover from $1.65 < \eta < 2.6$, is to provide γ -π^0 separation. At this rapidity the two photons from a π^0 decay have a small spatial separation and appear as a single shower in the crystal ECAL. Good separation is achieved by measuring the shower profile in two orthogonal directions. Two layers of lead converter are used: the first being two X_0 thick and the second one X_0. A single plane of silicon microstrip detectors follows each layer with the strips orientated orthogonally to one another. Unlike the barrel preshower detector the strip pitch is 1.9mm.

3.2 Introduction to the ECAL Test Beam Studies

The rest of this chapter will describe the testing of prototypes of the electromagnetic calorimeter to be used in CMS. These tests were carried out as part of a long period of R&D on the lead tungstate ($PbWO_4$) crystals planned for the CMS ECAL.

Throughout 1996 a series of beams tests of lead tungstate crystal matrices read out with silicon avalanche photodiodes (APDs) were carried out in the H4 beam of the SPS North Area at CERN. The H4 beam line is able to provide a range of electron beam energies from 15 to 150 GeV at rates of 2k/burst. The H4 beam has a low momentum spread, suitable for precision energy resolution measurements. The beam is asynchronous so a simple trigger system based on plastic scintillators was required.

The response of the calorimeter to irradiation has been investigated and a study of the electromagnetic energy resolution achieved with the prototype calorimeter has been made.

3.2.1 The H4 Test Beam Setup

The crystals used in the beam tests were truncated pyramids with a nominal length of 230mm (25.8 X_0) and a 20.5 × 20.5 mm^2 front face, projective to a point 1430 mm from the front surface. This closely approximates to the crystals at $|\eta| = 0$ in the baseline design. The crystals were placed in a wooden, thermally insulated and light-tight box on a remotely controlled moving table. The table was able to rotate the crystals about two perpendicular axes, θ and ϕ, both perpendicular to the beam, at a distance of about 1465mm from the surface of the crystals. The table could also be moved horizontally, transverse to the beam, and vertically, to modify the angle of incidence in both planes. The crystal axes were tilted by 3° to the beam direction in both transverse coordinates, to reproduce the planned configuration in the CMS ECAL.

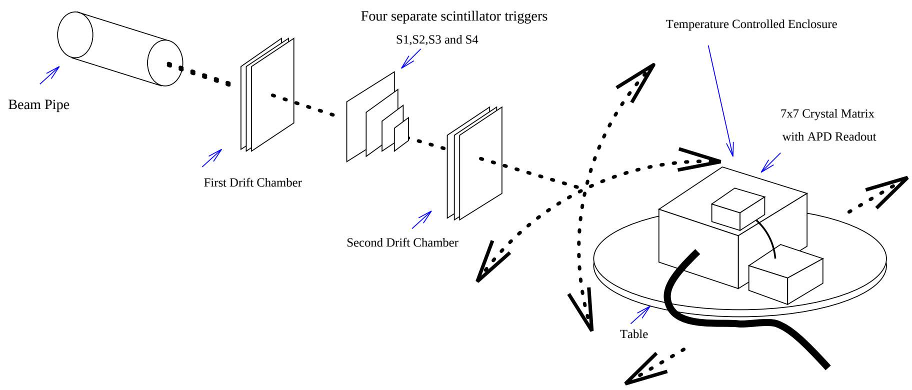

Figure 3.6: Isometric view of the H4 testbeam apparatus showing the movable table, drift chambers and trigger system.

In front of the box were placed a series of scintillation counters. Two orthogonal planes of scintillation fingers were used for adjusting the beam position. Additional counters provided information used off line for rejecting beam halo events. The trigger used for the majority of the data taking was a single coincidence defining a 20 × 20mm^2 spot, which corresponded well to both beam size and the front face of the crystal. Drift chambers gave a measurement of the impact point of beam particles with an error of approximately 225 μm. Figure 3.6 shows an isometric view of the H4 test beam arrangements. The configuration of the crystal matrix, monitoring and readout electronics is shown in Figure 3.7.

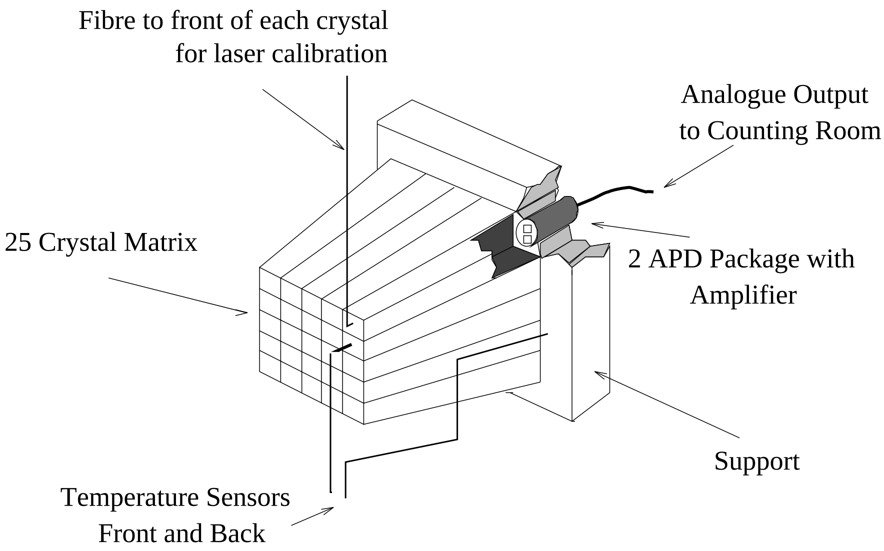

Figure 3.7: H4 Crystal matrix with monitoring and electronics.

3.2.2 Temperature and Voltage Control

The temperature of the test beam setup had to be carefully stabilised as both the scintillation light yield of the crystal and the gain of the APD are temperature dependent [28]. The variation in scintillation light is approximately -2% / °C and in APD gain is approximately -4% / °C.

Inside the box the four sides of the crystal matrix were in thermal contact with water cooled copper plates. The preamplifier and bias control circuit boards were positioned immediately behind the APDs mounted on the rear face of the crystals and were also in direct contact with water-cooled copper bars. The cooling water came from a temperature controlled water bath. The temperature of this water was maintained at 18°C. Additional cooling was provided in the form of heat screens which covered most of the interior surfaces of the box containing the crystal matrix. These screens consisted of 0.5mm thick aluminium sheets sandwiching a central aluminium plate 4mm thick. This plate was cut with zig-zag channels through which water was passed. This cooling water also came from a temperature controlled water bath.

The temperature of both the crystals and APDs were monitored continuously and written to tape. The temperature of the system could be monitored with an accuracy of approximately 0.01°C. The dominant effect on temperature stability of the system was diurnal fluctuation. The magnitude of this day-night fluctuation was approximately 0.15°C (peak to peak) [27].

The temperature variation on the front face of the crystals was about 0.05°C. This is due to the absence of the heat sources from the preamplifier and line driver which are present at the back of the crystals. Hence the gain variations caused by the changes in temperature should be almost entirely due to the sensitivity of the APD gain to temperature, rather than the temperature dependent light output of the crystals.

The high voltage on the APDs was also monitored and written to tape. The voltage monitoring was precise to ± 0.1%. The supply was found to be so stable that any effects from fluctuation in the voltage could be considered negligible [29].

3.2.3 Calibration and Monitoring

During the 1996 beam tests the calibration was monitored with a short pulse of light that was injected into the front of each crystal via an optical fibre. A red LED light source with peak emission at 660nm was used to generate a pulse of length 30ns, which was incident upon a silicon photodiode. A continuous feedback of signal size, via the photodiode, enabled stabilisation of the pulse to better than 0.1%. During the year both red (λ=676nm) and green (λ=532nm) lasers and a wide spectrum xenon flashlamp system were also tested. The xenon lamp used a rotating diffraction grating to provide four different wavelengths (420, 550, 600, 750nm). Only the LED system achieved enough stability to allow tracking of the calibration changes due to radiation damage with the required precision.

3.2.4 Readout and Electronics

The characteristics of the two types of APD used for light detection during 1996 are shown in Table 3.2. The signals from these APDs were fed into fast, low noise preamplifiers. These preamplifiers were designed around a high performance JFET and had a peaking time of 35ns and a measured noise of about 1200 electrons when connected to the EG&G APD. The measured noise increased to 2500 electrons when they were connected to the Hamamatsu device.

Each APD was followed by a completely independent electronics chain and separate ADC channels.

	EG&G	**Hamamatsu**
Size	$5\times5mm^2$	ϕ =5mm
Capacitance [pF]	30	325
Typical operating voltage [V]	400	150
Excess noise factor (M=50) [F]	2.2	2.0
1/M×dM/dT (M=50) [%/°C]	-3.5	-2.3
1/M×dM/dV(M=50) [%/V]	2	15

Table 3.2: APD Characteristics.

3.2.5 Crystal Preparation

When the crystals were delivered to CERN they were visually inspected and measured geometrically. This was followed by an extensive series of quality checks that included measurements of light yield, of optical absorption as a function of wavelength and also of longitudinal uniformity. Each crystal was wrapped using Tyvek[1] sheets of 150±50µm thickness. Tyvek is a white reflective paper made by DUPONT. Holes were left in the Tyvek on the end faces for the APD, two temperature sensors and three optical fibres per crystal.

3.3 Energy Resolution

This section presents an analysis of data from the September 1996 test beam. During this period the matrix consisted of a 7 × 7 array of $PbWO_4$ crystals of the nominal

[1] Tyvek is a trademark of Dupont.

size, read out by EG&G APDs. The energy resolution obtained when electrons were incident on each of the central 25 crystals is investigated and the contributions to the individual terms of the electromagnetic energy resolution parameterisation are studied.

3.3.1 Analysis Procedure

The intercalibration of the lead tungstate crystals was established using a 50 GeV electron beam. Runs of 40k events were taken with a $20 \times 20\text{mm}^2$ trigger centred on each of the 49 crystals in turn. The centre of each crystal was located with respect to the drift chamber coordinates by finding the point of maximum signal in the crystal. It is possible to reproduce this procedure with a precision of better than 0.1mm. Then a $4 \times 4\text{mm}^2$ region about this central point was identified. A Gaussian fit to the energy seen in each crystal provided a relative calibration value. This procedure was repeated for each of the 49 crystals.

The calibration runs were followed by a series of energy scans. Runs of 100k events were taken with the electron beam energy set to 15, 25, 35, 50, 80, 120, and 150 GeV in turn for each of the 25 inner crystals in the matrix. An electron incident normally on the centre of a $20.5 \times 20.5\ \text{mm}^2$ crystal face will deposit approximately 84% of its energy in that crystal [30]. Therefore when energy resolutions are calculated a 'sum of nine' crystals is always taken. This allows more than 99% of total energy to be included.

Figure 3.8 shows the energy summed in the 3×3 array of crystals centred on crystal 1283. By using a $4 \times 4\text{mm}^2$ region the effects of lateral non-uniformity and calibration are largely excluded. It also excludes the need to correct for the varying fraction of average lateral leakage out of the 3×3 array which would be necessary in a complete reconstruction algorithm. The width of the sum of nine was found from a $\pm 1.5\sigma$ Gaussian fit to the distribution peak.

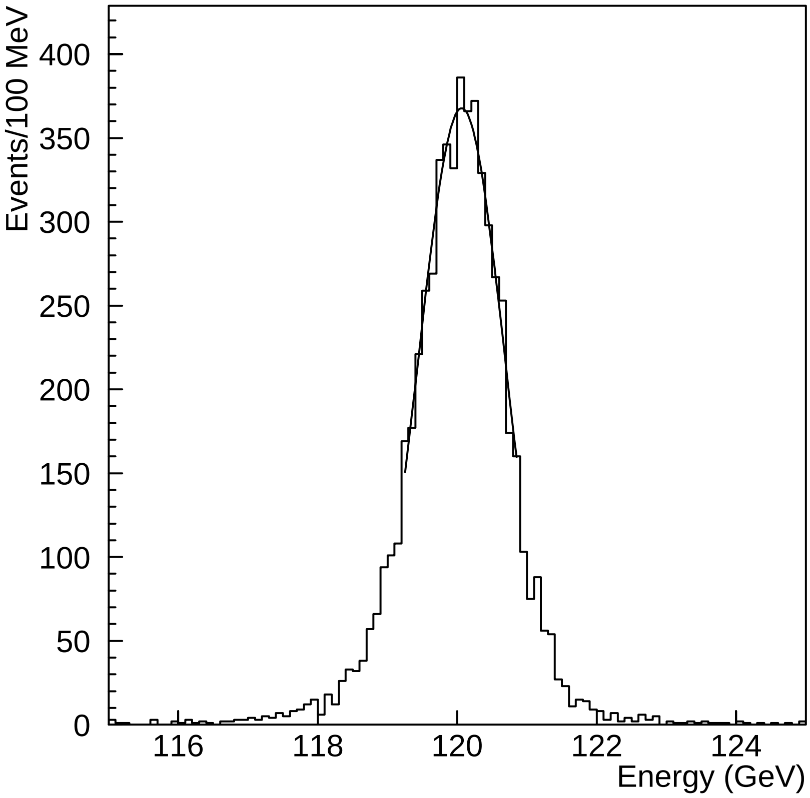

Figure 3.8: Energy summed in a 3×3 array of crystals for 120 GeV electrons incident in a 4×4 mm^2 region about the centre of the struck crystal.

The September data were analysed to extract an energy resolution function of the form:

$$\left(\frac{\sigma}{E}\right)^2 = \left(\frac{a}{\sqrt{E}}\right)^2 + (c)^2 \qquad (3.1)$$

after quadratic subtraction of the measured noise (see section 3.3.2). This was generally between 120 and 180MeV for a sum of 9 crystals. A range of different beam energies is required to calculate the energy resolution for a given crystal. The noise term was subtracted and then a plot of $1/E$ as a function of $(\sigma/E)^2$ was made.

Energy (GeV)	**$(\sigma / E)^2$**	**$\Delta((\sigma / E)^2)$**
15	1.4×10^{-4}	$\pm 1.2 \times 10^{-5}$
35	6.8×10^{-5}	$\pm 3.8 \times 10^{-6}$
80	3.3×10^{-5}	$\pm 2.4 \times 10^{-6}$
120	2.6×10^{-5}	$\pm 1.7 \times 10^{-6}$
150	2.4×10^{-5}	$\pm 1.5 \times 10^{-6}$

Table 3.3: Measured values of $(\sigma / E)^2$ for a range of energies.

Table 3.3 shows the values of $(\sigma / E)^2$ measured for a range of energies following noise subtraction and the errors on the measurements. A linear fit to $1/E$ as a function of $(\sigma / E)^2$ produces a result such as that shown in Figure 3.9. The fit yields a stochastic term of 4.47% / $\sqrt{E}$ and a constant term of 0.31%. The subtracted noise term was 135 MeV.

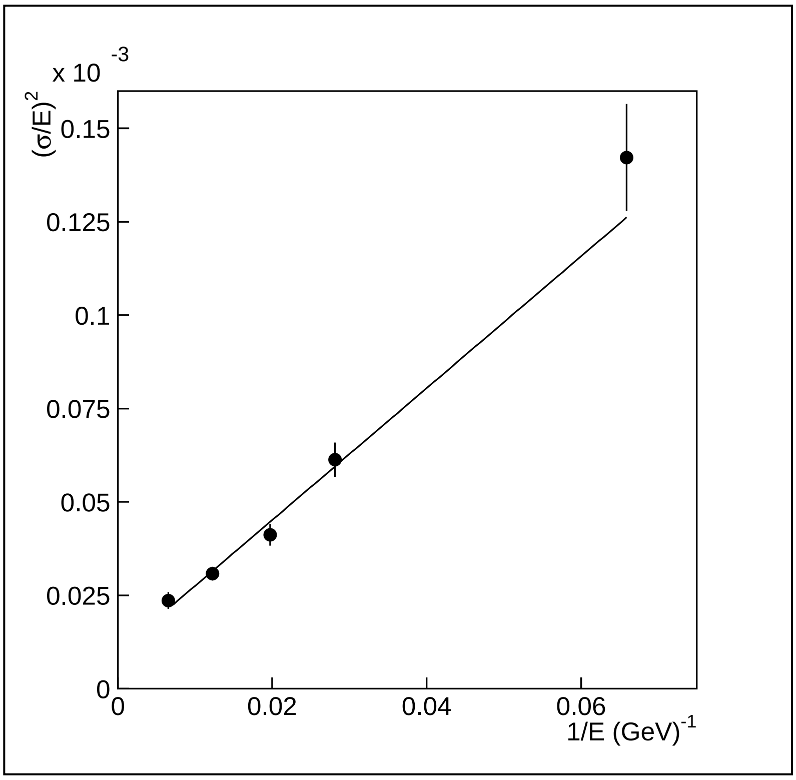

Figure 3.9: $(\sigma / E)^2$ as a function of $1/E$ for crystal 1283.

3.3.2 Noise Term

The noise term of the energy resolution was calculated run by run. The in-spill pedestals were summed using the same calibration as for the beam events. The width of this distribution was measured by a Gaussian fit to a region of $\pm 1.5\sigma$ about the peak. A typical reconstruction of the sum of 9 in-spill pedestals is shown in figure 3.10 The noise term was subtracted quadratically from the energy resolution before fitting to obtain the constant and stochastic terms.

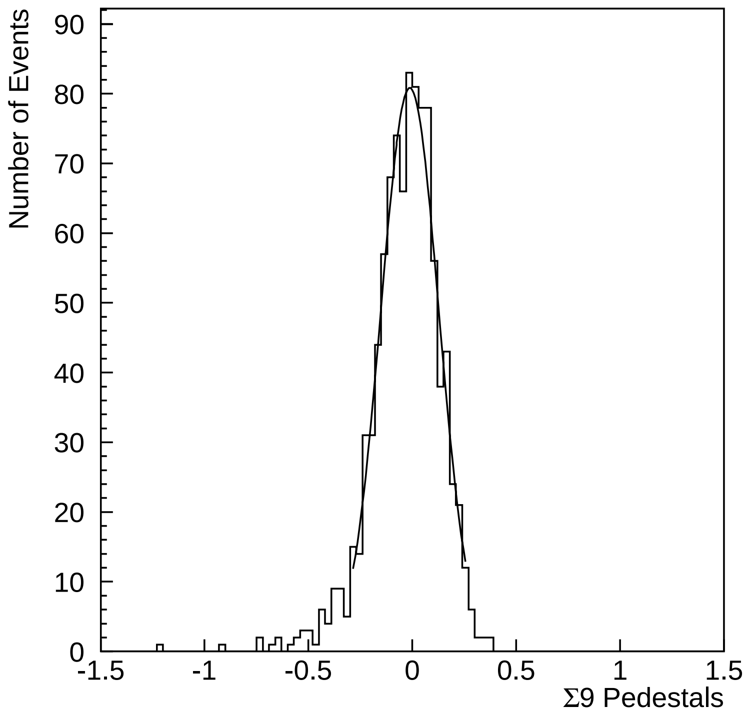

Figure 3.10: Reconstructed sum of 9 in-spill pedestals with a $\pm 1.5\sigma$ Gaussian fit.

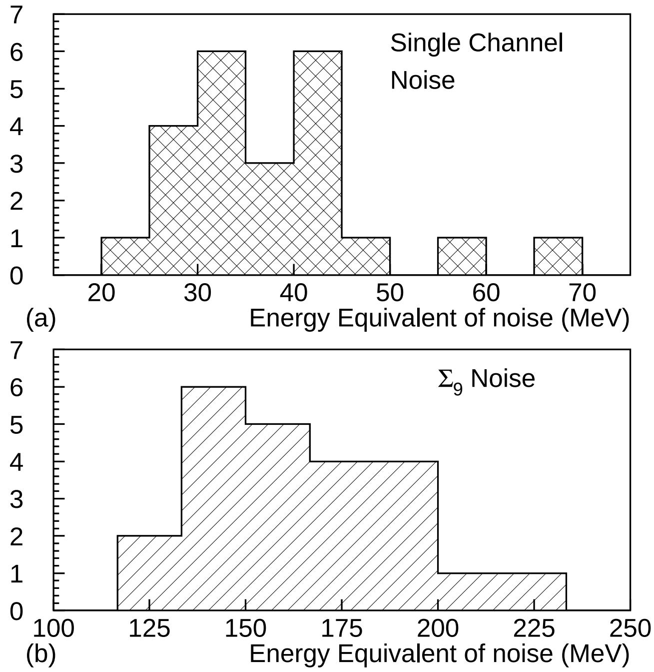

Figure 3.11: (a) Energy equivalent of noise for the crystals under test, (b) Energy equivalent of noise summed for 3×3 array.

Figure 3.11a shows the energy equivalent of noise for the 25 central towers. The noise is typically between 20 and 70 MeV per channel although a few noisy channels have larger values. Figure 3.11b shows the noise summed in a 3×3 array around each of the 25 central channels. The noise term is typically between 100 and 200 MeV. In each case it was found that the noise summed in 3×3 arrays was larger than the quadratic sum of noise from the 9 individual channels. This resulted from coherent pick-up inside the box caused by insufficient shielding around the preamplifiers.

3.3.3 Stochastic Term

Both shower containment and photostatistics contribute to the stochastic term. Assuming geometrically perfect crystals a GEANT [31] simulation [32][33] shows an expected stochastic contribution from lateral shower leakage of $\sim 2\% / \sqrt{E}$. Figure 3.12 shows the value of the stochastic term obtained for the central 25 crystals of the matrix. The values of the stochastic term for the September 1996 crystals range from $3.7\% / \sqrt{E}$ to $7.6\% / \sqrt{E}$ showing that photostatistics make a significant contribution.

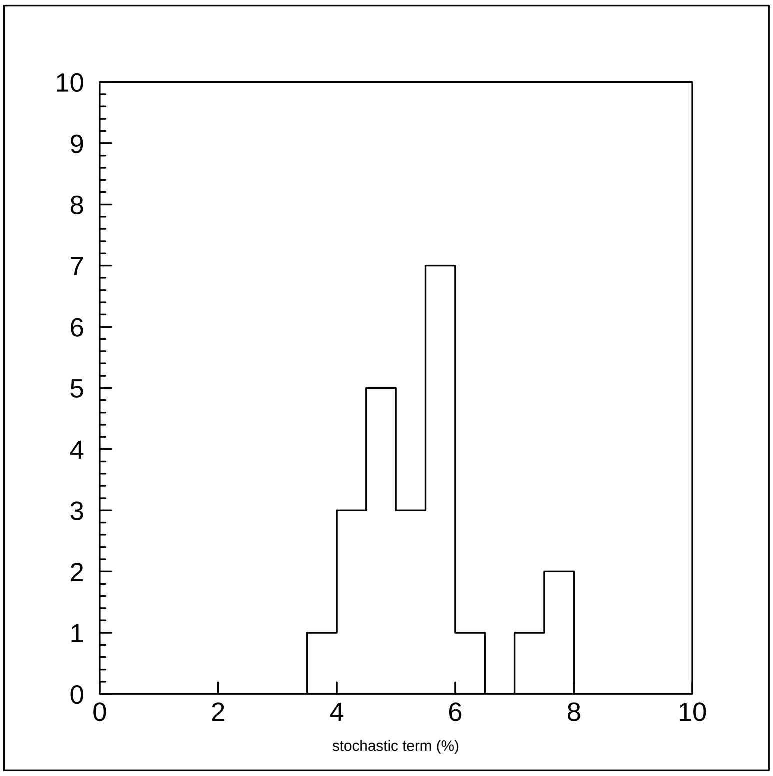

Figure 3.12: Stochastic terms for the 25 central crystals.

The contribution to the stochastic term from photostatistics has been measured with the LED monitoring system. Because the LED system was so stable (setction 3.2.3) the width of the response to the injected LED light, after noise subtraction, was assumed to be dominated by the photostatistics. In this case the contribution to the stochastic term from photostatistics (A_{photo}) is given by:

$$A_{photo} = \sqrt{\frac{\left(\sigma^2_{led} - \sigma^2_{noise}\right) \times k}{\mu_{led}}} \qquad (3.2)$$

where μ_{led} and σ_{led} are the Gaussian mean and width of the LED signal respectively in the struck crystal, σ_{noise} is the Gaussian width of the energy equivalent of noise in the struck crystal and k is the APD gain factor for red light (~1.2).

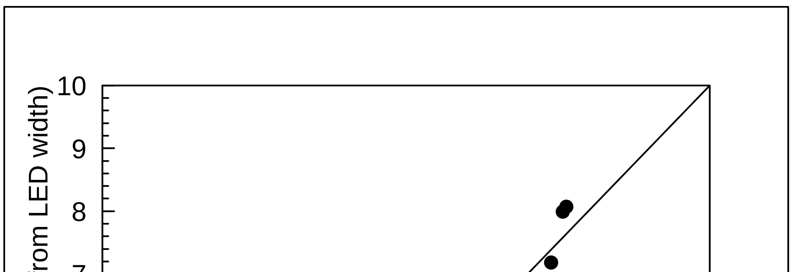

Figure 3.13: Measured stochastic term from LED as a function of the stochastic term evaluated from the energy resolution.

Figure 3.13 shows the measured stochastic term for the central 25 crystals versus the stochastic term predicted from the width of the LED signal. A good correlation between the measured stochastic term and the LED prediction can be seen indicating that the values of the stochastic terms measured in the test beam are well understood.

The photoelectron yield is the number of primary photoelectrons released by the APD per GeV. It is determined from Equation 3.3.

$$A_{photo} = \sqrt{\frac{F}{N_{photo}}} \qquad (3.3)$$

where N_{photo} is the photoelectron yield per GeV, F is the excess noise factor and A_{photo} is the contribution to the stochastic term from photostatistics.

It is envisaged that the final specification for APDs used in the CMS experiment will be to use two APDs on each crystal, double the area used in these tests. From Equation. 3.3 it can be seen that increasing the number of photoelectrons by a factor of 2 will result in the photostatistic contribution to the stochastic term being reduced by a factor of ~1.4.

3.3.4 Constant Term

There are several processes which contribute to the constant term, the second term in the energy resolution parameterisation. The most significant is the longitudinal uniformity of the light yield, and to a lesser extent, intercalibration error, longitudinal shower leakage into the APD and the momentum spread of the beam.

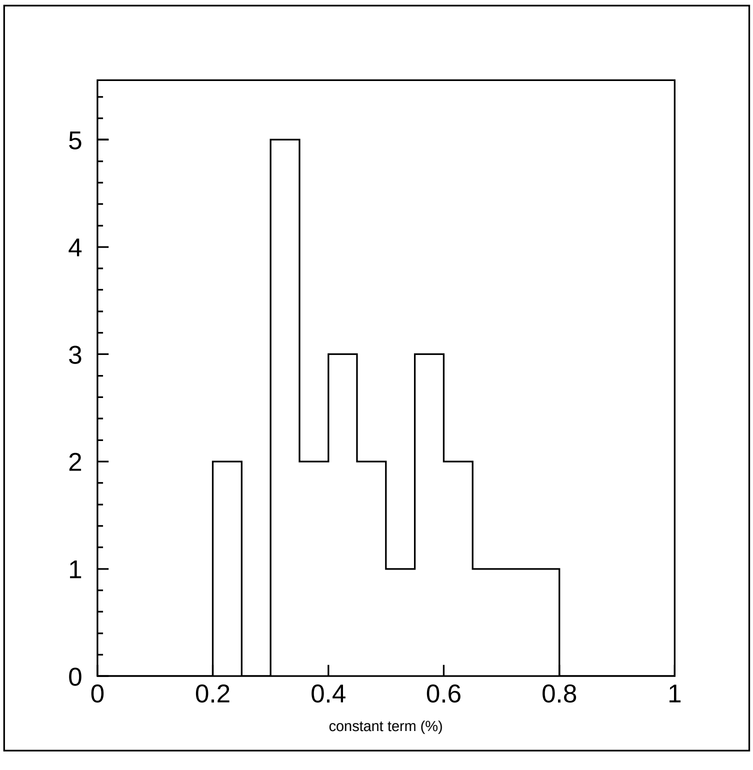

Figure 3.14 Measured constant term (%).

Figure 3.14 shows a histogram of the fitted constant terms for the central 25 crystals. The modal value obtained was ~0.3%, slightly higher than the 0.2% constant term predicted by a GEANT Monte Carlo simulation [33] of shower energy deposition with a uniform longitudinal response. The differences between the Monte Carlo prediction and the values obtained experimentally are due to the combined effects of lack of a uniform longitudinal response, the beam $\Delta p/p$ (nominally 0.1%), intercalibration errors and shower leakage into the APD.

3.4 Radiation Damage Studies

3.4.1 Introduction

Although lead tungstate is intrinsically radiation hard, non optimised crystals do suffer from radiation damage [13]. Extensive R&D has been carried out to help gain a better understanding of this problem. Tests carried out in 1995 [34] showed that radiation damage, causing loss of detected light, could pose a serious problem for the CMS ECAL even though it saturates after an integrated dose of a few kilorads. The damage anneals with relatively short time constants so that the calibration is subject to continual fluctuations. At room temperature the dominant time constant is approximately one week [27]. The CMS ECAL group have therefore adopted the simple strategy of ensuring that R&D efforts are focussed on the development of crystals that are less sensitive to damage. Any residual damage must be followed and corrected for using a precision monitoring system.

Therefore one of the main issues for the 1996 test beam programme was the further study of radiation damage using new crystals, new APDs and an improved test setup. Comparative studies were carried out in the H4 test beam of $PbWO_4$ crystals from three sources: Bogorodisk in Russia, SIC in China and Kharkov in the Ukraine. Most of the crystals were from the Russian production facility. Stability studies were carried out on these crystals by firing a beam of 120 GeV electrons into the centre of the crystal under investigation, at a fixed rate and with no changes to the external conditions. It should be noted that the actual radiation doses in the CMS detector will be far higher than the doses received by the crystals in the test beam.

During the study carried out in August 1996 the beam was centred on crystal 1283 for thirty hours. It was decided to examine the effect of this on the eight crystals surrounding 1283. Ideally information about the effects of radiation upon these crystals would have been obtained by running for thirty hours with the beam centred into each crystal in turn. However the constraints of the test beam programme meant that this was not possible. Information about the studies carried out on crystal 1283 can be found in [29] while this thesis describes the analysis of the surrounding eight crystals.

3.4.2 The Test Beam and the August Crystal Matrix

3.4.2.1 Test Beam Information

Eight of the 49 crystals in the 7×7 matrix were studied. These were the eight crystals surrounding crystal 1283. Only runs of 100k events were used. These runs were triggered on the two scintillators, S1 and S2. S1 and S2 are used to define the beam: S1 is 5×5 cm^2 and S2 is 2×2 cm^2. This resulted in a fairly narrow beam. Drift chambers gave a measurement of the impact point of beam particles with an error of about 250 μm. The rate was 15k/burst where a burst = 2.2 seconds during a 14.4 second SPS cycle.

3.4.2.2 August Crystal Matrix

The stability study was carried out on 14th and 15th August 1996 using a 7×7 matrix of $PbWO_4$ crystals. The crystals studied were the eight crystals, from Bogorodisk, surrounding crystal 1283 which came from SIC in China. Crystal 1283 received 640 rads in 30 hours. This was at a rate of 1.5k/burst with the exception of the first two runs and the final two runs, which were at a rate of 2k/burst.

Table 3.4 shows the position of the irradiated crystals in the August matrix viewed from the back.

1279	1121	1291	1297	1298	1056	1113
1114	1319	1041	1281	1278	1325	1115
1116	**1292**	**1117**	**1051**	1057	1295	1118
1120	**1293**	***1283***	**1045**	1050	1296	1131
1132	**1294**	**1288**	**1264**	1049	1268	1134
1135	1318	1270	1273	1043	1314	1138
1274	1276	1277	1280	1290	1286	1287

Table 3.4 August Crystal Matrix

3.4.3 Analysis Procedure

The beam was centred on crystal 1283 but information was required about the surrounding crystals. This presented some difficulties in obtaining accurate information about the eight crystals in this study. It was necessary to try several techniques before the method described here was decided upon.

The beam data was used to locate the central position of crystal 1283 for each run. This was done by plotting the response of the central crystal to the beam as a function of position, the maximum response occurring in the centre of the crystal. The ideal method of studying the response of the eight crystals would be to look at events in the centre of each crystal. However, in this case there would be few events. Therefore another method had to be chosen. The response to particles hitting $16mm^2$ regions in 1283 was studied. The area chosen was as close as possible to the position of the crystal being studied but far enough away from the edge of crystal 1283 to avoid any edge effects. This is shown in Figure 3.15. These pixels were then used to extract the response to the beam signal in the eight crystals around 1283. It was only the changes due to the radiation damage that were being followed so absolute measured values were not important.

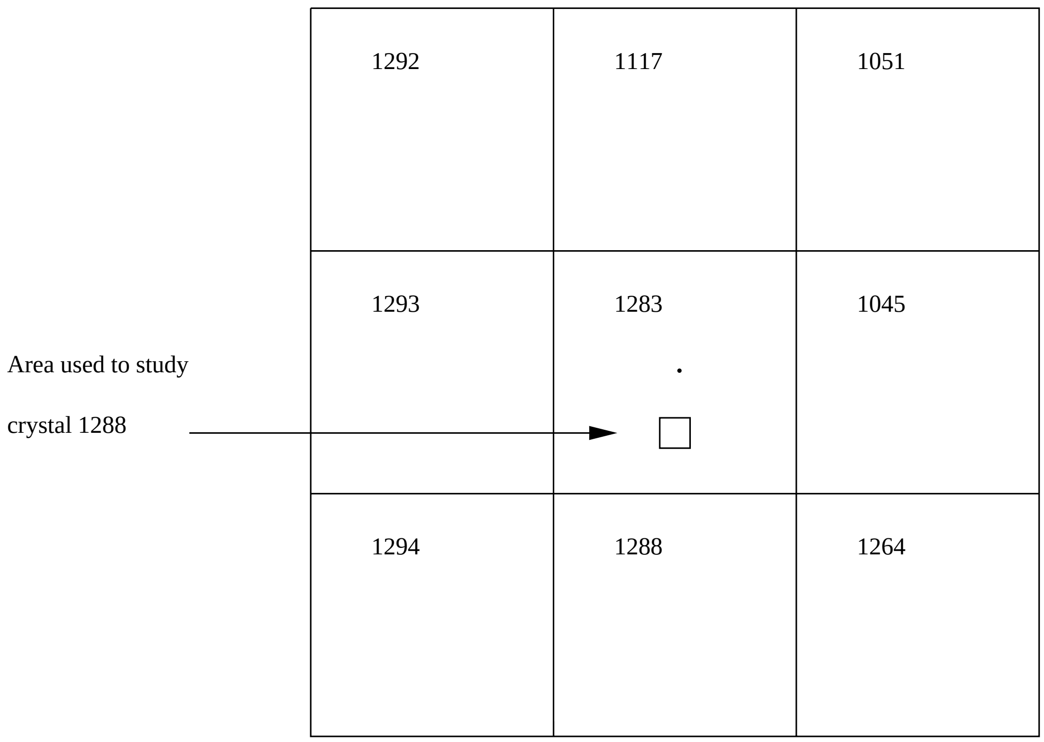

Figure 3.15: Showing the pixel in crystal 1283 used to study the effects of radiation in crystal 1288.

3.4.4 Dose Calculations

The measurement of the delivered dose in the test beam carries some uncertainties. The main uncertainty arises from the lateral spread of the dose. The lateral spread is caused by the shower width and by the lateral extension of the beam. The lateral size of the beam is approximately 15mm, which is somewhat larger than the shower width, although it varies with the beam file settings. The shape is known from beam chambers within the 20×20 mm^2 (S2) trigger area that has been used for irradiation. The number of incident electrons is counted in a scaler using a discriminated signal taken from the same trigger counter.

To make a precision calculation of the dose using a shower Monte Carlo it would be necessary to take account of the three degree tilt of the matrix in both horizontal and vertical coordinates. it would also require a precise knowledge of the alignment of the scaled scintillator with both the matrix and the drift chambers, However, such knowledge is not available, and therefore the practical solution is to accept some imprecision and assume the lateral spread is dominated by the beam spread.

Using an empirical parameterisation of the longitudinal shower profile given in ref. [35]
[36] the dose is found to reach a maximum of 6.7×10^{-6} rads per 120 GeV electron incident on the 20×20 mm^2 trigger counter, at a depth of 8.2 X_0 in the crystal.

$$Dose(rads) = Counts \times 6.7 \times 10^{-6} \qquad (3.4)$$

This expression depends on two assumptions:

i. The dose leaking out from the crystal in showers generated by electrons firing the scaler is equal to the dose leaking into the crystal from showers not firing it. This would obviously be the case if the beam was infinitely wide.

ii. The scaled trigger counter is perfectly aligned with the crystal.

The incorrectness of these assumptions contributes an error of perhaps ±10% [37].

Figure 3.16 shows the distribution of the impact point with respect to the crystal centre, as measured by the beam chambers, for one data run of 100k events during the irradiation period. It can be seen that neither the electron beam or the scintillation trigger were perfectly aligned with respect to the crystal centre. However, the beam width is large and therefore the relationship between the accumulated number of events and dose is a good approximation.

It was difficult to calculate the exact dose received by the eight crystals under investigation and some further assumptions had to be made. First the dose for the central crystal (1283) was calculated. The cumulative S2 counts per burst were stored during data taking. The cumulative counts per run were calculated and then converted into dose at shower maximum using Equation 3.4.

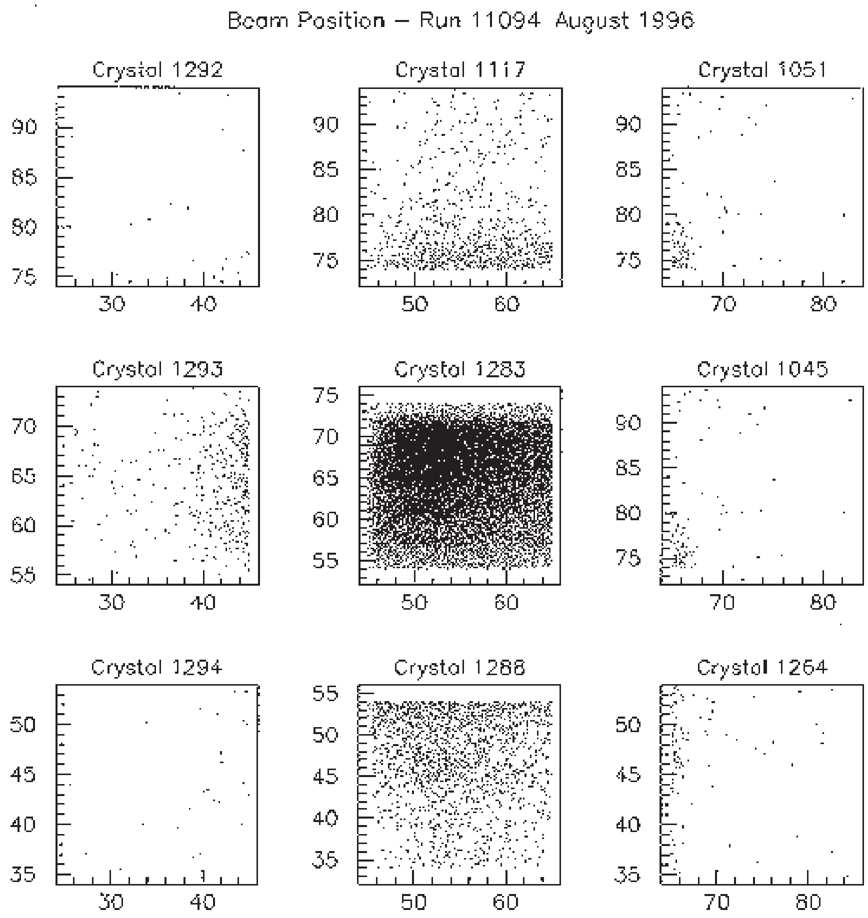

Figure 3.16: Impact point with respect to the crystal centre. The beam is centred on crystal 1283.

Stability studies that were performed in May 1996 showed that the beam shape in H4 was Gaussian with a horizontal and vertical σ of ~15mm. Thus the assumption that the beam width is bigger than a shower is valid. Using the known beam shape allowed us to estimate the dose received in the surrounding crystals as a function of the dose in crystal 1283 during the August stability studies. Table 3.5 shows the estimations of dose that were made for the eight crystals surrounding 1283 as a fraction of the dose received in the central crystal.

However this is dependent on alignment as well as assumed beam σ, and the hit distribution for triggered events shows that the beam was not well centred.

The dose rates are averaged over the SPS cycle. The instantaneous dose rate during the spill is 14.4sec/2.4sec = 6 times higher.

↓	½	↓
½	**1**	½
↓	½	↓

Table 3.5: Dose received as a fraction of dose in Crystal 1283.

3.4.5 Effects of Irradiation

For each of the crystals that were studied, the accumulated dose and the % decrease in the beam signal are shown in Table.3.6. The results for crystal 1283 are shown for information.

Crystal	**Approximate Dose (rads)**	**% Decrease**
1283	*640*	*8*
1292	210	17
1117	320	10
1051	210	5
1293	320	28
1045	320	10
1294	210	8
1288	320	10
1264	210	0

Table 3.6: Results of August Stability Study

Fig. 3.17 to 3.23 show the changes in signal as a function of dose for seven of the crystals. It was estimated that crystal 1264 received a dose of 210rads. However, this may not have been the case. Figure 3.24 shows a variation of ±5% in the beam signal during the period of the stability study. There were very few particles incident upon this crystal which partly explains the variations shown in this plot. The other explanation is that the dose was not as much as 210rads in this crystal. The dose approximations assumed that the beam was always well centred. However, investigation has shown that during the August stability study the beam was not centred very well. This is seen in Figure 3.16. The beam was actually slightly more concentrated in the upper and left hand side of the matrix (as viewed from the rear) so the dose received by crystal 1264 was probably somewhat less than the estimation of 210rads.

The decrease in mean beam signal for the central crystal, 1283, was 6% after a dose of 200rads and 8% after a dose of 640rads had been received [29].

Crystal	**Approximate Dose (rads)**	**% Decrease**
1283	*200*	*6*
1292	200	15
1117	200	8
1051	200	5
1293	200	24
1045	200	8
1294	200	8
1288	200	6
1264	200	0

Table 3.7: Decrease in mean beam signal for a dose of 200rads.

To enable a more direct comparison between the eight crystals that were studied Table 3.7 shows the decrease on mean beam signal in each crystal for a received dose of 200rads, once again the results for crystal 1283 have been included. However it was difficult to make meaningful comparisons between the eight crystals. Although all were manufactured in Russia, they mostly came from different production runs over a fourteen month period. Two of the crystals, 1045 and 1051, came from the same production run and were doped with Niobium at a concentration of 30ppm. They showed relatively small decreases in the beam signal, 8% and 5% respectively, but it was not clear if this was because of the doping or due to differences in crystal manufacture. It was also not possible to make any useful comparisons with the central crystal, 1283, which was produced at the SIC facility in China.

The plots also demonstrate that the LED light signal follows the beam signal well. The use of an LED is an effective way to follow the effects of radiation in the crystals. This is studied in more depth in [29].

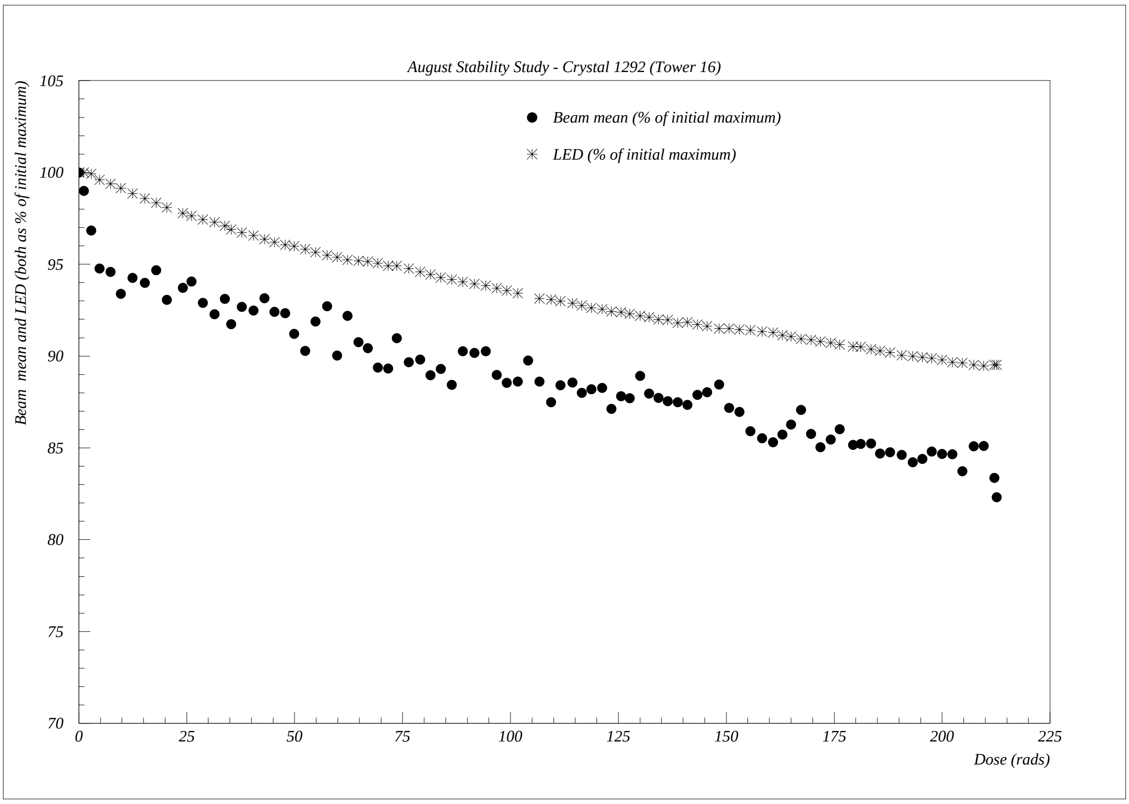

Figure 3.17: Crystal 1292

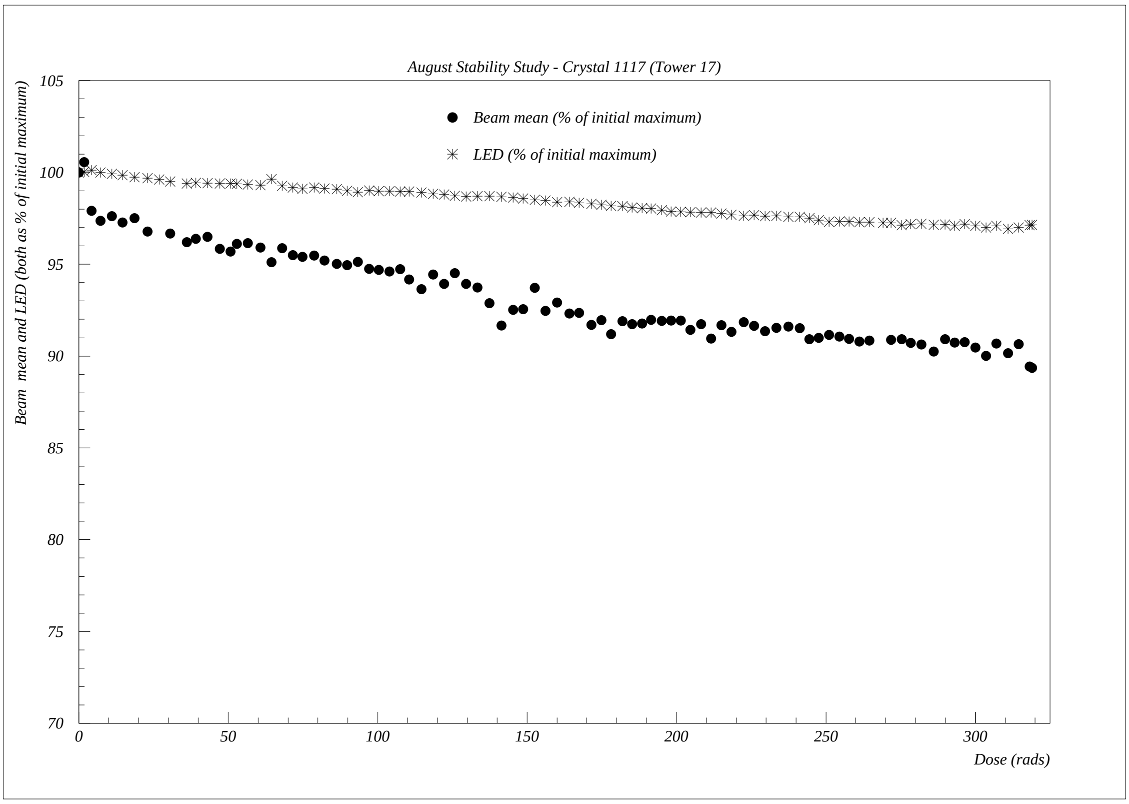

Figure 3.18: Crystal 1117

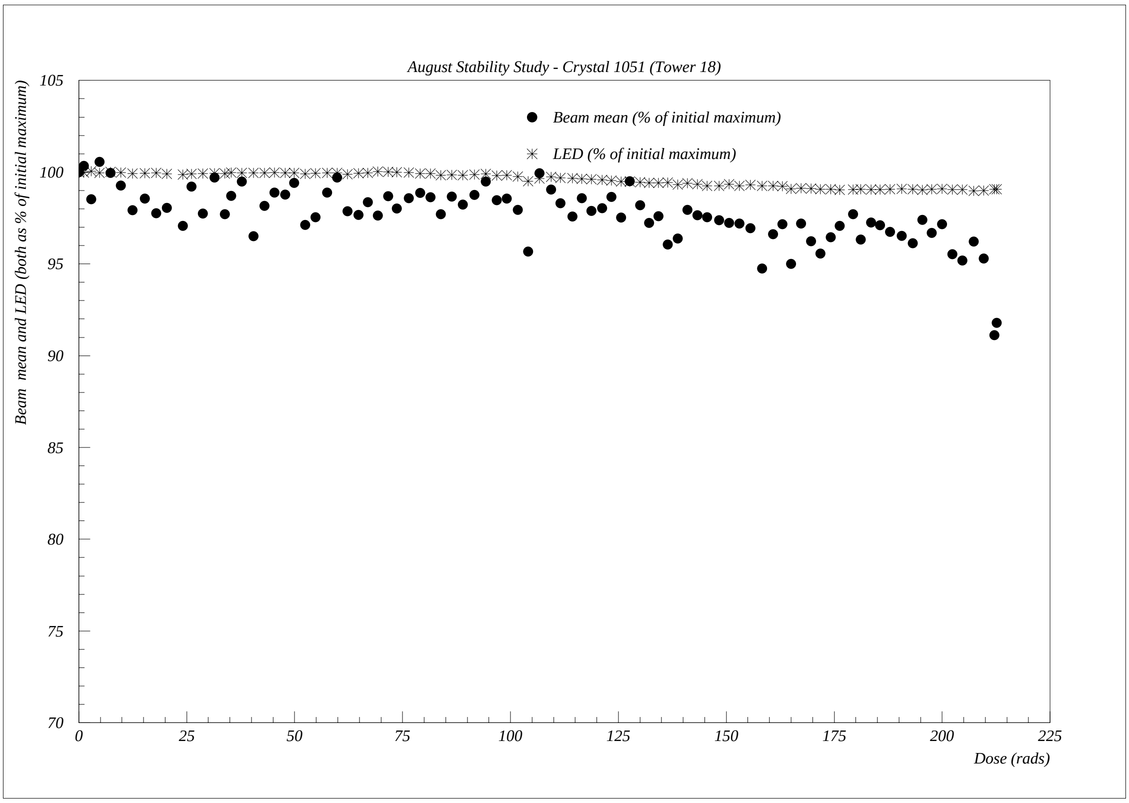

Figure 3.19: Crystal 1051

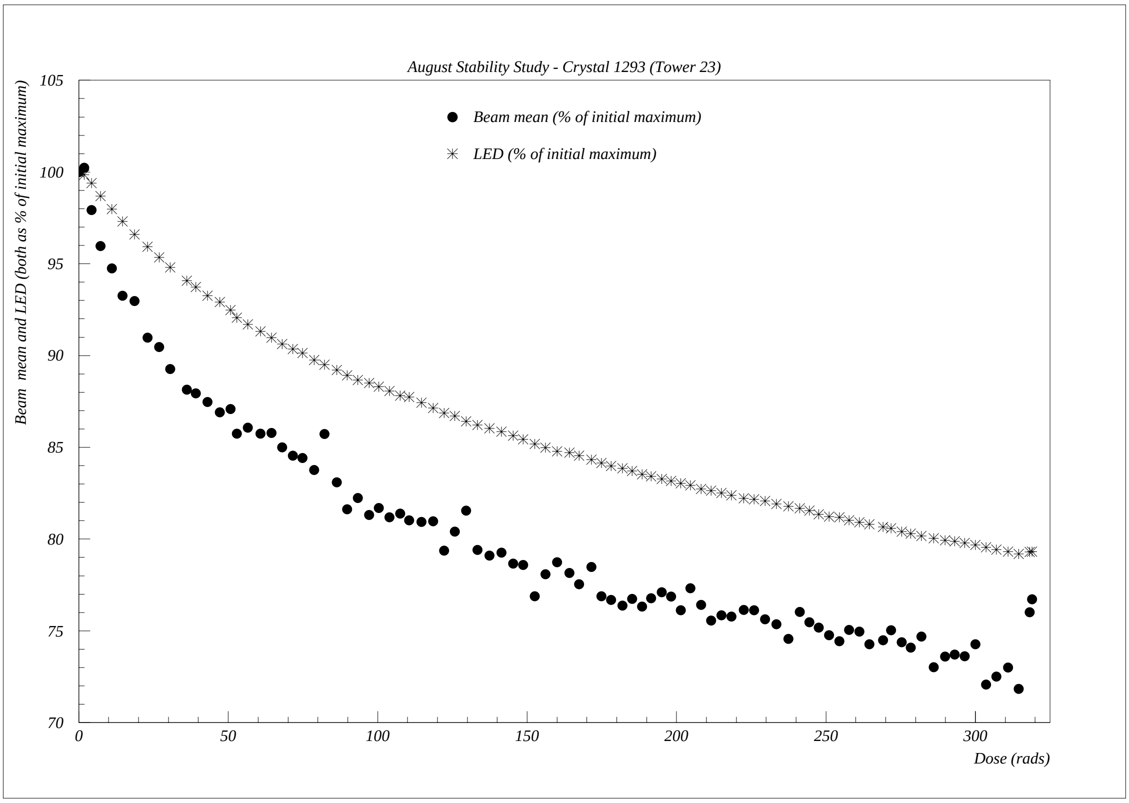

Figure 3.20: Crystal 1293

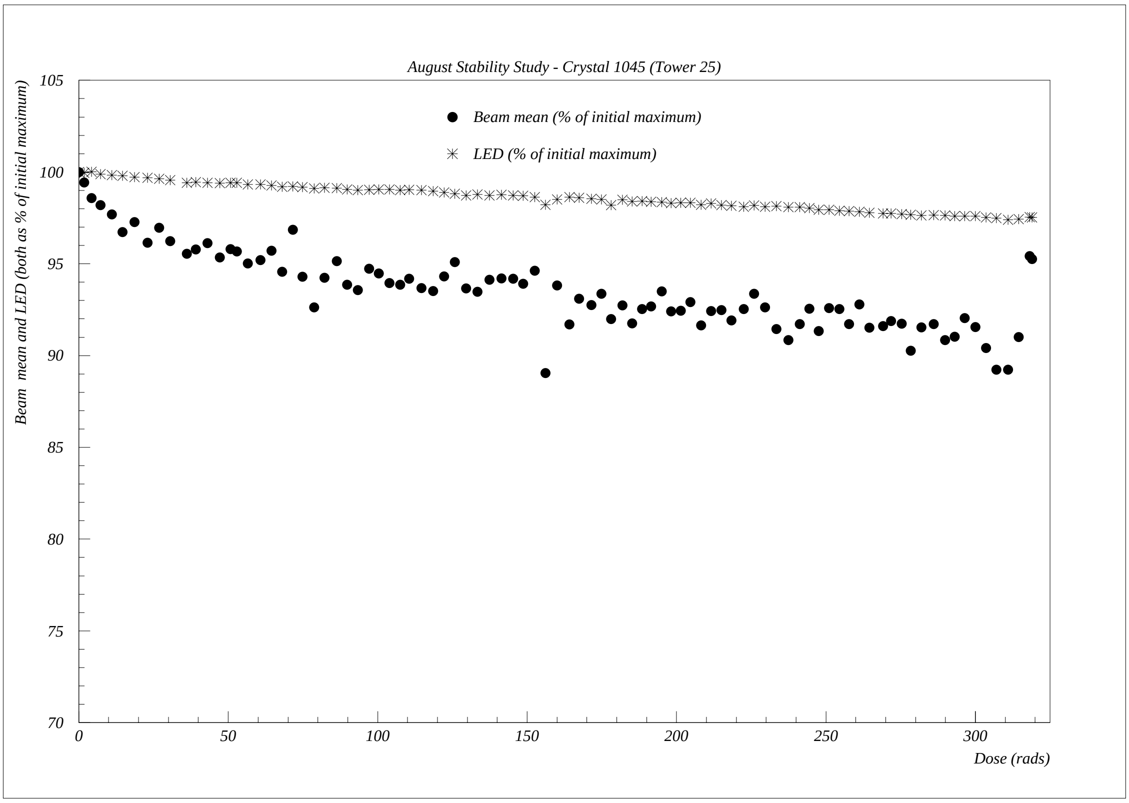

Figure 3.21: Crystal 1045

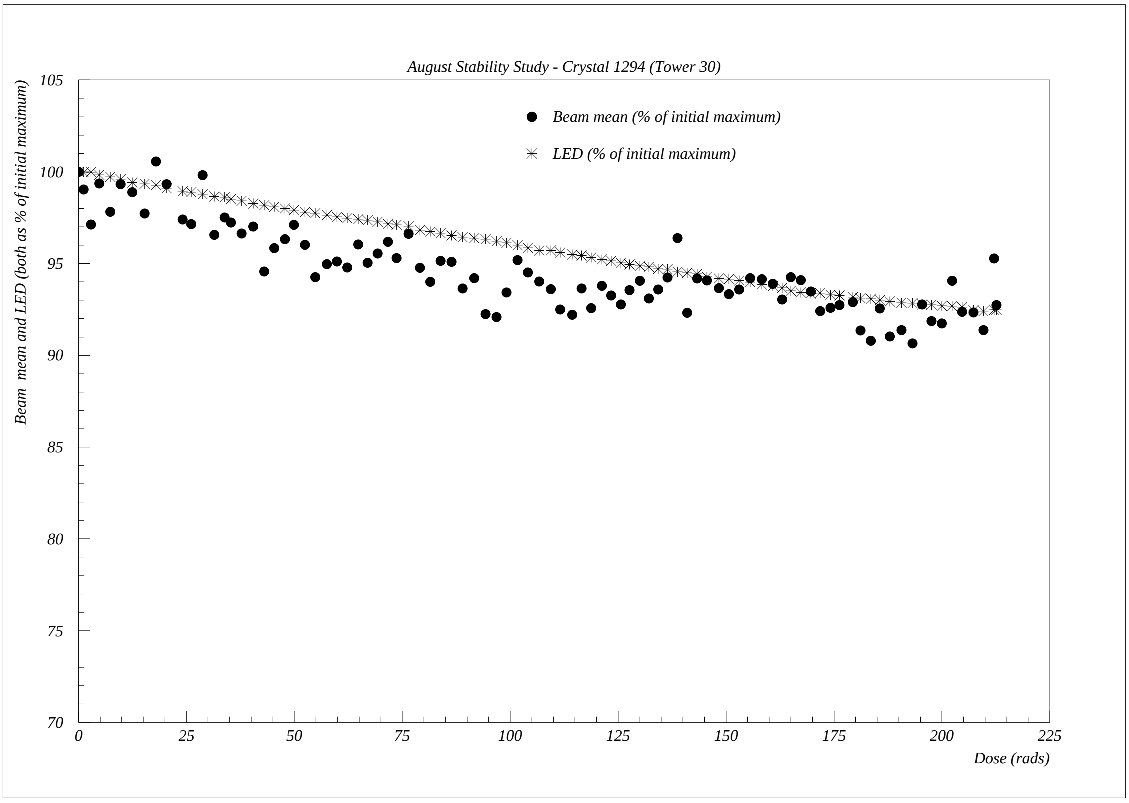

Figure 3.22: Crystal 1294

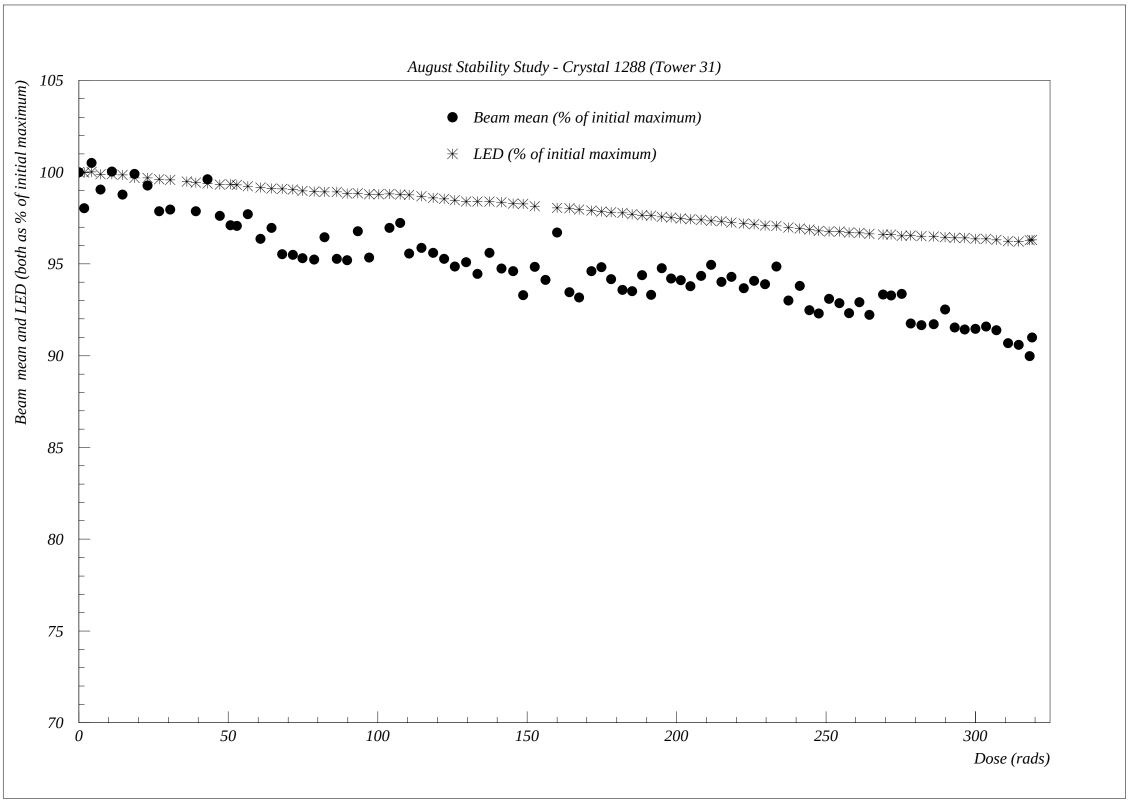

Figure 3.23: Crystal 1288

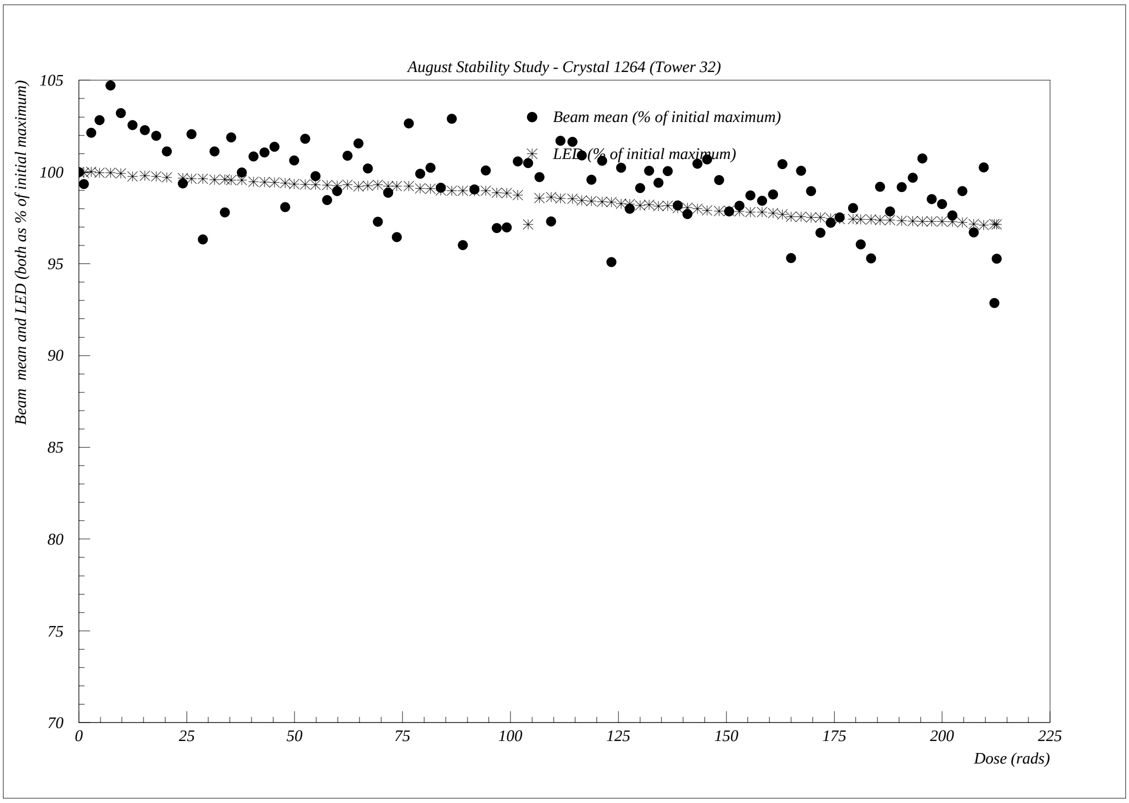

Figure 3.24: Crystal 1264.

This analysis could have been improved in several ways. To have a true picture of the results of radiation ‘spilling over’ from the central crystal it would have been more useful if the surrounding crystals all came from the same production run. If the crystals were identical and the beam was centred correctly a truer picture of the spread of radiation damage would have been gained. It would also have been interesting to compare a central crystal from, for example, SIC, with eight surrounding crystals from the same production facility. However, this method would mean that information would only be gained about one production run at a time and it would take a long time to study nine crystals from each production run. Even with these disadvantages the analysis confirmed the important result that these crystals were not sufficiently radiation hard and would not have been suitable for use in the final CMS ECAL. It shows that the production mechanism was not good enough or sufficiently well understood.

However, these beam tests were part of a programme of preliminary R&D on the lead tungstate crystals. This R&D programme has been a combined effort between CMS and the crystal producers. The R&D has continued and many hundreds of crystals have been tested. Lead tungstate is intrinsically radiation hard, although the early non-optimised crystals suffered from radiation damage. The R&D carried out has led to a better understanding of the damage mechanism and crystals are now being produced which are more resistant to radiation. It has been found that the intrinsic energy resolution of the crystals is undamaged which is consistent with the scintillation mechanism being undamaged [13].

3.5 Conclusions

The testing of prototypes of the CMS electromagnetic calorimeter has been described. An analysis of data taken in beam tests of lead tungstate ($PbWO_4$) crystal matrices, read out by silicon avalanche photodiodes (APDs), performed in the H4 Beam of the SPS North Area at CERN has been presented. The electromagnetic energy resolution of the prototype calorimeter has been studied in detail and the contributions to the terms of the energy resolution parameterisation have been investigated. The stochastic terms obtained have been understood in terms of the photostatistics of the number of primary photoelectrons released in the APD. The energy resolution from a typical crystal was:

$$\frac{\sigma}{E} = \frac{4.5\%}{\sqrt{E}} \oplus 0.31\%$$

where the energy equivalent of noise was 135MeV. The tests have shown that excellent energy resolution can be obtained with lead tungstate crystals when the longitudinal uniformity of the struck crystal is adequate. Further studies will explore techniques for achieving longitudinal uniformity.

The response of eight lead tungstate crystals to irradiation has also been studied. These crystals were in a matrix surrounding a central crystal that received a dose of 630rads. It was estimated that the four horizontally and vertically adjacent crystals received 50% of that dose and the four diagonally adjacent crystals received about

33% of the central crystal dose. The effects of this reduced dose have been examined. The main conclusion was that none of the crystals were sufficiently resistant to the effects of radiation and more R&D was necessary.

4 Direct Photons in CMS.

4.1 Introduction

The CMS detector is being built to study the interactions of quarks and gluons at very high energies up to ~1TeV. In order to interpret the measurements we need to understand the quark and gluon distributions in the incident proton beams. The remainder of this thesis studies the prospects for measuring these distributions at LHC using direct photon production.

QCD is the quantum field theory that describes the interactions of quarks and gluons. In experiments we have hadrons in the initial and final states and the constituent quarks and gluons, or more generally, *partons*, are not directly observed. To compare experimental results with theory we need some phenomenological input in addition to QCD for hard quark-gluon interactions. It is necessary to describe how the initial quarks and gluons 'emerge' from hadrons and how the quarks and gluons in the final state form hadrons. QCD is not able to explain everything about these processes but it can explain how they vary with energy scale, thus allowing comparisons between different experiments.

Some of the same phenomenological input is required to describe the electro-weak interactions of quarks. An example of this is direct production of photons in hadron collisions. This is a useful process to study because the photon emerges from the hard interaction free of any strong interaction complications. This results in a clean probe of the behaviour of initial state partons. A detailed understanding of the initial state is essential for the analysis of any new physics discovered at LHC.

4.2 Perturbative QCD Interactions

Scattering amplitudes and cross-sections in QCD and QED are calculated using Feynman diagrams. The contribution of each diagram to the amplitude is found using

Feynman rules. Each vertex in the diagram gives rise to a factor of $\sqrt{\alpha}$ in the contribution to the amplitude, where α is the coupling constant for the interaction. This means that the full cross section is a power series in the coupling constant. If the coupling constant is sufficiently small only a small number of leading terms need to be considered. However, if α is too large then the series will not converge. A series written in this way and calculated using Feynman diagrams is called a perturbation series.

Infinities come out in every term of the perturbation series beyond the lowest which leads to unphysical results. This is because of loops in the Feynman diagrams. Every possiblity has to be considered and there is an infinity of possibilities. To resolve this problem a mathematical method known as *renormalisation* is used. This neatly removes the infinities but at the cost of introducing an arbitrary momentum scale μ_R that is called the renormalisation scale. It is important to remember that μ_R is an artificial, non-physical parameter which only appears in the result of the calculation because we cannot complete the calculation to all orders. In principle the result of a calculation should be independent of μ, however this is only true if we calculate to all orders. Calculations of finite order therefore give results that are dependent on μ. The renormalisation scale is chosen to be some energy (momentum) representative of the scale of the interaction. We expect that the dependence of the result on μ_R will be small if we have carried the calculation to high enough order. However it is difficult to know what 'high enough' is and it is also very difficult to do higher order calculations.

Most higher order effects can be accounted for if the coupling constant is written not as a constant but rather as a function of scale μ. This is seen in QED where α is 1/137 at small μ but increases to 1/128 at the mass of the Z boson. In QCD, by contrast, the coupling constant, α_S decreases with increasing scale. The variation of the coupling α with μ is described by the equation:

$$\mu^2 \frac{\partial \alpha}{\partial \mu^2} = -b\alpha^2 \qquad (4.1)$$

to lowest order. This is the renormalisation group equation which comes from requiring that the results of the calculation are independent of μ. In QED the factor *b* is negative, leading to an increase in α with increasing scale. In QCD we have

$$b = \frac{1}{12\pi}\left(11n_c - 2n_f\right) \qquad (4.2)$$

the number of (active) quark flavours. The first term in this expression comes from the gluon self-coupling terms and makes the whole expression positive since $n_f \leq 6$.

This can be visualised in a space time picture where increasing the energy scale μ corresponds to shorter distance interactions. The effect of electric charge is seen to increase at short distances while strong charges get weak.

4.3 QCD description of hadronic interactions.

As stated in the introduction to this chapter we need to include other elements in addition to the perturbative hard scattering to get a description of experimental measurements of hadrons. Equation 4.3 gives the full description of a process in QCD, which is illustrated in Figure 4.1.

$$\begin{aligned}\sigma(A+B\to C+X) = \sum_{abcX}\int dx_a\, dx_b\, dz_c\, F_{a/A}(x_a,\mu_F)F_{b/B}(x_b,\mu_F)D_{c/C}(z_c) \\ \times\ \hat{\sigma}_{ab\to cX}(x_a,x_b,\mu_R,\mu_F)\end{aligned} \qquad (4.3)$$

The term $\hat{\sigma}$ describes the hard interaction which can be calculated by the methods described in the previous section. The parton distribution function $F_{a/A}$ describes the probability of finding a parton *a* with momentum fraction x_a inside the beam particle *A*, similarly for $F_{b/B}$. Precisely, $F(x)\ dx$ represents the number of partons with momentum fraction between x and $x + dx$. *D* is the fragmentation function which describes the probability of getting *C* from *c* with some fraction z_c of *c*'s momentum.

Writing the process in this way means that we are arbitrarily dividing all the complex interactions into a hard scattering part which can be calculated and soft parts which cannot be calculated. The soft processes include those in the initial state, where partons are ‘selected’ from the incoming particles to take part in the interaction, and final state processes which produce the outgoing hadrons. The separation is done by introducing the factorisation scale μ_F. Processes which occur at energy scales larger than μ_F are considered to be part of the hard interaction. Mathematically, this scale specifies the momentum scale of the renormalisation of the operators that appear in the definition. Physically, μ_F is the momentum scale at which the hard interaction probes the partons.

An important result from QCD [38] is that this separation, known as factorisation, can be done in a consistent way. The parton distribution functions (PDFs) $F_{a/A}$ are universal functions that depend only on a and A and not at all on the nature of the hard process. Similar considerations apply in the case of the fragmentation functions. Moving to a space time picture, the hard scattering represents short distance interactions between partons. In contrast, the parton distribution functions and the fragmentation functions describe processes that are happening a long way from the hard scattering.

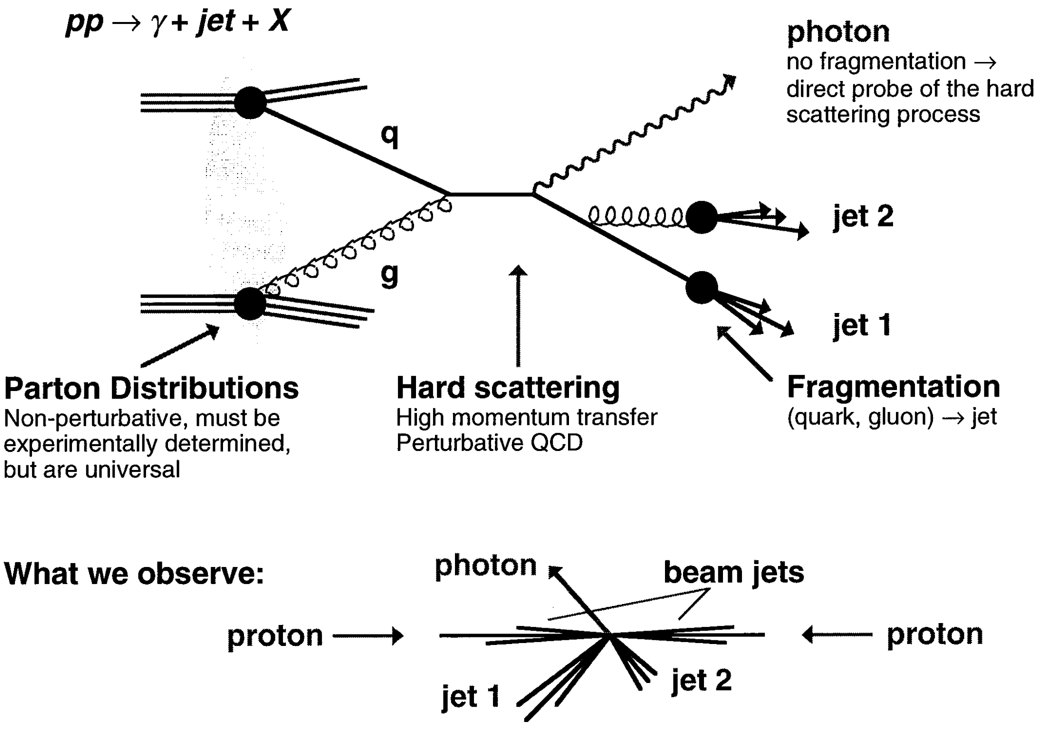

Figure 4.1: Diagram illustrating different aspects of a QCD interaction (courtesy W. J. Womersley).

In the specific case of photon production, as shown in Figure 4.1, the final state photon is free of the complication of fragmentation ($D_C / \gamma = 1$). The photon is seen in the final state exactly as it was produced, directly from the parton level interaction. This enables us to study more directly the initial state processes and the parton distribution functions.

4.3.1 Parton Distribution Functions

Parton distribution functions describe the parton substructure of a high momentum proton or other hadron. The function $F_{a/A}(x, \mu)$ gives the distribution of partons of type *a* in a hadron of type *A.* Here, *a* could be any flavour of quark, any flavour of antiquark or a gluon. The label *A* can designate a proton, anti-proton, neutron, pion, or any other hadron. In this thesis only the case *A* = proton is considered.

The parton distribution functions depend on the factorisation scale μ_F. The variation of PDFs with μ is described by QCD. A parton that is seen at a low scale can be resolved at higher scale into two or more partons, i.e. a quark can emit gluons or gluons can fluctuate into $q\bar{q}$ pairs. In practice when parton distribution functions are used to make QCD predictions for a physical process, μ_F is set to be of the same approximate size as the momenta involved in the process.

The evolution of the quark and gluon distributions with μ is given by the DGLAP equations:

$$\begin{aligned} \frac{\partial F_{q/A}(x,\mu^2)}{\partial \ln \mu^2} &= \frac{\alpha_s(\mu^2)}{2\pi}\left[P_{qq} \otimes F_{q/A} + P_{qg} \otimes F_{g/A}\right] \\ \frac{\partial F_{g/A}(x,\mu^2)}{\partial \ln \mu^2} &= \frac{\alpha_s(\mu^2)}{2\pi}\left[P_{gq} \otimes F_{q/A} + P_{gg} \otimes F_{g/A}\right] \end{aligned} \tag{4.4}$$

where $\otimes$ represents the convolution operation eg.

$$P_{qq} \otimes F_{q/A} \equiv \int_x^1 \frac{dz}{z} P_{qq}\left(\frac{x}{z}\right) F_{q/a}\left(z,\mu^2\right) \tag{4.5}$$

and the splitting functions P_{qq} are calculable in perturbative QCD. $P_{qq}(x/z)$, for example, represents the probability for a quark of momentum fraction *z* to fluctuate into a quark of momentum fraction *x* and a gluon of momentum fraction $z - x$.

The formalism is quite straightforward at leading order (LO), with simple algebraic expressions for the splitting functions, but becomes much more complicated in higher orders. In many cases where QCD is confronted with experimental data, calculations of the hard scattering are available beyond leading order in perturbation theory. In these cases the behaviour of the structure functions must also be described beyond leading order.

Sets of parton distribution functions, one function for each kind of parton in a proton, are produced to fit experimental data. Figure 4.2 shows the gluon distribution and the up-quark distribution in a proton, according to the CTEQ4M [39] parton distribution set. The figure [40] shows $x^2 F_{a/A}(x,\mu)$ for $a = g$ and a = u, A = p. Note that the area under the curve is

$$\int_0^1 dx\, x\, F_{a/A}(x,\mu) = \int_{-\infty}^0 d(\ln x)\, x^2 F_{a/A}(x,\mu) \qquad (4.6)$$

and this is the momentum fraction carried by partons of type a.

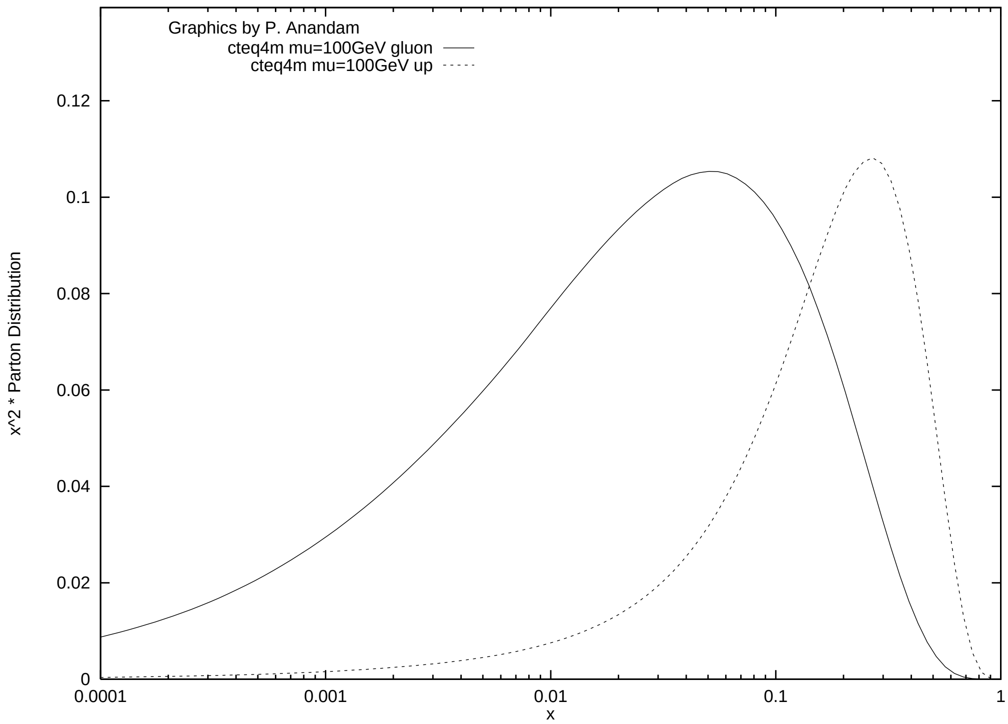

Figure 4.2: Gluon and up quark distributions in the proton according to the CTEQ4M parton distribution set.

4.3.2 Global fitting of parton distributions.

There are three main groups of people currently doing global fitting of parton distributions:

- Martin, Roberts and Stirling (MRS) [41]
- Gluck, Reya, and Vogt (GRV) [42]
- Brock, Collins, et al (CTEQ) [39]

The purpose of the fitting is to adjust the parton distribution functions to make theory and experiment agree for a wide range of processes and scales. For example, recent CTEQ fits have used the following processes: [43]

$$
\begin{aligned}
&e + p \to X \\
&\mu + p \to X \\
&\nu + Fe \to X \\
&p + p \to \mu + \overline{\mu} + X \\
&p + Cu \to \mu + \overline{\mu} + X \\
&p + \overline{p} \to W \to l + \bar{l} + X \\
&p + \overline{p} \to \gamma + X \\
&\mu + {}^2H \to X \\
&\overline{\nu} + Fe \to X \\
&p + {}^2H \to \mu + \overline{\mu} + X
\end{aligned}
$$

The main features of a programme of global fitting are as follows. First of all a starting scale is chosen, for example μ_0 = 2GeV. Then $F_{a/A}(x,\mu_0)$ is written in terms of several parameters for $a = g, u, d, s$, and their antiparticles. Generally the heavy quark distributions are generated from evolution, not fit to data. At small scale there are no heavy quarks, however using equations such as 4.4 the distributions may be evolved until, via gluon splitting, heavy quarks are found in the distributions.

An example is

$$F(x,\mu_0) = Ax^B(1-x)^C(1+Ex^D) \qquad (4.7)$$

The parton distribution functions obey certain flavour and momentum sum rules, such as

$$\begin{gathered}\int_0^1 dx\left[F_{u/p}(x,\mu) - F_{\bar{u}/p}(x,\mu)\right] = 2 \\ \sum_a \int_0^1 dx\, x\, F_{a/p}(x,\mu) = 1\end{gathered} \qquad (4.8)$$

These sum rules follow from the operator definitions[43]. The parameterisations are chosen so that these flavour and momentum sum rules are obeyed exactly.

The next thing is to pick a trial set of parameters. This determines $F(x,\mu_0)$, from which $F(x,\mu)$ can be calculated for all μ by evolution. Then, given the $F(x,\mu)$, theory curves are generated for each type of experiment used. Hard scattering matrix elements are also needed for all the processes. These must be calculated with a consistent treatment of μ_F etc. Both leading order and next to leading order fits are performed but this is not easy beyond leading order. Finally the results are compared to the data. This sequence is iterated, adjusting the parameters to get a good fit. There are more than a thousand data sets and only about 25 free parameters in the fit, so the fact that this procedure works at all provides support for QCD as the correct theory of the strong interactions.

4.3.3 Parton Distribution Functions used in this analysis.

Some of the parton distribution functions are implemented in a convenient form in PDFLIB [44] which makes them suitable for use in Monte Carlo simulations. The PDFs used in this thesis are described below.

4.3.3.1 CTEQ

The starting scale of the CTEQ parameterisations is $Q_0^2 = 2.46\ \text{GeV}^2$. It uses data for the fits from a large number of experiments, both from DIS experiments (HERA, NMC, E665), and from *p-p* experiments (eg. inclusive jet data from the TEVATRON). The PDFs extracted from the fit depend quite strongly on the starting scale. The latest set of proton structure functions available from CTEQ are CTEQ4M [39]. The baseline PDF for this thesis is the CTEQ4M parameterisation.

4.3.3.2 GRV

In contrast to CTEQ, GRV begin at a very low starting scale, $Q_0^2 = 0.34\ GeV^2$. The motivation behind this is that at such a low starting scale, the nucleon consists only of the constituent valence quarks as they are fully constrained by the charge and momentum sum rules. This is intended to remove the dependence of the PDFs upon the starting scale.

4.3.3.3 MRS

The MRS fit includes data from DIS experiments and they have also studied other information for the gluon, including the constraints coming from fixed-target and collider direct photon production data.

Set	**Description**	$\alpha_S(m_Z)$	$Q_0^2\ (GeV)^2$
CTEQ4M	$\overline{MS}$ scheme	0.116	2.56
CTEQ4L	Leading order	0.132	2.56
GRV94HO	$\overline{MS}$ scheme	0.115	0.34
GRV94LO	Leading order	0.128	0.34
MRS G	$\overline{MS}$ scheme	0.114	5

Table 4.1: The parton distribution functions used in this analysis.

4.4 Direct Photons

The study of direct photon production from hadrons provides experimental physicists with a unique and very useful tool with which to test QCD. The term direct photon is taken to mean a photon that originates from an interaction related to the hard scatter and not from the production of a hadron that subsequently decays electromagnetically. Since the direct photon originates in the hard-scattering sub-process one has a more direct probe of the interaction. Furthermore, the photon couples to the electric charge, while quarks and gluons interact via the colour charges. Thus direct photon production yields information that is complementary to that obtained from jet production. The characteristics of the final state particles that come from a direct photon event and the ease and precision with which photons can be identified and measured provide a practical advantage in studying this process.

4.4.1 Direct Photon Diagrams

Figure 4.3 shows leading order diagrams for direct photon production.

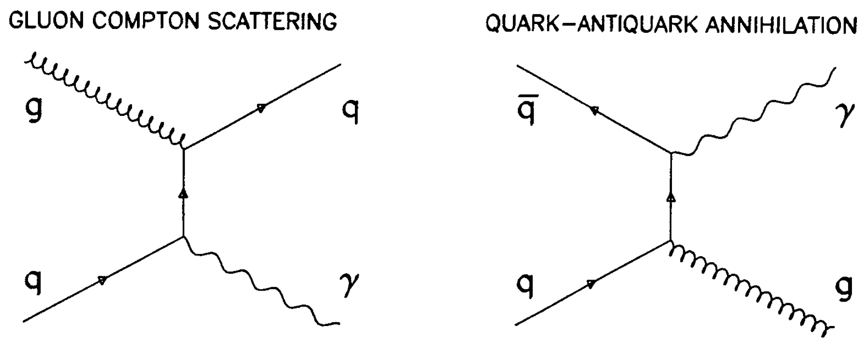

Figure 4.3: Leading order diagrams for direct photon production.

One way in which photons can be produced is in quark-antiquark annihilation, in which the direct photon is produced along with an outgoing gluon. Another important process is a form of QCD Compton scattering, in which a gluon scatters from a quark producing a photon in the final state along with the scattered quark. Because of the abundance of low *x* gluons in the proton, QCD Compton scattering is the dominant form of direct photon production for E^{γ}_{T} below approximately 100 GeV. Above this energy the, typically, larger momentum quarks are necessary to produce such an energetic photon and the annihilation diagram becomes more prominent. Because of the Compton dominance it is expected that a measurement of direct photon production will have sensitivity to the gluon content of the proton.

Some examples of higher order photon production diagrams are shown in Figure 4.4. These usually involve additional gluon radiations and result in characteristic event signatures of a photon plus two or more jets. Current direct photon QCD calculations include only up to the two jet level, order $\alpha\alpha_S^2$. These are known as next-to-leading order (NLO) calculations. The experimental measurement includes all orders and is therefore called *inclusive*. However, if the terms beyond NLO are small, the NLO prediction should be a good approximation to the inclusive cross section.

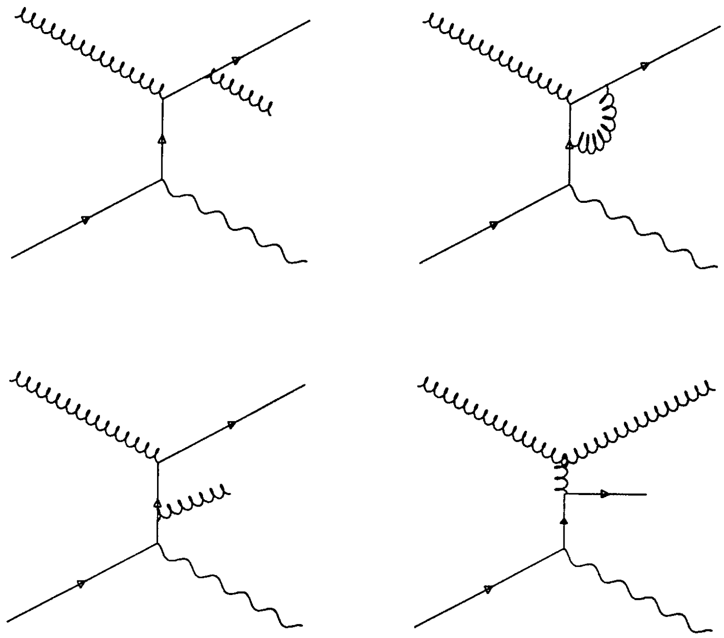

Figure 4.4: Examples of higher order direct photon diagrams.

4.4.2 Bremsstrahlung Component and Isolation

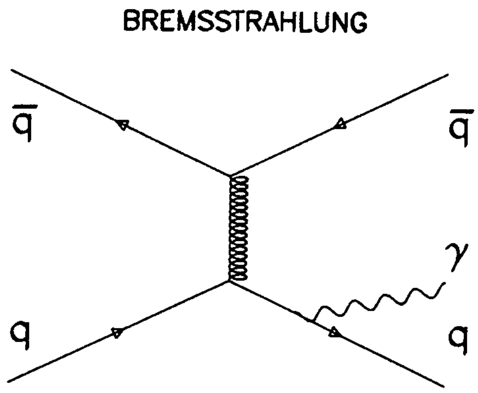

Figure 4.5: Photon production through Bremsstrahlung.

As shown in Figure 4.5 there is another source of single photons: *bremsstrahlung* from an outgoing quark in a dijet event. In this case the photon is not produced directly from the interaction vertex and is therefore not really a 'direct' photon. However the existence of this production method affects the way in which direct photons are measured and modelled theoretically.

In order to minimise the effect of the bremsstrahlung case an isolation criterion is imposed upon the photon. Usually a cone around the photon is examined and required to have less than a certain amount of energy. A photon produced through bremsstrahlung tends to be very collinear with the quark it radiates from. The requirement that the photon be isolated removes all but the very largest angle radiation.

4.5 Direct Photon Kinematics

As outlined in the previous section, the main processes contributing to direct photon production are the two-body reactions $gq \rightarrow q\gamma$ and $q\bar{q} \rightarrow g\gamma$. In this case, assuming no transverse momentum of the initial partons, we need to measure three kinematic variables of the final state photon and hadron jet in order to determine the initial parton energies and hence the gluon fractional momentum x_g in $gq \rightarrow q\gamma$ events. These variables may be chosen to be, for example, the photon p_T, and the photon and jet angles or pseudorapidity η. The main differences between the different parameterisations of the parton distribution functions are at low *x* so this is an important area for study. Experiments generally need to place a cut on the minimum photon p_T to isolate the direct photon signal from the jet background. This restricts the region of x_g to which the experiment is sensitive. The x_g range also depends on the angular coverage of the measurements. An experiment with an acceptance to large η, or small angles with respect to beams, gives a better reach to low x_g.

4.5.1 Pseudorapidity dependence.

Theoretical investigations have shown [45] that the cross section of direct photons has a pseudorapidity dependence which is sensitive to the parameterisation of the gluon distribution functions. Results from different experiments can be compared as a function of the variable

$$x_T = \frac{2p_T}{\sqrt{s}} \qquad (4.9)$$

This is related to the fractional momenta x_g, x_q of the initial partons. The energy available in the parton subprocess is $\sqrt{\hat{s}}$ where $\hat{s} = x_g x_q s$. If the initial parton energies are nearly equal, the photon and jet are produced back-to-back in the laboratory. Then at large angles to the beam, in the central region $\eta \approx 0$, we have that the photon p_T is about the same as the initial parton energy, or x_g is close to x_T. At smaller angles, for the same x_T, the parton CM energy $\hat{s}$ and hence x_g are larger. Now consider the case of a large imbalance between initial parton energies, such that $x_g << x_q$. In this case, both the photon and jet will tend to be produced at small angles, either both forward η > 0 or both backward. The cut on p_T determines the minimum $\hat{s}$ value that can be measured, while a large forward acceptance means that events can have a greater degree of imbalance between the initial parton energies, and so a smaller x_g for a given $\hat{s}$. Detailed calculation of the two-body kinematics gives the minimum x_g for cuts on p_T, η as

$$x_{g_{\min}} = \frac{x_T e^{-\eta}}{2 - x_T e^{\eta}} \qquad (4.10)$$

Since most earlier experimental direct photon results, with the exception of D0 and CDF have focused on the central pseudorapidity region, the forward direct photon capability of the CMS detector allows a relatively new region for investigating the pseudorapidity dependence where gluon distributions within hadrons can be constrained. The pseudorapidity dependence is more crucial for the case of gluons since their momentum fraction peaks at lower x values [46]. As one goes to lower p_T or higher pseudorapidity η, there is an increased possibility to study gluons near the x range around 10^{-4} - 10^{-3} where they are dominant in the hadronic structures [47].

Table 4.2 gives the value of $x_{g_{\min}}$ for different p_T cuts and η values at LHC. It can be seen that an acceptance to |η| = 2.5 considerably enhances the reach of low x_g values.

p_T / GeV	**x_T**	**x_g min, η = 0.5**	**x_g min, η = 1.5**	**x_g min, η = 2.5**
20	0.0029	9.0×10^{-4}	3.0×10^{-4}	1.0×10^{-4}
40	0.0057	1.7×10^{-3}	6.0×10^{-4}	2.0×10^{-4}
60	0.0086	2.6×10^{-3}	1.0×10^{-3}	4.0×10^{-4}
80	0.0114	3.5×10^{-3}	1.3×10^{-3}	5.0×10^{-4}
100	0.0143	4.4×10^{-3}	2.7×10^{-3}	6.0×10^{-4}

Table 4.2: The variation in x_T with changes in p_T and η at LHC.

4.5.2 Regions accessible to various experiments.

In previous studies of the gluon distribution the high x gluons have been measured in fixed target deep inelastic scattering , while low x gluons have been measured at HERA using the DGLAP variation of the structure functions with scale. However, the LHC will open up a new kinematic region which will give the opportunity to study gluons of low x but much higher Q^2 than at HERA .The studies at the Tevatron have been better than anything that was done before but at CMS we will be able to go lower x and higher Q^2 than either D0 or CDF. This new kinematic region is illustrated in Figure 4.6.

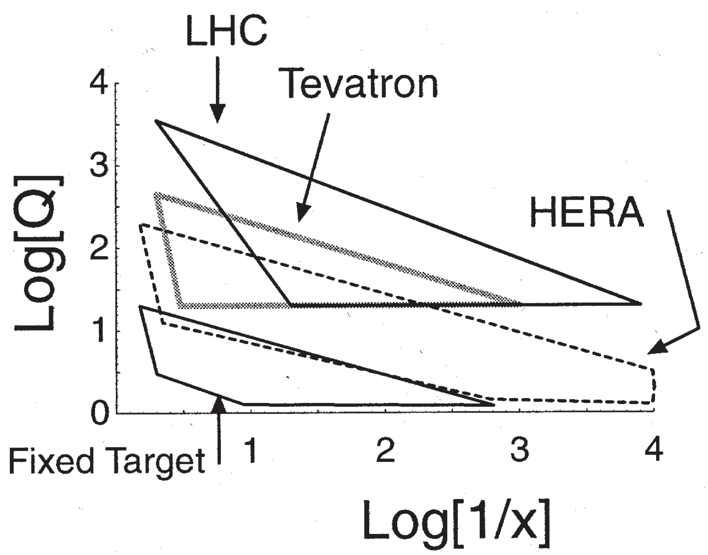

Figure 4.6: Kinematic reach of present and planned facilities. Note that the full (x,Q^2) region is clipped by the plot [48].

4.6 Other Studies of Direct Photon Production

Direct photon production has been studied at several fixed target and collider experiments. The parameters of some of these experiments are shown in Table 4.3 [49],[50],[51],[52].

Experiment		**√s Gev**	$\boldsymbol{x_T}$	**η**	**pb^{-1}**
D0	$p\bar{p}$	1800	0.013 – 0.13	± 3.0	?
CDF	$p\bar{p}$	1800	0.013 – 0.13	± 1.1	?
E706	*Pbe*	31	0.26 – 0.52	±0.7	0.75
E706	π^- *Be*	31	0.26 – 0.52	±0.7	0.50
UA6	*pp*	24.3	0.34 – 0.63	-0.1 - 0.9	3.9
UA6	$p\bar{p}$	24.3	0.34 – 0.63	-0.1 - 0.9	4.7
WA 70	*pp*	23	0.35 – 0.52	±1.0	5.2
Run II at the Tevatron [52]					
D0	$p\bar{p}$	2000	0.2	± 3.0	?
CDF	$p\bar{p}$	2000	0.16	± 1.1	?

Table 4.3: Parameters of various other direct photon studies.

The experiments cover a range from $x_g \sim x_T$ for photons in the central region (η close to zero) to $x_{\min} = \frac{x_T e^{-\eta}}{2 - x_T e^{\eta}}$.

The large range of x_T , from low to high $\sqrt{s}$, that has been studied is evident in the table. In addition, D0 has a much larger η coverage which extends the range that can be studied down to a lower x_g.

All the experiments compared their results with QCD NLO predictions using existing structure function parameterisations. The results generally show a discrepancy with predictions at low photon E_T independent of the corresponding value of x_g or x_T. This can be seen in Figure 4.7.

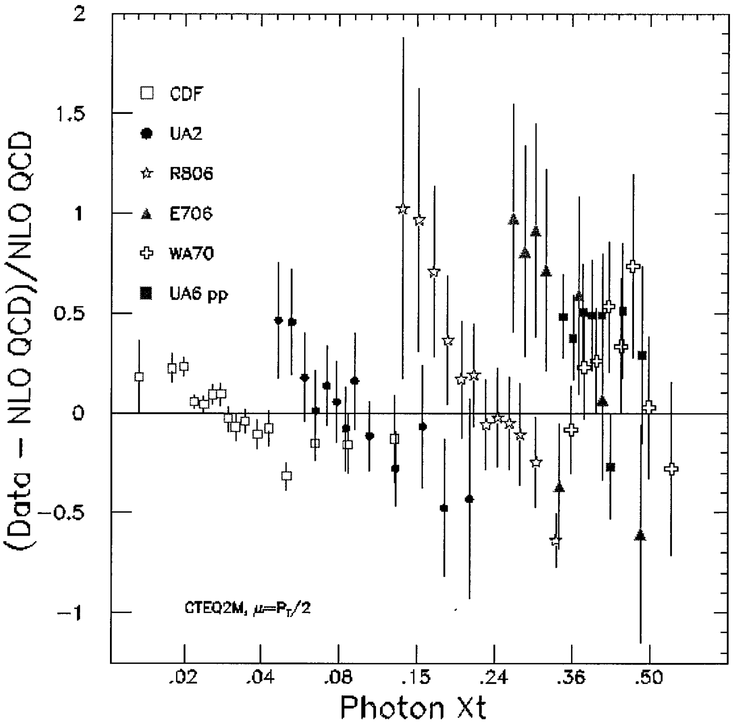

Figure 4.7 : x_T distribution comparison of existing direct photon cross section data with NLO QCD calculations with CTEQ2M parton distribution functions. [53]

Various explanations have been suggested for the discrepancy. It is generally thought to be due to modification of the slope of the E_T distribution by some source of k_T smearing [53]. This is smearing caused by the transverse momentum of initial state partons with respect to the incoming hadrons. If the initial state partons have some transverse momenta and are not collinear to the hadrons as has been assumed, the transverse momenta is passed on to the final state partons and makes their E_T spectrum steeper. This effect is clearly seen experimentally in the low E_T region where the amount of k_T is not negligible compared to the total E_T. The k_T smearing is a combination of the following effects:

- The initial state partons are confined within hadrons which are approximately 1.5 fm in size. Due to the uncertainty principle they should have some intrinsic transverse momenta around 0.4 GeV.

- The radiation of gluons from initial state partons will give the partons certain transverse momenta. This initial state gluon emission can be the dominant effect contributing to the k_T smearing.

There are at least two other possible causes for this shape difference [54]. A possible explanation is the QED bremsstrahlung process, in which an initial or final state quark radiates a photon. QCD predictions show good agreement with measurements at LEP [54], however a higher order calculation of this process [55] in $p\bar{p}$ collisions does indicate a prediction that is 5% steeper at p_T = 16 GeV. Another possibility is that the differences could indicate that the gluon distribution inside the proton in this fractional momentum range needs to be modified by the use of this data. It has also been suggested [56] that there is no need for an additional intrinsic k_T to force the agreement between QCD predictions and experiments.

D0 and CDF will be continuing their studies when Run II commences in 2000, providing higher statistics data. However as demonstrated in the previous section, the LHC will open up a new kinematic region to be studied. The higher luminosity at CMS means that we will be able to make good measurements in this new region in quite a short time.

5 Monte Carlo Simulation of Direct Photons in CMS

5.1 Introduction

Photons offer a unique window to the fundamental interactions both of the Standard Model and new physics. This is because they are fundamental vector bosons which emerge from the collision without either decaying or fragmenting into other particles. Photons can be cleanly identified and, unlike jets, their energy and direction measured precisely.

Within the Standard Model next to leading order QCD calculations exist which predict photon and diphoton production cross sections. By measuring these cross sections in CMS and comparing with the predictions we will be able to test our understanding of the Standard Model. These measurements are sensitive to the parton distributions. The parton distributions are important inputs to calculations of physics processes at the LHC. Various parameterisations exist which are in agreement with existing measurements from lower energy accelerators. At LHC energies we will probe new kinematic regions and be able to distinguish between the various parameterisations.

The cross section for the photon plus jet final state is very sensitive to the gluon distribution. Therefore a precise measurement of this process allows information on parton distributions to be extracted.

Unfortunately the advantages of photons as a clean probe of parton distributions are offset by the large backgrounds. Any analysis wishing to exploit photons must separate true direct photons (those coming from the hard scattering) from those copiously produced in the decay of π^0 and η mesons in jets.

In this chapter the simulation of direct photons and the backgrounds will be presented. It will be seen that direct photon production is a high cross section process which can be effectively simulated. The source of the background will be also be discussed and the generation of 2-jet events will be described. The event generator and the detector simulation will be discussed.

5.2 Direct Photons

The cross section for direct photon production predicted using the CTEQ4M parton distribution is shown in Figure 5.1. A large number of photons will be produced at the LHC. Isolated electromagnetic showers can be triggered on with high efficiency [57] above an E_T threshold of greater than 10 GeV. This threshold varies with the luminosity. The direct photon cross section at LHC will be approximately fifty times larger than at the Tevatron so even if we only did the same physics the results would be much more precise and the reduction in statistical error alone would improve the parton distribution measurements.

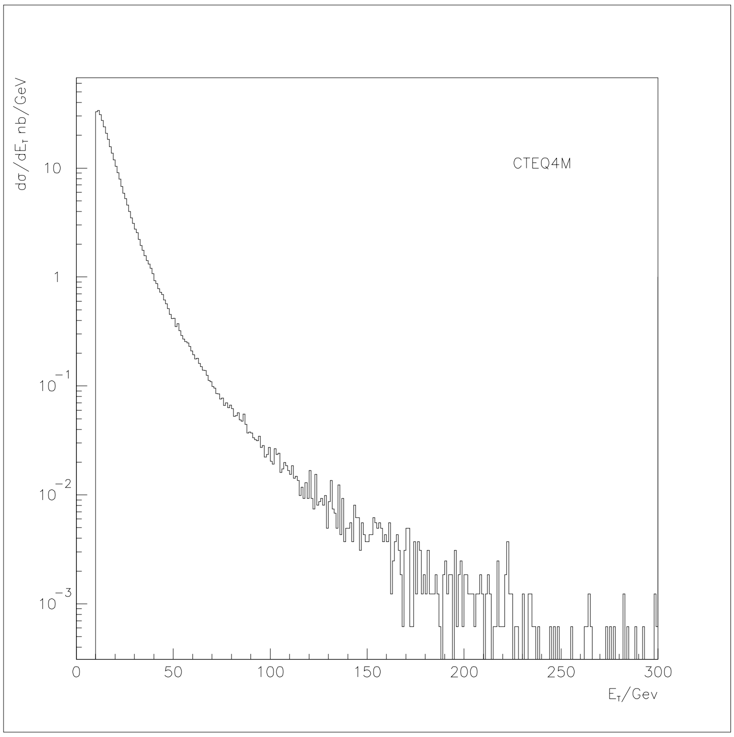

Figure 5.1: Direct photon cross section

Figure 5.2 shows the total events per year as a function of E_T for a luminosity of 10^{33} cm^{-2} s^{-1}. Direct photon analysis is likely to be one of the first physics studies to be done when the CMS experiment begins. There will be enough photons produced that an in depth study could be completed very quickly even at a luminosity of 10^{32} cm^{-2} s^{-1}. The direct photon samples in this analysis consist of 1 million events which is equivalent to one day at a luminosity of 10^{32} cm^{-2} s^{-1}. Even if the initial luminosity was as low as 10^{31} cm^{-2} s^{-1} this is only ten days running.

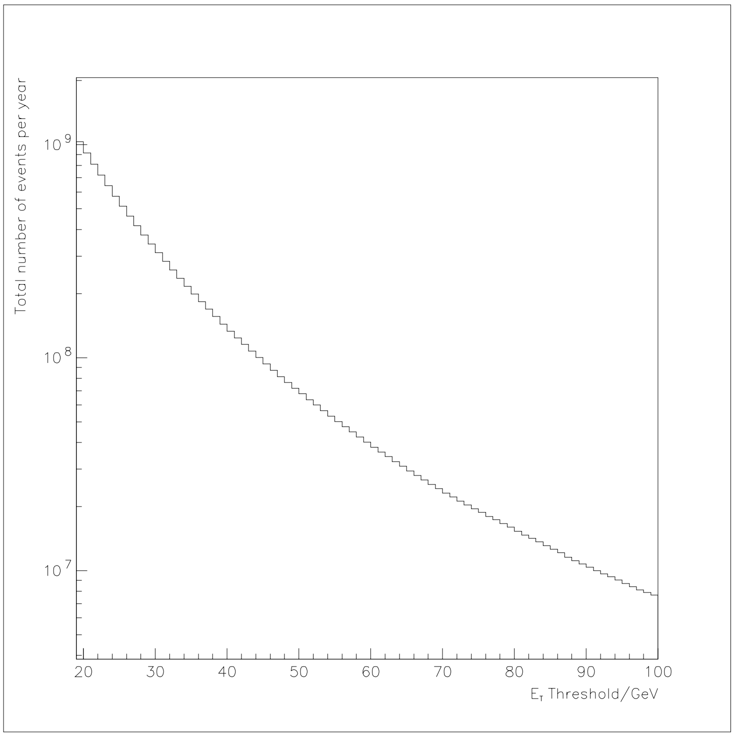

Figure 5.2: Events per year at a luminosity of 10^{33} cm^{-2} s^{-1}.

However, contributions from background decay processes greatly complicate analysis of the true direct photon signal. Figure 5.3 compares the direct photon cross section and that of the background. The methods for overcoming this hurdle are considered in detail in Chapter 6.

5.3 Background

There are two types of background that can contaminate the signal: fake backgrounds and irreducible backgrounds. Fake backgrounds occur when an event from a different type of process is misidentified and therefore fakes the desired signal. Irreducible backgrounds occur when another signal contains the same final state as the desired signal.

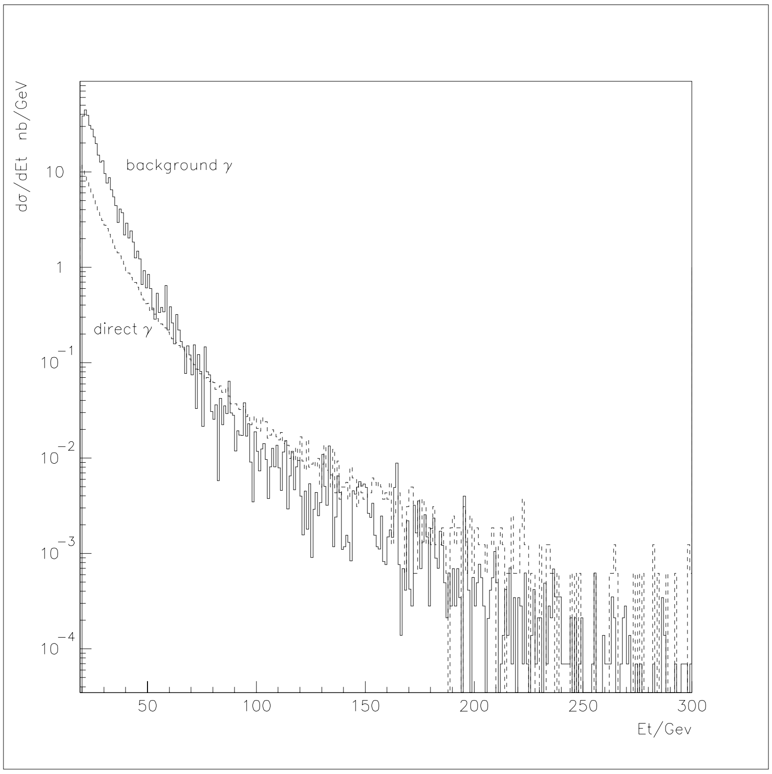

Figure 5.3: Direct photons and the background.

The dominant background to the direct photon signal comes from jet fluctuations. While most jets consist of many particles, and are thus easily distinguishable from a single photon, a small fraction ($\sim 10^{-3}$) fragment such that a single particle carries most of the momentum of the parent parton. Several neutral mesons decay to produce two or more photons. These include the lightest, and therefore most commonly produced, neutral meson, the π^0. The π^0 decays to two photons with a branching ratio of 99% [58], although at these energies the photons are very close together. This means that non-direct photons are common in hadronic collisions. The jet cross section is of order 1000 times larger than that for direct photons. Almost all jets can be rejected by the requirement that the photon candidate be isolated: that there should be no significant energy deposit or charged tracks in a region around the photon. Such a requirement typically rejects all but about 0.1 % of jets leaving only those where almost all the jet energy was carried by a single neutral meson and the jet consequently looked exactly like an isolated electromagnetic object. This remaining jet rate is still comparable to that of true direct photons and so additional rejection is needed.

Table 5.1 identifies several neutral mesons which decay to photons. The π^0 is the main particle considered in this analysis as it is the neutral meson that is most commonly produced although leading ηs can also contribute.

Particle	**mass(GeV/c²)**	**Decay products**	**branching ratio**
π^0	0.135	$\gamma\gamma$	0.99
η	0.547	$\gamma\gamma$	0.39
η	0.547	$3\,\pi^0$	0.32
η	0.547	$\pi^0\ \pi^+\ \pi^-$	0.23
K^0_s	0.494	$2\,\pi^0$	0.31
ω	0.781	$\pi^0\,\gamma$	0.09

Table 5.1: Neutral meson decays to photon states

It is difficult to generate enough events to study the background effectively because the two jet cross section is extremely large, 5×10^5nb compared to 6×10^2nb for direct photons. Although only one in a thousand jets will fragment in such a way as to become a problem this still results in a very large background. This means that to produce the require amount of background events many, many thousands of unwanted events must be generated.

5.4 Monte Carlo

In order to study direct photon events and their background at CMS we must be able to simulate the process and the response of the detector. Because there is no experimental data we rely heavily on Monte Carlo generated data to mimic the real data as closely as possible. The Monte Carlo must be able to simulate the various parts of the CMS detector, taking into account particle identification efficiencies, trigger efficiencies etc. In addition, it must be capable of processing quickly a large number of events.

5.4.1 PYTHIA

PYTHIA [59] is a well established event generator that has been used to generate the direct photon events in this analysis. To generate direct photon events the PYTHIA generator includes contributions from five processes: $q_i g \rightarrow q_i \gamma$, $q_i \bar{q}_i \rightarrow g\gamma$, $f_i \bar{f}_i \rightarrow \gamma\gamma$, $gg \rightarrow \gamma\gamma$, $gg \rightarrow g\gamma$. In hadron colliders the first and second processes are most important, with the final process giving an additional contribution which may be important in some kinematic regions. This is generally in the central region, low η, and is not of interest for this analysis.

PYTHIA was also used to generate the background events in this analysis. This was done by generating QCD two jet events. Input parameters for PYTHIA are shown in table 5.2. The PDFLIB [44] package was used within PYTHIA to choose the various parton distribution functions used in this analysis.

Parameter	**Direct Photons**	**Background**
Process	MSEL = 10 Prompt photon production	MSEL = 1 QCD jets
$\sqrt{s}$	14 TeV	14 TeV
$\hat{p}_T$ range / GeV	10 – 7000	20 – 300 in twelve unequal bins
η range	± 3	± 3
m_{top}	175 GeV	175 GeV

Table 5.2: Some input parameters for PYTHIA

5.4.2 The CMS Detector Simulation

CMSJET [60] is a stand-alone fast non-GEANT detector simulation of the CMS detector which is essentially generator independent. It parameterises particle–detector interactions as opposed to the full GEANT detector simulation provided by CMSIM [61] which requires an enormous amount of CPU time per event. CMSJET processes events from a generator through a selection of user defined kinematic cuts eliminating particles outside the detector acceptance. User defined cuts are then applied to the particles in the event table allowing, for example, a minimum p_T for leptons and photons. CMSJET then searches for events for objects which would cause the event to trigger, eg. a high p_T lepton or photon or a large missing E_T.

The remaining events are then passed through simulations of the various sub-detectors. The CMSJET calorimeter system is represented by a set of sectioned cylindrical volumes. Charged particles are tracked, through the uniform 4 Tesla magnetic field, up to the surface of the calorimeter system. To calculate the energy deposited in a particular part of the calorimeter a parameterisation of the shower is used. The energy/momentum of the particles are smeared according to the resolutions shown in Table 5.3. The showers' spatial development is then simulated in both lateral and longitudinal directions. The parameterisation for the showers is taken from the H1 experiment.

Sub-detector	**Resolution**
ECAL	$\sigma /E = 5\% / \sqrt{E} + 0.5\ \%$
HCAL	$\sigma /E = 82\% / \sqrt{E} + 6.5\ \%$
HCAL crack	$\sigma /E = 86\% / \sqrt{E} + 09.3\ \%$
VFCAL (hadrons)	$\sigma /E = 182\% / \sqrt{E} + 9.0\ \%$
VFCAL (e,γ)	$\sigma /E = 138\% / \sqrt{E} + 5.0\ \%$

Table 5.3: Calorimetry in CMSJET

In the muon chambers and the central tracker the momenta is smeared and only those muons able to produce a hit in the muon system are recorded.

The final analysis phase includes jet-finding, recalculating the measured missing energy and applying quark tagging efficiencies. Following this the relevant data are written out for subsequent analysis.

Jets are searched for in the ECAL and HCAL out to a rapidity $|\eta| = 3.0$ with a cone jet finding algorithm from UA1 [62]. Using the full granularity of both ECAL and HCAL an initial selection is performed that rejects any calorimeter deposit (cell) with $E_T < 1$ GeV. A pre-clustering stage then takes each cell in turn and adds to it any nearby cells which pass the criterion

$$\Delta R = \sqrt{\Delta\phi^2 + \Delta\eta^2} \text{ where } \Delta R < 0.2 \qquad (5.1)$$

with no restriction on the number of clusters a given cell may belong to. Overlapping pre-clusters that share 75% or more of their cells are joined together otherwise they are split apart with the cells going to the closest initiator cell. The remaining pre-clusters that have $E_T > 5$ GeV are designated jets. Finally, any cell that fails the initial selection stage or the 5 GeV cut are added to the nearest jet providing that $\Delta R < 0.2$. Once identified, each jet is labelled or tagged to the type of quark or gluon that initiated the jet. The standard CMSJET cut of 20GeV is designed for high luminosity processes. This analysis will be done at low luminosity where pile up is not a problem. Therefore a lower cut was chosen. Table 5.4 shows some of the user defined cuts that were used in CMSJET for this analysis.

Parameter	Direct Photons	Background
No of events	1000000	250000 in each of 12 unequal bins
γ search – E_T min – η photon	10 GeV 3.0	20 GeV 3.0
tracker – radius of cone around γ tracker – max p_T in cone	0.3 2 GeV	0.3 2.GeV
calorimeter – radius of cone around γ calorimeter – E_T sum limit in cone	0.3 5 GeV	0.3 5GeV
jet p_T cut jet energy cut jet η cut	5 GeV 5 GeV 3.0	5 GeV 5 GeV 3.0
min p_T threshold for π^0 to be treated as γ		10 GeV

Table 5.4: Some CMSJET parameters used in this analysis.

5.4.3 Limitations

CMSJET 4.4 was used for all the work in this thesis. It is based on the detector design in the Technical Proposal. The details of CMS design are still not finalised, although there now exists a later version of CMSJET. The most obvious change from CMSJET 4.4 is modifications to the CMS ECAL endcap designs. The resolution used for the

ECAL were larger than the latest test beam results [27], therefore providing a slightly pessimistic scenario.

5.5 Conclusion

By combining PYTHIA event generator and the CMSJET 4.4 detector simulation direct photon events and their background can be generated and the response of the detector can be evaluated. This enables the study of direct photons at CMS to be carried out.

6 Event Selection

As has been shown in Figure 5.3 the background from jets faking photons or photons in jets is a factor of four times as much as the direct photons at low E_T. This chapter outlines the cuts applied to the data with the main aim of reducing the background to the direct photon signal.

6.1 Photon E_T > 20GeV.

The first cut was to exclude all photons with E_T of less than 20 GeV. The main reason for this cut is that it would be difficult to trigger on photons with such a low E_T. At high luminosity it is proposed to trigger on single photons of E_T 40GeV to meet the constraints of the trigger system. At low luminosity it is possible to run with a lower trigger threshold but it is not envisaged to trigger with a single e/γ threshold of less than E_T 20 GeV.

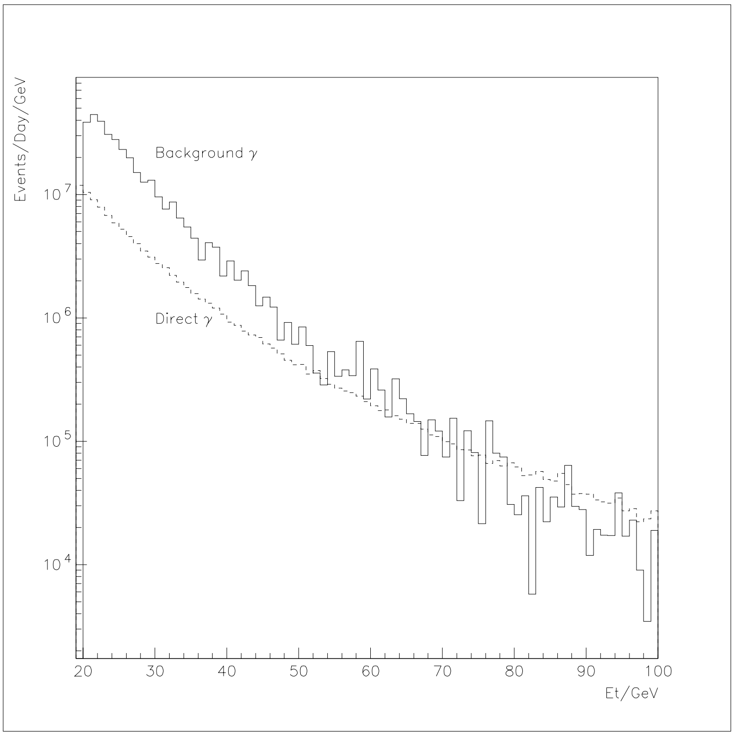

Figure 6.1: $E_{T\gamma}$ after cuts to exclude events with photons with an E_T of less than 20 GeV.

The cross section for the background falls more rapidly with E_T than the cross section for direct photons so it would be hard to do these studies at E_T of less than 20GeV even if the trigger threshold was lowered. The result of this cut is shown in Figure 6.1. It can be seen that the signal/background is worst in the low E_T regions.

6.2 Jet Rejection

6.2.1 Isolation

A jet being misidentified as a photon can cause a significant background to the direct photon signal. This can occur when a jet fragments into a leading π^0 and the resulting two photon decay is indistinguishable from a single direct photon in the detector. Initial and final state radiation photons from quark lines tend to be co-linear with the jets so isolation cuts will eliminate these as well.

Isolation cuts are used to reject particles coming from the fragmentation of jets by detecting the other jet fragments which accompany them. At high luminosity, pile-up and the underlying event (spectator system) will limit the effectiveness of an isolation cut. For any cut there will be a loss: events are rejected because the photon appears not to be isolated due to the presence of activity from other events in the same, or nearby, bunch crossing. In order to limit this loss to an acceptable level one can reduce the isolation area and/or raise the isolation threshold.

Traditionally isolation has been imposed by cutting on the summed transverse energy measured by both the electromagnetic and the hadronic calorimeters within a relatively large circle around the particle to be isolated. The performance of the CMS central tracking system together with the fine granularity and low noise of the electromagnetic calorimeter allow the use of ‘discrete isolation’ [63]. ‘Discrete’ isolation allows jet fragments accompanying candidate particles originating in jets to be detected individually above some p_T threshold. The p_T threshold arises from what can be reconstructed with good efficiency and what does not reject too many photons or electrons. The same threshold is usually used for both charged tracks and electromagnetic clusters. However, this is an arbitrary convenience, one could choose two different thresholds. Discrete isolation is more efficient at rejecting jets because the charged particles, which do not appear next to the original deposit because of the magnetic field, are included. Neutral particles cannot be tracked but as they follow a straight path they will appear close to the original deposit and therefore their energy is summed within the cone. The quantity, p_T, rather than p or E, is chosen since it is this quantity that is relevant for both the rejection power and the pile-up loss [63].

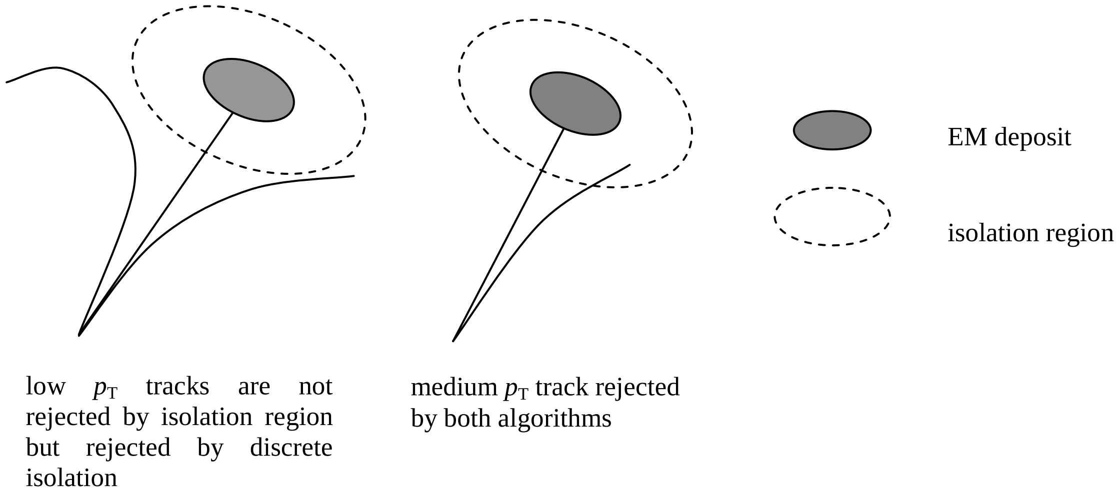

Figure 6.2: Diagram to show the principles of discrete isolation.

Discrete isolation provides approximately twice the rejection power, for the same pile-up loss, as the traditional isolation method [63]. With the large magnetic field in the CMS detector the traditional method requires a large isolation region rejecting a lot of the signal because of superimposed background events and noise or a small isolation region which reduces the elimination of background events because low p_T tracks such as those in the diagram are bent outside the region. Discrete isolation allows the tracking of such low p_T tracks and associating them with the vertex. One of the advantages of the discrete isolation cut is that one may reasonably assume that reconstructed tracks and electromagnetic energy deposits can be assigned to a single bunch crossing, whereas the transverse energy sum of the traditional definition will almost certainly integrate over more than one crossing.

In its simplest form the cut is made on the charged tracks alone, with a threshold of p_T > 2 or 2.5 GeV. Such tracks can be reconstructed with high efficiency and with the generation of a low number of fake or ghost tracks. It is necessary to assume only a modest performance for the central tracker: the ability to find isolated tracks with $p_T >$ 2 GeV with an efficiency greater than 95%, and with a generation of isolated ghost tracks ($p_T > 2$) at a level of less than 5% compared to real tracks. Apart from these assumptions, studies using the 4-vector output by Monte Carlo generators such as PYTHIA [59] (at the particle level) are completely adequate, since the dominant uncertainties are in the cross section and the fragmentation functions and these cannot be reduced by more detailed detector simulation.

For this analysis a cone of

$$\Delta R = \sqrt{\Delta\eta^2 + \Delta\phi^2} = 0.7 \qquad (6.1)$$

was used to isolate the photons. Figure 6.3 shows the minimum value of ΔR for the track in direct photon events. It demonstrates that cutting at ΔR = 0.7 will only remove 8% of the direct photon signal. The aim was to reduce the background while keeping the losses to the signal below 10%. The effects of using this isolation method combined with the photon E_T cut described in section 6.1 can be seen in Figure 6.4. This method removes 38% of the background at the same time as only reducing the signal by 8%. For high luminosity and low cross section processes a cone size of 0.3 would be more usual.

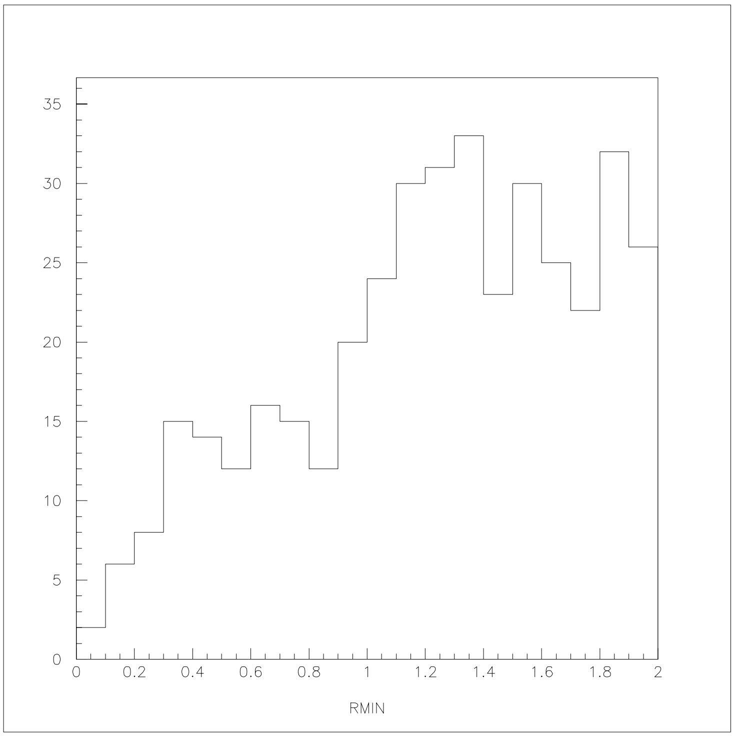

Figure 6.3: Plot of R_{min} for direct photon events.

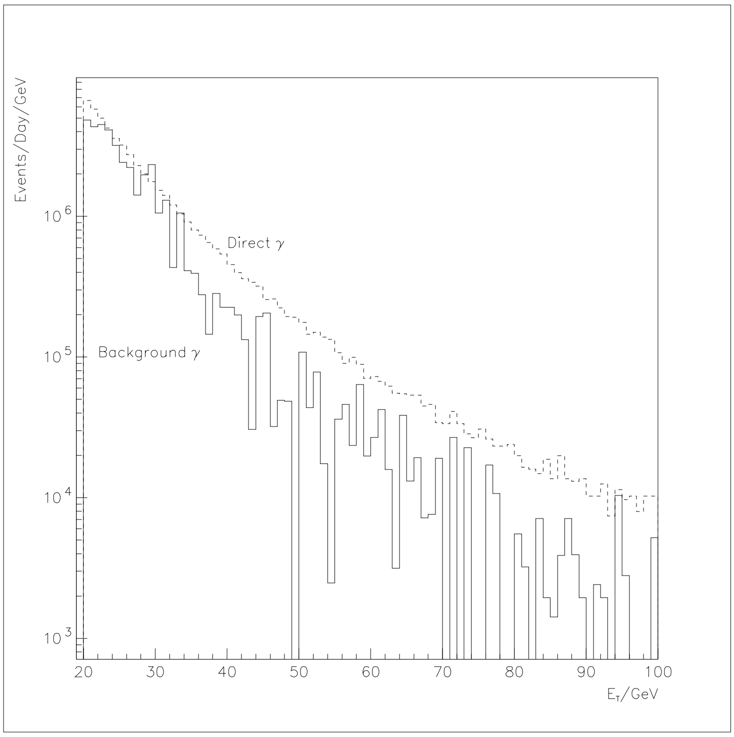

Figure 6.4: The results of using an isolation cone size of 0.7.

6.2.2 π^0 rejection

The main source of jet background for direct photons is from jets which fragment with a single π^0 taking a large fraction of the jet energy. The π^0s can be rejected by detecting the presence of two electromagnetic showers rather than one. In the barrel of the CMS detector this is achieved by cutting on the lateral shower shape in the crystals. In the endcap the preshower detector is used. Cuts are placed such that there is 90% efficiency for true single photons[13]. The resulting rejection curves, as a function of transverse momentum, have different characteristics. The limitation on the rejection power when using the crystals is the granularity of the crystals. The photons from a π^0 with p_T = 25 GeV have an average separation of approximately 15mm when they strike the crystals in the barrel. This distance is comparable to the crystal granularity and hence a large rejection factor is possible. however, the separation decreases linearly with increasing p_T and hence the rejection power drops steeply. This is illustrated in Figure 6.5[13]. In the endcap region the preshower can be used to give a higher rejection factor. The preshower has a granularity of 1.9mm which is small compared to the decay photon separation over most of the p_T range of interest for much of the endcap region. The preshower consists of

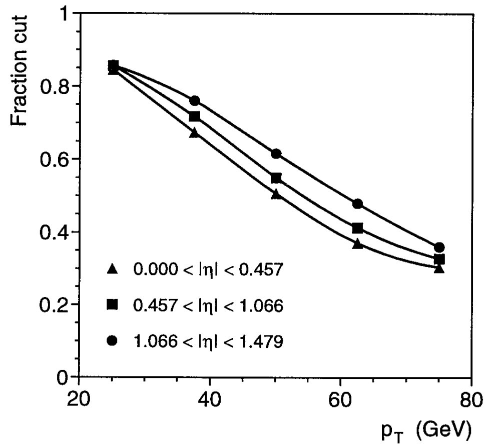

Figure 6.5: Fraction of π^0s rejected, using the lateral shape of the energy deposits in the crystals, as a function of p_T, for different η regions of the barrel.

a two X_0 layer of lead with two layers of scintillator in front of the endcap. The rejection power of the preshower detector is limited by shower fluctuations. Satellite deposits away from the shower core may mimic a double shower and reject genuine photons. The rejection curves that result are fairly flat in p_T as can be seen in Figure 6.6 [13].

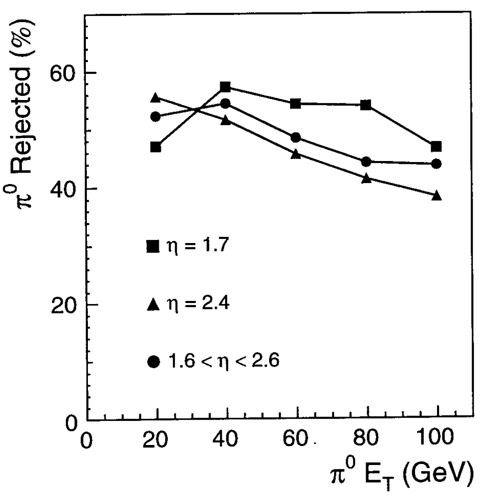

Figure 6.6: Variation of π^0 rejection as a function of E_T for three values of η.

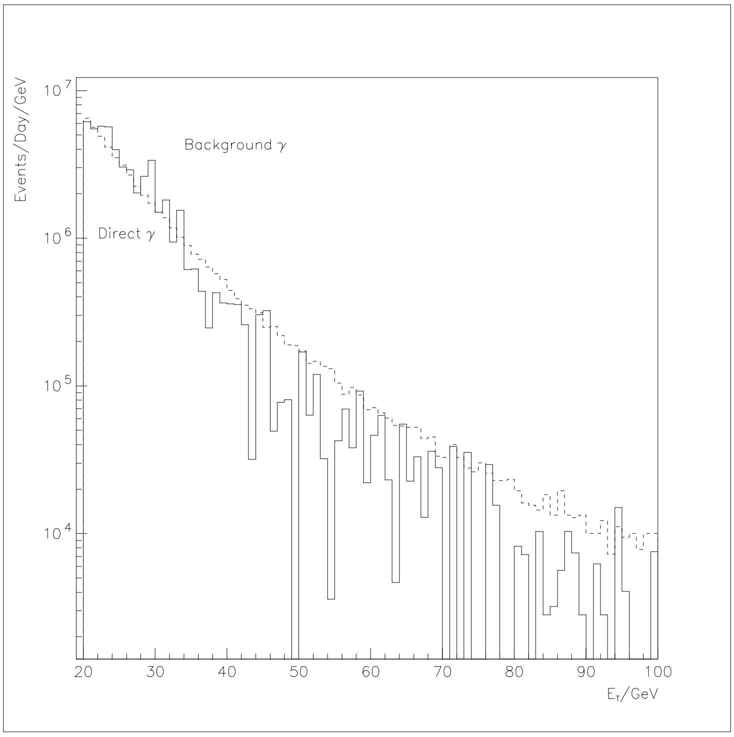

Figure 6.7: The effects of π^0 rejection upon the direct photons and the background.

It was assumed that for a given E_T and η the rejection was random. This is reasonable since the rejection depends on the orientation of the two decay photons relative to the detector. Therefore a parameterised version of these results was put into the detector simulation. For each π^0 faking a jet a random number was generated and if it was higher than the rejection fraction it was accepted. The results of this rejection, combined only with the $E_T > 20$GeV cut, can be seen in Figure 6.7. The plot shows that this is a very effective way of reducing the background.

6.3 Events with only one jet.

The next cut to be considered was to exclude events with more than one jet. Figure 6.8 shows the number of jets in the range $20 < E_T < 50$ GeV for both direct photon and background events. It is clear that cutting on 1 jet will improve the signal to background ratio.

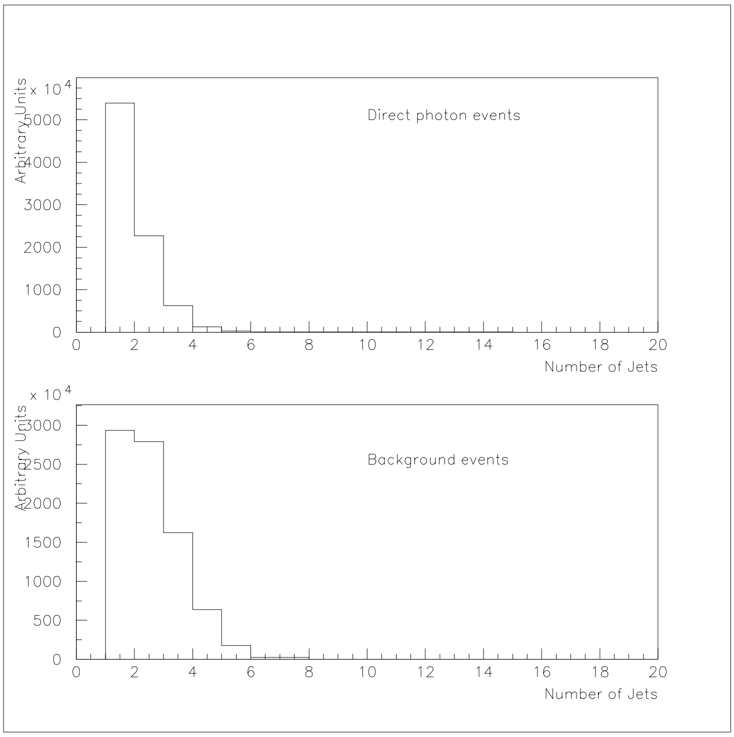

Figure 6.8: Number of jets for an $E_{T\gamma}$ range between 20 and 50 GeV for direct photon events and background events.

It can be seen that cutting on events with only one jet will keep approximately 66% of the direct photon events but will reject more than 60% of the background. If the event is a genuine 2-jet event where one jet fakes a photon we will not see two jets and therefore cannot reject the event with this cut.

The two main sources of background are initial and final state radiation, where a genuine photon is produced, and π^0s that fake photons. In CMSJET it is possible to separate the contributions from each type. Figure 6.9 shows the difference between background events that are real photons and background events where a π^0 is faking a photon. It demonstrates that cutting on events with only one jet will remove over two thirds of the genuine photons. This is very useful as obviously these are not rejected by the π^0 cut. This cut also helps to reject many of the events where a π^0 fakes a photon, for example, where a π^0 is isolated from the rest of the jet of which it is a part. The results of using this cut can be seen in Figure 6.10.

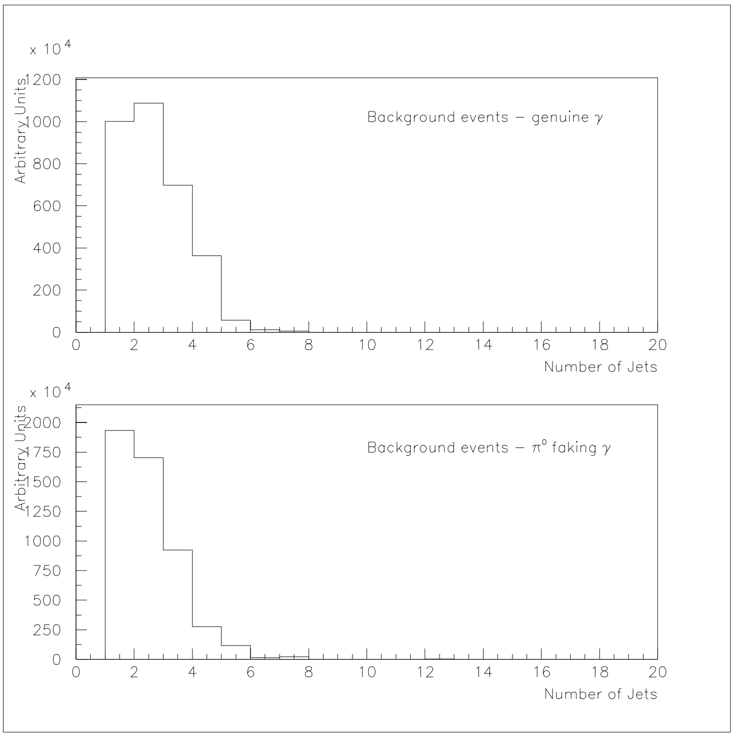

Figure 6.9 Number of jets for an $E_{T\gamma}$ range between 20 and 50 GeV for background events, divided between those events that are real photons and the events where π^0s are faking photons.

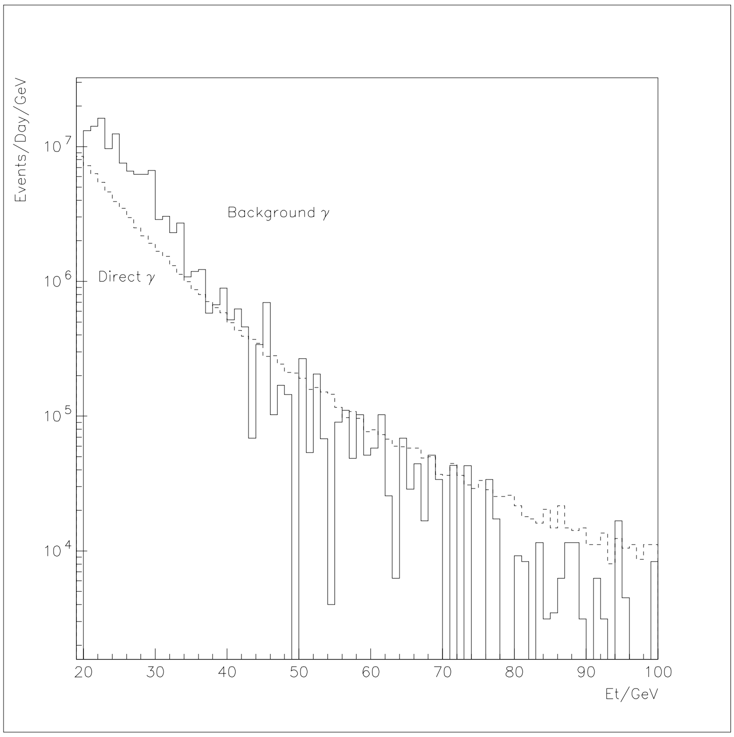

Figure 6.10: $E_{T\gamma}$ after cuts to exclude events with more than one jet.

6.4 Minimum bias

There will be a high rate of soft hadronic interactions, known as minimum bias events, from the bulk of the proton-proton interactions which do not involve a hard parton-parton interaction. The pile-up of many soft interactions in the same trigger gate, due to high luminosity and the extremely small inter-bunch spacing , adds a non negligible level of noise on top of the more interesting events particularly at high luminosity. This puts constraints on the level of background rejection that can be achieved in the analysis. In particular pile-up can limit the effectiveness of the isolation cuts.

In principle these interactions can arise because a single parton from one beam scatters against several different partons from the other beam, or because several partons from each beam take place in separate 2→2 scatterings. Both of these are possible but combinatorics tend to favour the latter, which is the mechanism used in PYTHIA. Using PYTHIA minimum bias events were generated with an E_T range of 20-7000 GeV. This corresponds to a total cross section of 1×10^8 nb. These events were then put through CMSJET and only those with a jet of at least 5GeV were written out. At very low luminosity, 10^{32} cm^{-2} s^{-1}, this cross section means that there would be 1×10^7 events every second compared to 60 direct photon events every second. Of 20,000 events generated only those with at least one jet of E_T greater than 5GeV were written out by CMSJET. This corresponds to 10% of those generated. Of these only 1 in 4 have E_T greater than 20GeV. This is illustrated in Figure 6.11. By cutting out events that do not have two jets the percentage of the total is reduced to 0.25%. Of these events only approximately 1 in a 1000 will result in minimum bias events that could cause a problem for this analysis by the jet fragmenting to fake a photon. Therefore only 25 minimum bias events per second could cause a problem. In addition, π^0 rejection eliminates 50% and isolation removes 38%. This reduces the minimum bias events to 4.6 per second which give a signal/background ratio of 12. This takes into account the cuts on the direct photons and can be compared with the ratio for direct photons and 2 jet events of ~2. It has been assumed that all jets of 20GeV or more could fake photons of E_T greater than 20GeV but not all of them would because some energy would be lost to low E_T tracks that are not reconstructed. Although this factor is not quantified it would reduce the signal to background ratio.

A detailed simulation would need to investigate minimum bias events and will need to be done when the detector design is finalised. They make a relatively small contribution to the background so for the analysis described in chapter 7 their contribution has been neglected.

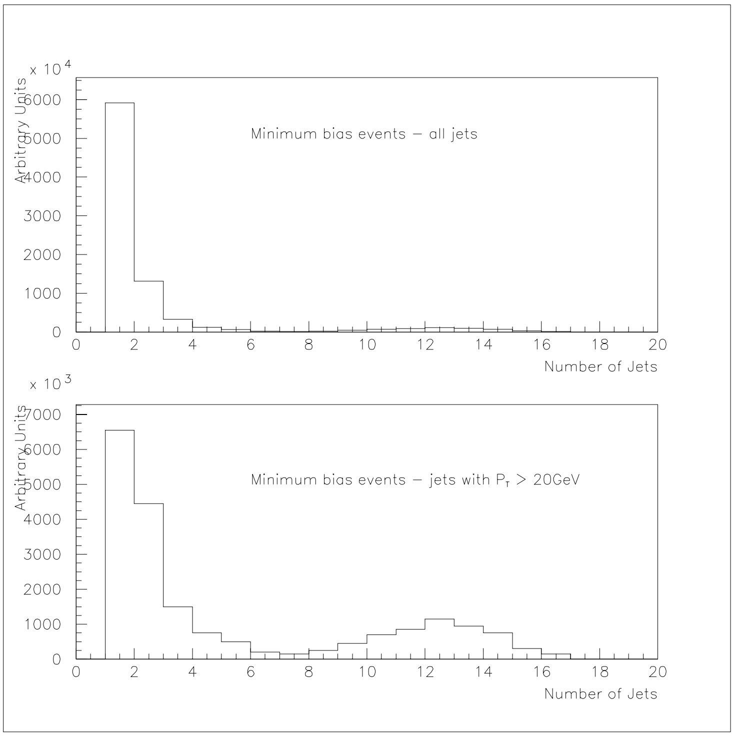

Figure 6.11: Minimum bias events – number of jets.

6.5 Conclusion

The signal to background ratio for the 2 jet background is shown in Figure 6.12 for the range $20 < E_{T\gamma} < 50$ GeV. This range is being focused on because it is in the lower E_T range that low x gluons are dominant. However trigger considerations mean that it is not practical to look below an E_T of 20 GeV.

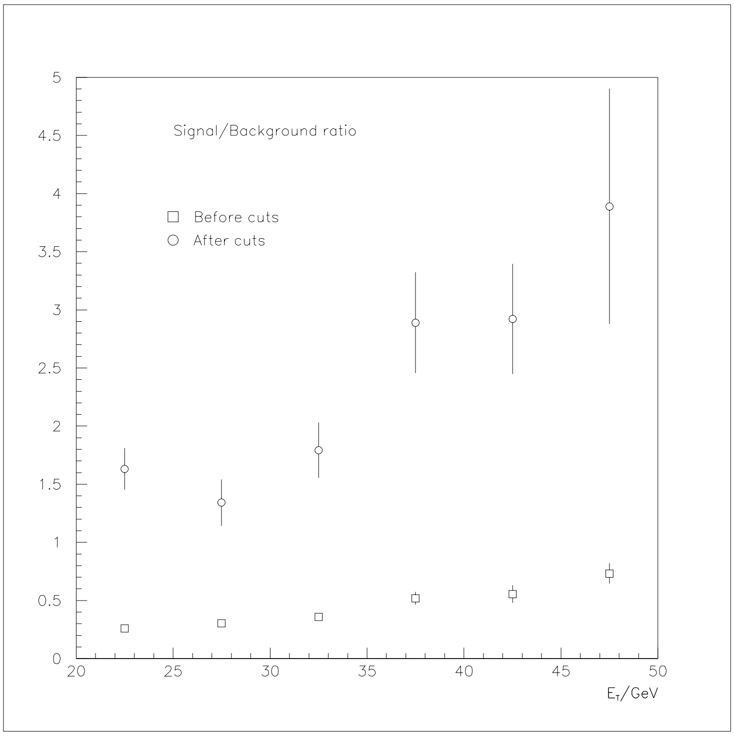

Figure 6.12: Signal to background ratio for events where $20 < E_{T\gamma} < 50$ GeV.

7 Direct Photons and the Gluon Distribution

7.1 Introduction

Previous analyses of deep inelastic scattering (DIS) experiments have obtained reasonable estimates of the parton distribution functions within hadrons. Yet, gluons enter the DIS process only as second order effects since they do not participate in the electromagnetic or weak interactions which are the primary processes taking place in deep inelastic scattering. Their behaviour is only measured indirectly by DIS analysis. Low *x* gluons are well measured at low Q^2 (1 – 10 GeV^2) but are not as well constrained at higher Q^2. On the other hand, in very high energy pp collisions gluons have very large contributions, and therefore these provide a good testing ground for gluon distributions.

In this chapter direct photon events that have been generated using five different parton distribution functions will be examined.

7.2 The E_T and the η spectrum

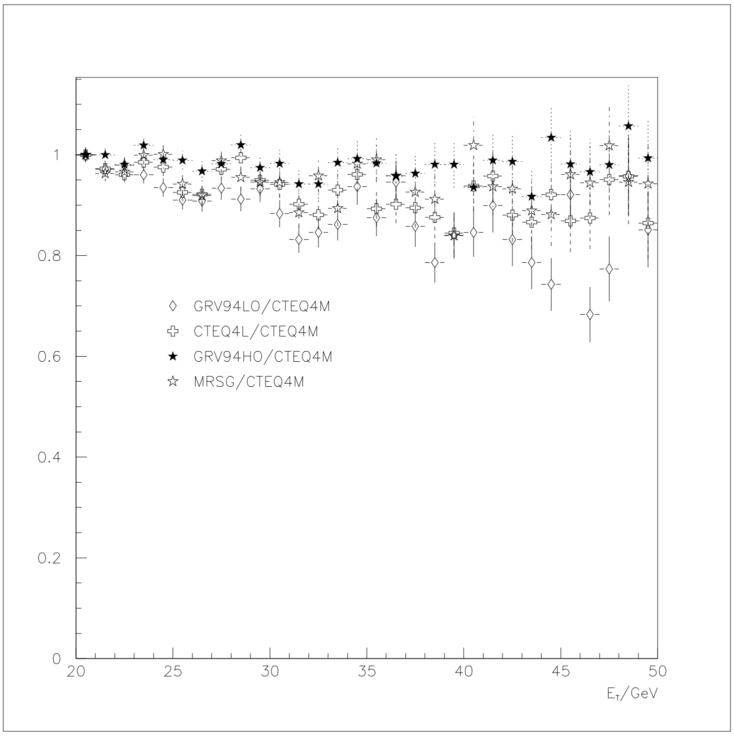

Figure 7.1: E_T spectra for four of the parton distributions in this analysis.

Figure 7.1 shows the E_T spectra, in the range $20 < E_T < 50$ GeV, for direct photons produced using the five different parton distribution functions used in this analysis. The E_T distributions have been normalised to the CTEQ4M parameterisation. It can be seen from the plot that it is difficult to distinguish between the different distributions. The best way to obtain information about the gluon distribution is to study the shape of the η spectrum. The E_T distribution has a five to ten % normalisation uncertainty from the choice of the renormalisation scale μ in the QCD calculation. This can be seen in Figure 7.2. This uncertainty is the same size as the effect we expect to see from different gluon distributions.

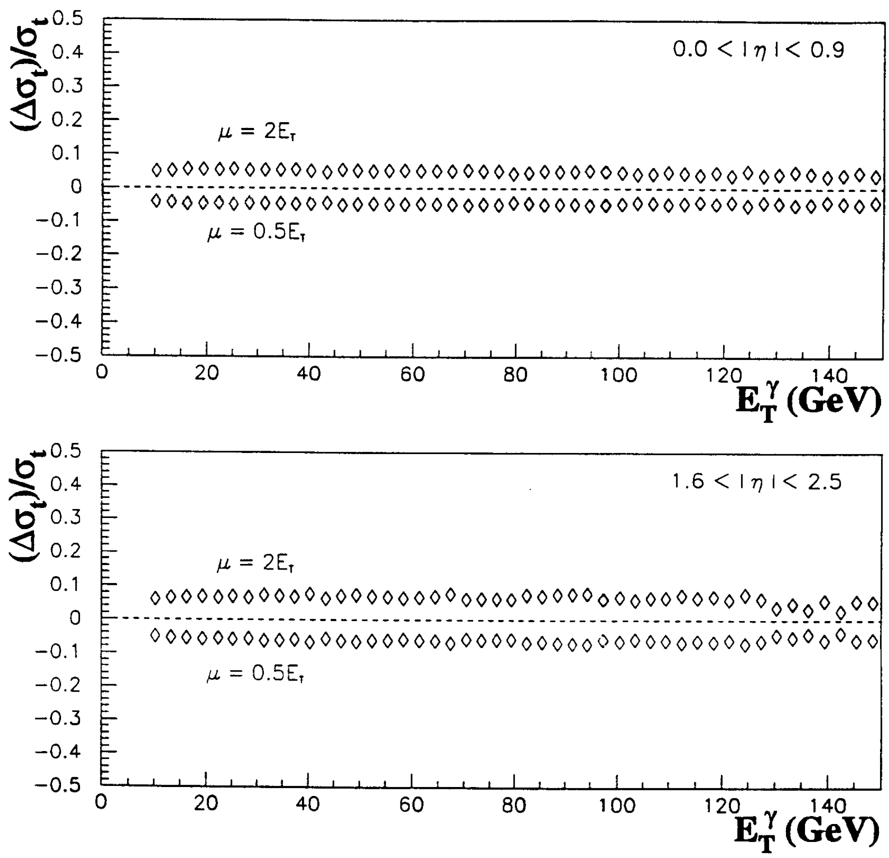

Figure 7.2: Variation of the theoretical prediction with a change in scale for the central (top) and forward (bottom) regions of the D0 detector [64].

Plotting the η spectra is slightly more helpful, this is shown in Figure 7.3, and it is possible to see more separation between the five different parameterisations. The E_T spectrum is flat but there is more shape variation in the η plot.

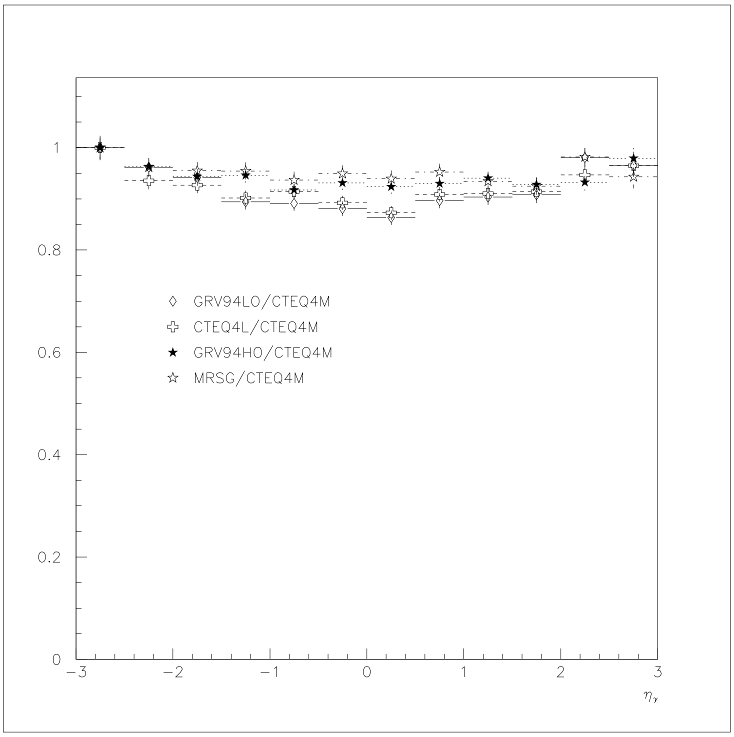

Figure 7.3. η spectra for the five different parton distributions.

7.3 Triple Differential Cross Section

Another method is to examine the triple differential cross section. The goal of this type of direct photon analysis is to help fix the gluon distribution at low *x*. At given E_T, η of the photon and η of the jet correspond to a given x_1 and x_2 of the partons in the incoming proton. Hence looking at the cross section in this triple differential form enables us to separate the contributions to the cross section coming from particular regions of *x*. In turn, this enables us to extract the parton distributions. Plotting the single differential cross section is equivalent to integrating over x_1 and x_2 and the changes due to different gluon distributions at low *x* are obscured by contributions from high *x* gluons.

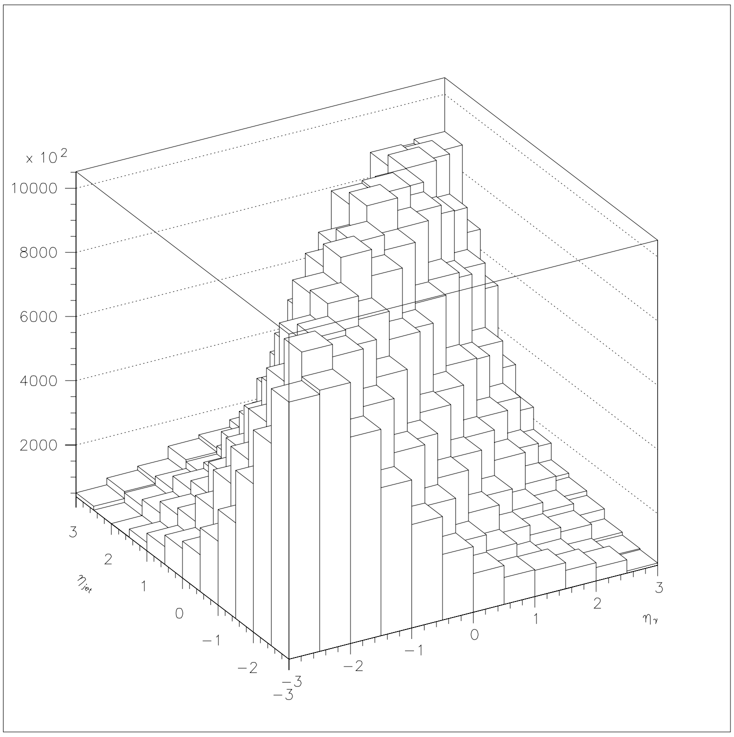

Figure 7.4: Triple differential cross section (No. of Events/Day/$d^3\sigma/dE_{T\gamma}\, d_{\eta\gamma}\, d_{\eta jet}$) using CTEQ4M for 20< $E_{T\gamma}$ <30.

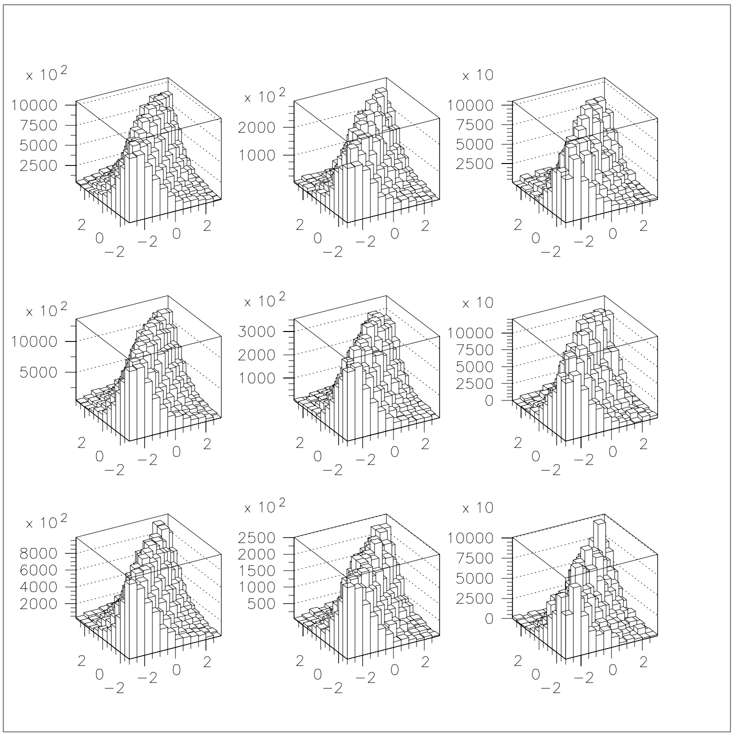

Figure 7.5: Triple differential plots for CTEQ4M (top), GRV94H0 (middle), MRSG (bottom) for $E_{T\gamma}$ ranges, 20-30, 30-40 and 40-50.

Figure 7.4 shows the triple differential cross section for the CTEQ4M parameterisation and Figure 7.5 shows a similar cross section for all three higher order structure functions and three different $E_{T\gamma}$ ranges. It is difficult to extract much useful information from this type of plot.

7.4 Event kinematics.

Because the dominant method of direct photon production at CMS is that of $qg \rightarrow q\gamma$ (QCD Compton scattering), one expects that the gluon distribution of the proton will affect not only the rate of direct photon production but also the associated kinematics. This can be demonstrated by considering the collision of two partons which create the leading order signal of one photon and one jet. This is illustrated in Figure 7.6.

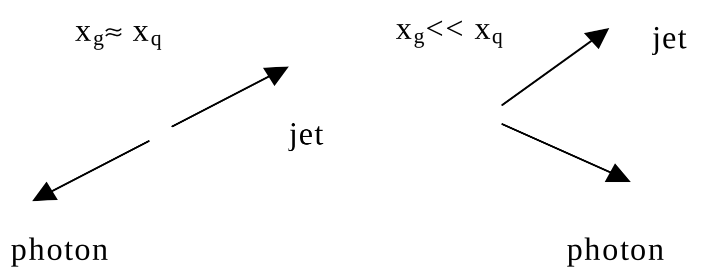

Figure 7.6: Diagram to show the final state topology when colliding partons have similar (left) or very dissimilar (right) momentum fractions.

If the partons are of equal momenta the system will retain its centre of mass back-to-back nature in the laboratory frame. If one parton is of much greater momentum than the other, then the system is boosted, as the more energetic parton overwhelms the softer one, and the final state objects tend to the same side of the event. Since gluons typically carry much less of the momentum of the proton than do the quarks one expects that in direct photon production unequal momentum combinations will dominate, and the final state will tend to be boosted in the direction of the incoming quark.

To increase the sensitivity to gluons at low *x* it is useful to require that the photon and the jet are on the same side of the detector. Therefore we define η_{jet} to be positive and in all subsequent plots η_γ is positive when on the same side of the detector as η_{jet}.

7.5 Direct photon distributions.

The differences due to the different gluon parameterisations are more obvious if the triple differential cross section is 'sliced' in η_{jet}. An example is shown in Figure 7.7 which shows the slice for $2.0 < \eta_{jet} < 2.5$ in the range $20 < E_{T\gamma} < 30$GeV.

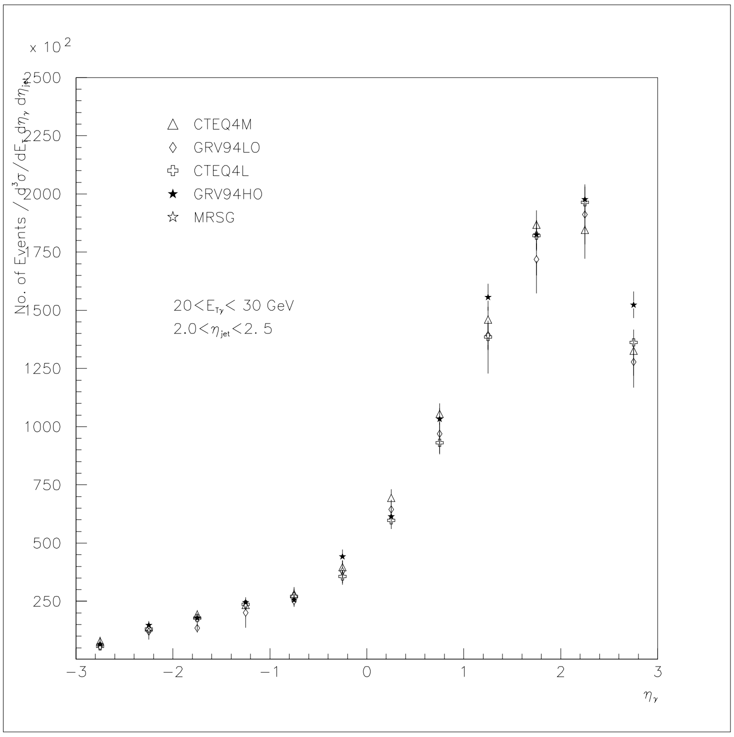

Figure 7.7. A slice in η_{jet} for the range 20< $E_{T\gamma}$ <30 GeV.

7.6 Background contributions.

Figure 7.8 shows a slice in η_{jet} for both the signal and the background. As can be seen the errors on the background are too large for this plot to be useful. This is because the number of background events generated is too low. It was not feasible to run more jobs to increase the statistics. CMSJET takes a very long time (two days for 250,000 events) to generate the required number of events. Because only approximately one in a thousand of these events will produce an event where a π^0 fakes a photon it takes a very long time to generate enough to study. In fact, to generate enough events would take 20 days for each of four p_T bins and to do this for two structure functions would need 160 days of CPU time. A full simulation in CMSIM the GEANT based detector description is not practical at the moment because it would take approximately 10 times more CPU time than CMSJET. Until the detector design is finalised such an investment of computer time is not warranted.

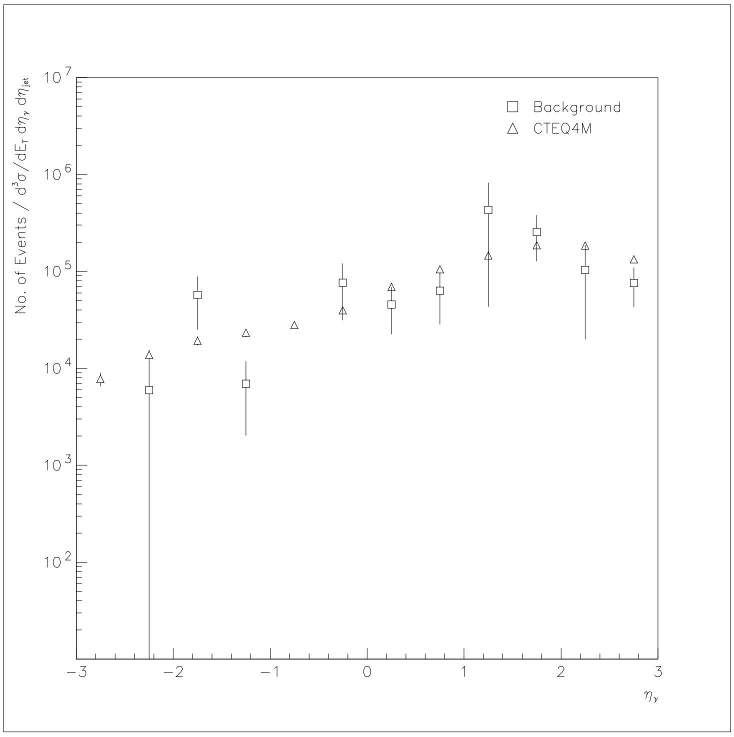

Figure 7.8: Signal and background for the CTEQ4M parameterisation.

In order to determine the feasibility of distinguishing between gluon structure functions by studying direct photon production a different approach was used. It was assumed that the fake photon distribution and the jet distribution in QCD 2 jet events are very similar i.e. that the jets which fragment to π^0s have the same E_T and η spectrum as other jets.

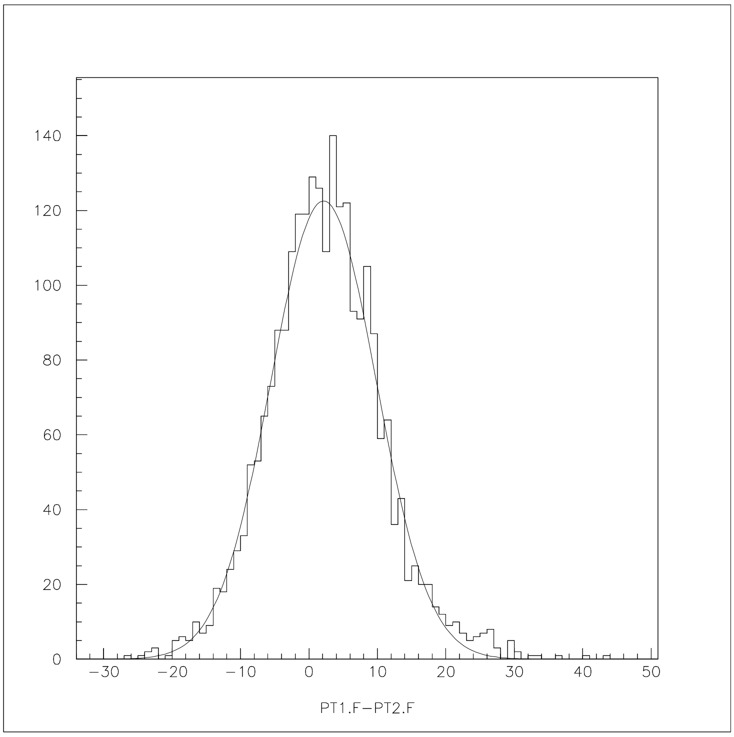

Figure 7.9: Difference in p_T between jet1 and jet2 in QCD jet events.

Events were generated in CMSJET and the second jet in each event was designated to be a fake photon. Figure 7.9 shows the difference between jet 1 and jet 2. Jet 2 has an average smaller p_T, it was assumed that this was because of the loss of accompanying tracks. These events were then put through the analysis program. This approach was taken to try and get an idea for what the effects of a high statistics background would be and whether the analysis is feasible. Table 7.1 shows the user defined parameters set in PYTHIA and CMSJET for this estimation of the background.

Parameter	Background
Process	MSEL = 1 QCD jets
$\sqrt{s}$	14 TeV
$\hat{p}_T$ range /GeV	20-65 in four unequal bins
η range	± 3
No of events	100000 in each of 4 unequal bins
γ search – E_T min – η photon	20 GeV ± 3
jet p_T cut jet energy cut jet η cut	5 GeV 5 GeV ± 3

Table 7.1: PYTHIA and CMSJET parameters of background estimation analysis.

These type of background events were generated using both CTEQ4M and GRV94HO parton distribution functions. The background and the signal were then added together. Figure 7.10 demonstrates the variation between the two different parameterisations for six bins in η_{jet} from $0 < \eta_{jet} < 0.5$ to $2.5 < \eta_{jet} < 3.0$. All six plots were for the range $20 < E_{T\gamma} < 30$ GeV.

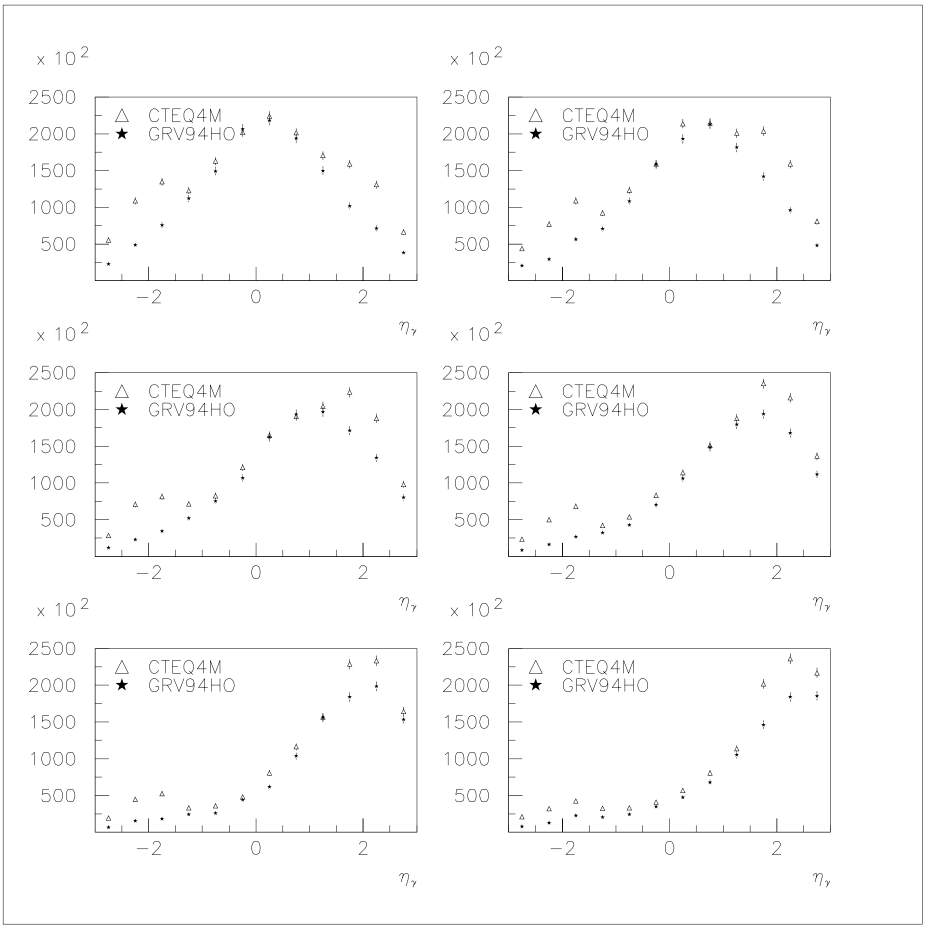

Figure 7.10: Six slices of the triple differential cross section in η_{jet} (No. of Events/Day/$d^3\sigma/dE_{T\gamma}\,d_{\eta\gamma}\,d_{\eta jet}$).

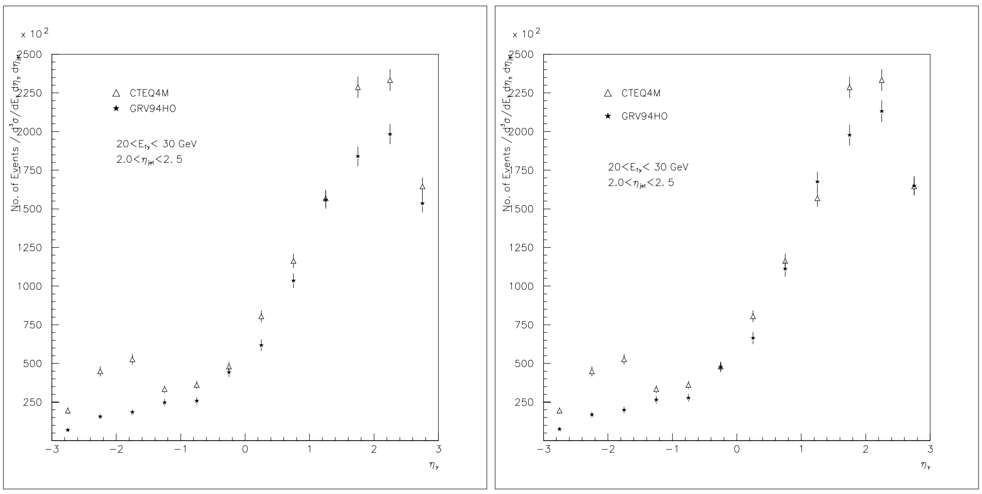

Figure 7.11: CTEQ4M and GRV94HO parameterisations for the range $20 < E_{T\gamma} < 30$GeV.

Figures 7.11, 7.12, and 7.13 each show two different plots. The first plots clearly show the separation between the two different structure functions. The second plots have been normalised to $\eta_\gamma = 0$ and $\eta_{jet} = 0$ over the range $20 < E_{T\gamma} < 30$GeV. This has been done to try and eliminate the systematics. After this normalisation the two structure function parameterisations are closer together but can still be clearly separated. The slight 'hump' in the negative η regions comes from the background contribution

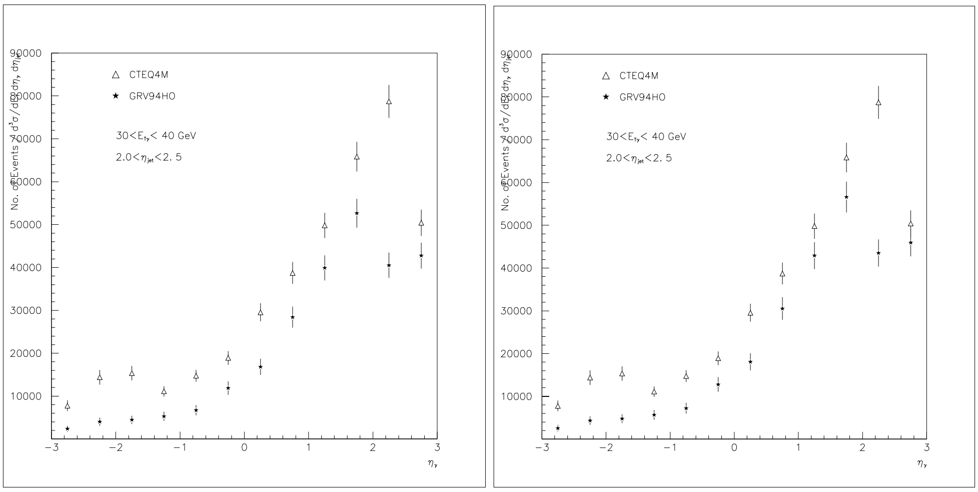

Figure 7.12: CTEQ4M and GRV94HO parameterisations for the range $30 < E_{T\gamma} < 40$GeV

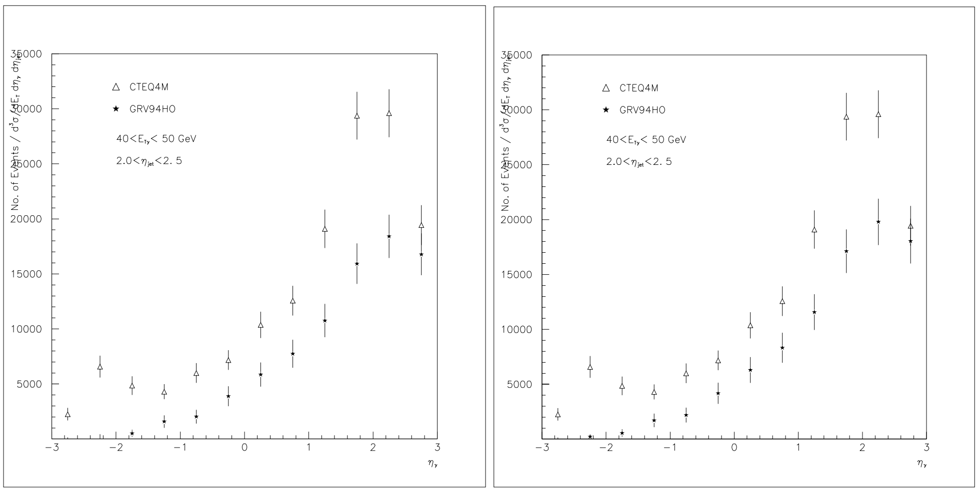

Figure 7.13: CTEQ4M and GRV94HO parameterisations for the range $40 < E_{T\gamma} < 50$GeV

This analysis has been done assuming only one days running at a very low luminosity (10^{32} cm^{-1} s^{-1}). If direct photons were studied for ten days then the statistical errors would be reduced by a factor of $\sqrt{10}$. This is demonstrated in figures 7.14 and 7.15.An increase in statistics would therefore improve the separation between the two structure functions.

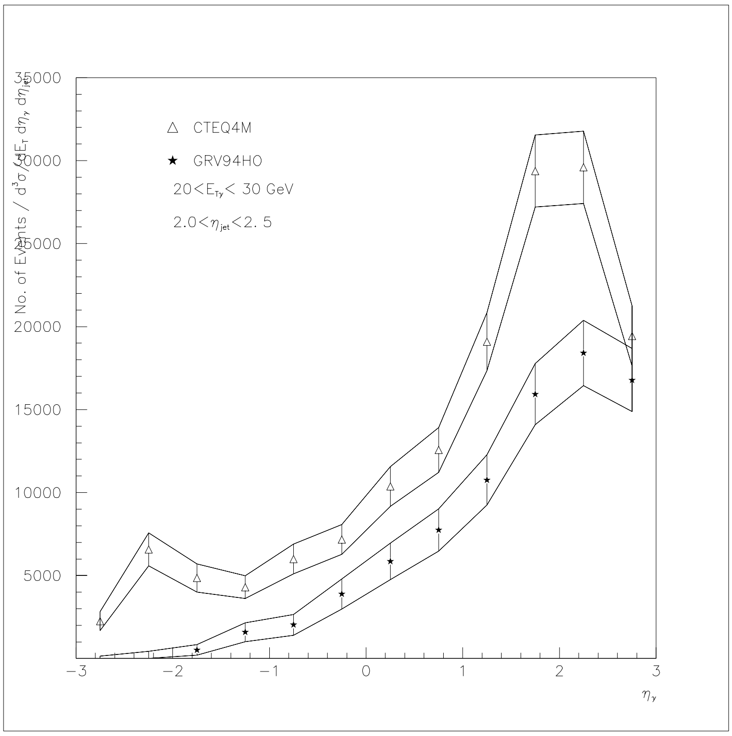

Figure 7.14: To show the statistical errors after 1 day at a luminosity of 10^{32} cm^{-2} s^{-1}.

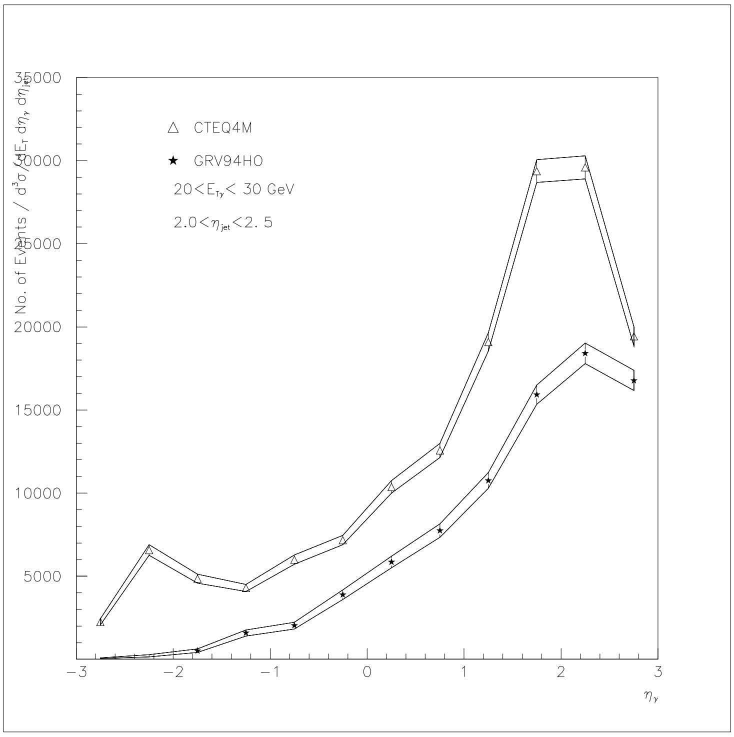

Figure 7.15: To show the statistical errors after 10 days at a luminosity of 10^{32} cm^{-2} s^{-1}.

It is not only statistical errors that will limit the measurement accuracy of the parton distributions. Systematic errors must also be taken into account. Systematic errors will arise from every phase of the detector construction and it is important to try and minimise these errors.

7.7 Conclusion

This analysis has been the first study of direct photon production at CMS. It shows that even after 1 day of running at a very low luminosity differences can be seen between different parameterisations of the gluon distribution. A longer period of data taking and therefore higher statistics would improve these results.

It is clear that a detailed study of the background would be essential for this type of analysis. However, it has been shown that it is difficult to generate sufficient events to make a reasonable study of the background to this analysis because of the length of CPU time that would be needed. A collaboration wide dedicated effort is needed to overcome this computing problem.

References

1. ATLAS Collaboration, *ATLAS, Technical Proposal for a General-Purpose pp Experiment at the Large Hadron Collider at CERN*, CERN/AC 95-05 (LHC), (1995).

2. CMS Collaboration, *The Compact Muon Solenoid Technical Proposal*, CERN/LHCC 94-38, (1994).

3. ALICE Collaboration, *A Large Ion Collider Experiment Technical Proposal*, CERN/LHCC 95-71, (1995).

4. LHC-B Collaboration, *A Dedicated LHC Collider Beauty Experiment for Precision Measurements of CP-violation*, CERN/LHCC 95-5, (1995).

5 E. Keil, *The Large Hadron Collider, LHC*. LHC Internal Note 1, (1996).

6. The LHC Study Group, *The Large Hadron Collider Conceptual Design Report*, CERN/AC/95-05(LHC).

7. V. Benda, *Conceptual Design of the Cryogenic System for the Large Hadron Collider (LHC)*,LHC Report12, (1996).

8 F. Teubert, *Precision tests of the Standard Model from Z physics*, hep-ph/9811414

9 M.Pimia et al, *Compact Muon Solenoid*, Proc.Large Hadron Collider Workshop, Aachen, 4-9 October 1990, eds. G. Jarlskog and D. Rein, CERN 90-10, vol III, (1990)

10 *CMS Expression of Interest*, Proceedings of the General Meeting on LHC Physics and Detectors, Evian, 5-8 March 1992.

11 F. Nessi-Tedaldi, Overview of $PbWO_4$ Calorimeter in CMS, CMS CR1998/003(1998)

12 The Magnet Group, *The Magnet Project Technical Design Report*, CERN/LHCC 97-10 (1997)

13 The ECAL Group, *The Electromagnetic Calorimeter Project Technical Design Report,* CERN/LHCC 97-33 (1997).

14 G. Tonelli, *The silicon tracking system for the CMS experimen*t, CMS NOTE/96-008

15 C. Seez and T.S. Virdee, *Detection of an intermediate mass Higgs boson at LHC via its two photon decay mode*, CMS TN/92-056, (1992)

16 CMS Collaboration, *The Hadron Calorimeter Project Technical Design Report*, CERN/LHCC 97-31, (1997).

17 D. Green et al. *HCAL Tailcatcher Decision*, CMS TN/008, (1996).

18 PPC Collaboration, *Proceedings of 1st Workshop on PPCs for Muon Trigger and Very Forward Calorimetry*, CMS TN/159, (1994).

19 CMS Collaboration, *The Compact Muon Solenoid Letter of Intent*, CERN/LHC 92-3, LHCC/I1, (1992).

20 D.Litvintsev, *Study of Degradation of the Quartz VFCAL Response due to Fibre Radiation Damage*, CMS TN/106, (1996).

21 D. Litvintsev. *Optimisation of the VFCAL Design*, CMS IN/003, (1996).

22 The Muon Group, *The Muon Project Technical Design Report*, CERN/LHCC 97-32, (1997).

23 F. Cavallari, *Progress on avalanche photodiodes as photon detectors for PWO crystals in the CMS experiment*, CMS CR/97 –010.

24 S. Baccaro et al., *APD properties and recovery from radiation damage*, CMS NOTE 30 (1997)

25 RDMS/UK Collaboration, *First test beam results on the ECAL Endcap Prototype* ,CMS NOTE 90 (1997)

26 P. Aspell, D. Barney, P. Bloch, S. Reynaud, A. Van Hove, J. Bourotte, *Results of tests of a Preshower Prototype during 1996*, CMS NOTE 32 (1997)

27 E. Auffray et al, *Beam tests of $PbWO_4$ crystal matrices and a silicon strip preshower detector for the CMS electromagnetic calorimeter*, Nuclear Instruments and Methods, A412:223-237,1998

28 J.P.Peigneux et al, *Beam tests on matrices of lead tungstate crystals using high energy beams,* Nuclear Instruments and Methods A378, 1996

29 C. Mackay, *1996 ECAL Test Beam Radiation Damage Catalogue*, CMS IN 1997/004 (1997)

30 O.V.Buyanov et al, *Beam Studies of EM-Calorimeter built of $PbWO_4$ crystals,* preprint IHEP 93-144 (1993)

31 R. Brun et al, *Simulation program for particle physics experiments*, GEANT, CERN DD 78-2 (1978)

32 D. Barney, P. Bloch, V.Popov, *Monte Carlo studies of barrel ECAL with preshower,* CMS TN 325 (1994)

33 A. Givernaud, *Monte Carlo study of a $PbWO_4$ crystal matrix,* CMS TN 119 (1996)

34 G. Alexeev et al. Nuclear Instruments and Methods, A385: 425-434 (1997)

35 Particle Data Group, Review of Particle Properties, Phys.Rev.Lett., B294, 1988, p 66

36 C.Seez, *Test Beam Irradiation Catalogue for 1997 and 1998*, CMS IN 1998/026 (1998)

37 J. Collins & D. E. Soper, Ann. Rev. Nucl. Part. Sci 37 (1987) 383.

38 H.L.Lai et al, *Improved Parton Distributions from Global Analysis of Recent Deep Inelastic Scattering and Inclusive Jet Data*, hep-ph/9606399 (1996).

39 P.Anandam & D. E. Soper, World Wide Web page '*A Potpourri of Partons*', http://zebu.uoregon.edu/~parton/.

40 A. D. Martin, R. G. Roberts & W.J.Stirling: Phys.Lett.354B (1995) 155;

41 M. Gluck, E. Reya & A. Vogt: Z Phys C67 (1995) 433.

42 Davison. E. Soper, *Parton Distribution Functions,* hep-lat/9609018 (1996)

43 H. Plothow-Besch, *PDFLIB: Nucleon, Pion and Photon Parton Density Functions and α_S Calculations; Users Manual – Version 7.09,* W5051 PDFLIB, 1997.07.02, CERN-PPE

44 P. Aurenche et al., *Prompt photon production at colliders,* Phys. Rev.D Vol 42. No 5. (1990) 1440-1449

45 J.P.Ralston, *Pocket Partonometer*, Phys.Lett B172, 430, (1986).

46 J. Owens, *Large-Momentum Transfer of Direct Photons, Jets and Particles*, Rev.Mod. Phys. Vol 59, No 2, 465 (1987).

47 M. Albrow et al., Structure Function Subgroup Summary, hep-ph/9706470, (1997)

48 L. Apanasevich et al., *Evidence for Parton K_T Effects in High-P_T Particle Production*, hep-ph/9711017 (1997).

49 G.Ballochi et al., *Direct photon cross sections in proton-proton and antiproton-proton interactions at* $\sqrt{s} = 24.3$ *GeV*,CERN-EP/98-111, (1998)

50 M. Werlen, *Review of New Direct photon Results*, IPNL 93-8 (1993)

51 W. J. Womersley, private communication.

52 J.Huston et al., *A Global QCD Study of Direct Photon Production,* Phys.Rev. D51,(1995) 6139.

53 F.Abe et al., *A Precision Measurement of the Prompt Photon Cross Section in* $p\bar{p}$ *Collisions at* $\sqrt{s} = 1.8$ *TeV*, Phys. Rev. Lett. 73, 225 (1994)

54 M. Gluck et al., *High –P_T Photon Production at* $p\bar{p}$ *Colliders*, D0-TH 94/02 (1994)

55 R. Nobrega & J. Varela, CMS TN/99-21, (1999)

56 C. Kaso et al, Eur. Phys. J.C.3. 1996

57 T. Sjostrand, *PYTHIA 5.721 and JETSET 7.408 generators*, Comp. Phys. Comm 82 74 (1994)

58 S. Abdullin, A. Khanov, N.Stepanov, *CMSJET 4.3*, CMSNOTE 180 (1994)

59 The CMS Collaboration, *Computing Technical Proposal*, CERN/LHCC 96-45 (1996)

60 B. Flaugher, K.Meier, *A compilation of jet finding algorithms*, Proc. of the Summer Study on Physics, Snowmass (1990)

61 C. Seez, *Using Isolation cuts in CMS*, CMS TN 003 (1992)

62 S. A. Jerger, Doctoral Thesis (Michigan State University), 1997.

Glossary

Absorption Length The mean free path of a particle undergoing a non-elastic collision in a given medium.

Acceptance The acceptance *a* of an experiment is defined as the average detection efficiency

ALICE A Large Ion Collider Experiment, The collaboration responsible for the design and construction of the dedicated heavy ion detector for the LHC accelerator.

ATLAS A Toroidal ApparatuS for LHC, one of two general purpose experiments for the LHC accelerator.

APD Avalanche PhotoDiode, a silicon photo-detector with high internal gain and low overall noise.

CERN Conseil European pour la Recherche Nucleaire, one of the worlds largest particle physics research institutes situated in Geneva on the Swiss/French border.

CMS Compact Muon Solenoid, one of two general purpose experiments for the LHC accelerator.

Cross Section The cross section, σ is defined as a Lorentz invariant measure of the probability of interactions in a two particle initial state.

DAQ Data AQuisition, a system for reading out, processing and storing data from a data source such as a HEP experiment.

DME Di-Methyl Ether, gas used in Drift Chambers.

ECAL Electromagnetic CALorimeter, calorimeter optimised for the detection of electrons and photons. Such a calorimeter will be designed with many radiation lengths to fully contain electromagnetic showers but will be constructed from materials with long interaction lengths to ensure a minimum of interacting hadronic particles.

GEANT A program that describes the passage of elementary particles through matter.

HCAL Hadron CALorimeter, detector optimised for measurement of hadron energies. Constructed from materials such as iron or lead with very short interaction lengths, HCALs force high energy hadrons to shower. Liquid argon or scintillator is then used to sample the shower at various depths.

HERA Hadron-Elektron Ring Anlage, an accelerator colliding electrons/positrons and protons at DESY in Hamburg.

Hermeticity A term used in calorimeters to describe maximal coverage for particles under all emission angles, combined with minimal leakage.

Interaction Length λ, the interaction length of a material is defined as the mean free path of a proton between inelastic collisions while traversing that material.

k the gain factor of an APD, the ratio of the ionisation coefficients for holes to electrons.

LED Light Emitting Diode, LEDs behave in a similar manner to normal diodes except that they light up when sufficient current flows through them.

LEP Large Electron Positron collider, accelerator currently taking data at CERN.

LHC Large Hadron Collider, a 14TeV centre of mass proton-proton accelerator to be built at CERN.

Moliere Radius A characteristic constant of a material describing its electromagnetic interaction properties and related to the radiation length by $R_M = 0.0265 X_0 (Z + 1.2)$ with X0 the radiation length and Z the atomic number.

MSGC Microstrip Gas Chamber

Pileup Background signals which add to observed events, originating in multiple events that occur in the same time gate as the signal of interest.

PS Proton Synchrotron, the first accelerator to be built at CERN, it successfully accelerated protons up to energies of 24 GeV.

QCD Quantum ChromoDynamics, the theory describing the interactions of particles governed by the strong force.

QED Quantum ElectroDynamics, the theory describing the electromagnetic interactions of electrons and photons.

Radiation Length X_0, the radiation length of a material is defined as the average distance required for a high energy electron to lose 1/e of its energy while traversing the material.

RF Radio Frequency, the electromagnetic fields in RF cavities are used to accelerate bunches of particles with the same momentum around circular accelerators.

RMS Root Mean Square, a statistical term referring to normal distributions. The error on a total which is calculated from the sum of a number of uncorrelated values is the square root of the sum of the squares of the errors on those values.

SMD Silicon Microstrip Detectors, particles passing through the depleted area between silicon strip and collector create a signal which can then be read out. Position is only accurately defined in one direction although charge collection times provide some information as to the exact impact point.

SPD Silicon Pixel Detectors, particles passing through the depleted area of one of the very small silicon pixels creates a signal which can then be read out to provide exact position information.

SPS Super Proton Synchrotron, big brother of the PS accelerator. The SPS can accelerate protons up to energies of 450GeV.

SUSY SuperSYmmetry, an extension to the Standard Model which proposes partners for each of the Standard Model particles differing by half a unit of spin.

TRIDAQ TRIgger and Date AQuisition, a system that selects then stores interesting physics events from a large number of background events.

VFCAL Very Forward Calorimeter, a radiation hard calorimeter used at high rapidities.